UCGE Reports
Number 20271

Department of Geomatics Engineering

Use of the Global Environmental Multiscale Model for Atmospheric Retrieval from Radio Occultation for Canadian Events

(URL: http://www.geomatics.ucalgary.ca/research/publications/GradTheses.html)

by

Lance de Groot

June 2008

UNIVERSITY OF CALGARY

Use of the Global Environmental Multiscale Model for Atmospheric Retrieval from Radio Occultation for Canadian Events

by

Lance de Groot

A THESIS

SUBMITTED TO THE FACULTY OF GRADUATE STUDIES

IN PARTIAL FULFILMENT OF THE REQUIREMENTS FOR THE

DEGREE OF MASTER OF SCIENCE

DEPARTMENT OF GEOMATICS ENGINEERING

CALGARY, ALBERTA

JUNE, 2008

© Lance de Groot 2008

Abstract

GPS radio occultation is a method for determining vertical profiles of refractivity, temperature, pressure, and humidity in the troposphere. External temperatures are required as input. The ECMWF numerical weather prediction model is frequently used for input temperature data. Within Canada, the primary NWP model in use is the GEM model. The suitability of GEM as an alternative source of temperature data is investigated.

The sensitivity of retrieved temperature profiles to residual orbital error and errors in the boundary condition is investigated for a data set of Canadian occultations. The sensitivity of retrieved humidity to refractivity and external temperature error is also examined. The accuracy of the GEM temperatures is assessed against these sensitivities and found to be adequate.

Actual retrievals are performed using input data from GEM. Profiles are compared to the CHAMP product and radiosondes. Results support the conclusion that GEM is suitable for radio occultation work in Canada.

Acknowledgements

I wish to thank my supervisors, Dr. Susan Skone and Dr. Kyle O'Keefe, for guidance and technical advice throughout the preparation of this thesis. Also the Alberta Ingenuity Fund, the Natural Sciences and Engineering Research Council of Canada, and the Geomatics for Informed Decisions Network of Centres of Excellence for financial support, without which this thesis would not be possible. All of my colleagues throughout the years, in particular Natalya Nicholson, Ossama al-Fanek, Mohammed Zafer Sadeque, and Fatemeh Ghafoori, for frequent help and consultation. Lastly my friends, family, and especially Teri Anderson, for their unceasing support throughout.

Table of Contents

List of Tables

List of Figures

List of Symbols

ϕ	GPS phase observable
ρ	true GPS range
$d\rho$	orbital error
c	speed of light
dt	receiver clock error
dT	satellite clock error
λ	wavelength
N	integer ambiguity
$trop$	tropospheric delay
$iono$	ionospheric delay
ε_m	multipath
ε	noise
Δ	single difference
$\nabla\Delta$	double difference
θ	colatitude
φ, λ	latitude and longitude
R_C	Radius of curvature of spherical approximation
P	Coordinates of tangent point
$\mathbf{v}_{GPS}$	velocity of GPS satellite
$\mathbf{v}_{LEO}$	velocity of LEO satellite
$\mathbf{r}_{GPS}$	position of GPS satellite
$\mathbf{r}_{LEO}$	position of LEO satellite
$\mathbf{k}$	inter-satellite vector
d_a	atmospheric Doppler
d	observed Doppler
d_g	geometric Doppler
α	bending angle
a	impact parameter
r	*r*adius of tangent point
f	frequency
n	index of refraction
N	refractivity in parts per million
P	pressure
T	temperature
e	partial water vapour pressure
RH	relative humidity

List of Abbreviations

C/A	Coarse Acquisition
CDMA	Code Division Multiple Access
CHAMP	Challenging Minisatellite Payload
CMC	Canadian Meteorological Centre
CT	Canonical Transform
ECMWF	European Centre for Medium-range Weather Forecasts
GEM	Global Environmental Multiscale
GFZ	GeoForschungsZentrum Potsdam
GNSS	Global Navigation Satellite System
GPS	Global Positioning System
IF	Ionosphere Free
IGS	International GNSS Service
LEO	Low Earth Orbiter
MSISE	Mass Spectrometer Inchoherent Scatter
NWP	Numerical Weather Prediction
P	Precise
PRN	Pseudo-random Noise
RMS	Root Mean Square
RO	Radio Occultation
SLR	Satellite Laser Ranging
SNR	Signal to Noise Ratio

Chapter 1 - Introduction

1.1. Background

The Global Positioning System (GPS) is a space based navigation system operated by the Department of Defense of the United States of America. Since 1993 the constellation has been maintained at a minimum level of 24 satellites, and has seen widespread use as a positioning and navigation tool in both the military and civilian communities. In 2007, the constellation consisted of 30 satellites. Typical positioning accuracies attainable are on the level of a few metres, with much higher accuracies possible through the use of differencing methods and error correction. More recently, the GPS has been used as a tool for atmospheric sensing. By fixing the coordinates of a GPS receiver, one can instead observe the error contributions from the ionosphere and troposphere, and estimate their magnitudes. Estimates of the total zenith tropospheric delay with these techniques can be on the level of a few cm (Bevis et al, 1992).

Radio occultation (RO) is a technique for deriving information about the properties of an atmosphere by observing radio signals that pass through it tangentially to the surface (Figure 1.1). This technique was demonstrated for the occultation of the Mariner V spacecraft by Venus in 1967 (Fjeldbo et al, 1971). The technique has since been applied to GPS signals observed by Low Earth Orbiting (LEO) satellites in order to sound the Earth's atmosphere. The first experiment of this nature was the GPS/MET experiment flown aboard the Microlab-1 satellite launched in 1995 (Hocke, 1997). Since GPS/MET

several other RO experiments have been launched, notably SAC-C, CHAMP, and the recently launched COSMIC constellation (e.g. Rocken et al, 2000, Wickert et al, 2001a, Hajj et al, 2004). The research conducted in this field has seen a corresponding increase with the enhanced data availability.

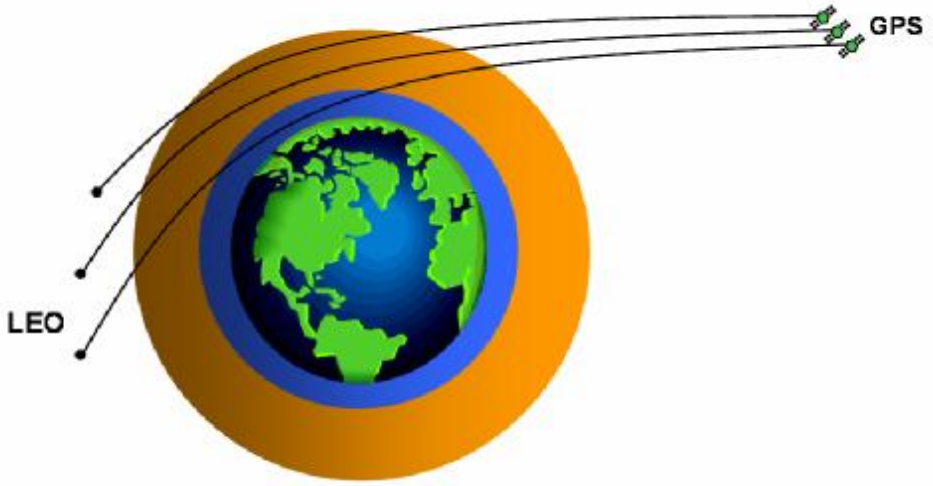

Figure 1.1: Radio Occultation technique

The primary data derived from an occultation is a vertical profile of the atmospheric refractivity. As the signals pass the atmosphere they are bent, experiencing increasing bending with increasing refractivity at lower altitudes. The amount of bending can be calculated by knowledge of the positions of the transmitter and receiver. The total bending can then be inverted using an Abel integral transform to solve for the refractivity of the atmosphere at the idealized point of bending. As the observed GPS satellite sets with respect to the LEO, a vertical profile of refractivity is estimated. Given an a priori boundary value of temperature or pressure at a given height, full profiles of temperature

and pressure can be derived from the refractivity. If a full a priori temperature profile is available, water vapour in the troposphere can be estimated instead (e.g. Steiner et al, 1999, Hajj et al, 2002). The typical source for boundary conditions or temperature profiles is a Numerical Weather Prediction (NWP) model.

Compared to ground based GPS atmospheric sensing techniques (in which total atmospheric delay above a receiver or network of receivers is estimated), radio occultation provides far greater vertical resolution. Ground based networks are limited by receiver geometry, in that all stations receive signals which have passed more or less vertically through the troposphere, making it difficult to distinguish the vertical structure of the atmosphere. Radio occultation signals pass horizontally through the atmosphere, and so vertical changes are easily observed as the ray path descends. The tradeoff is that radio occultation offers poor horizontal resolution, as the occulting rays pass through and are affected by several hundred kilometres of atmosphere. Kursinski (2004) estimates the horizontal resolution of an occultation sounding at 300 km.

Another limitation of the technique is poor performance in the lowest few kilometres of the atmosphere. This is caused by poor receiver tracking at low altitudes, as well as difficulties in correctly retrieving the bending angle profile when complicated atmospheric structures are present (e.g. Ware et al, 1996). Current research in the field includes work on techniques to overcome these problems and extend successful retrieval lower into the atmosphere. To prevent receiver loss of lock at low altitudes, it is possible

to use open-loop tracking, in which the signal is not tracked by a conventional phase lock loop, but rather the raw signal is sampled and filtered based on a predicted Doppler for the occultation (Sokolovskiy, 2001). Open-loop tracking can extend successful retrieval well into the atmospheric boundary layer, that part of the troposphere directly impacted by the Earth's surface (Sokolovskiy et al, 2006).

A technique to improve successful retrieval of bending angles in regions of complex atmospheric refraction, specifically when the atmosphere is not spherically symmetric, is the canonical transform method. In this method the coordinates for the observed phase data are transformed from geometric space into an impact parameter space. In this formulation refractive multipath does not occur; each ray is distinct in terms of its impact parameter (Gorbunov, 2002a).

The accuracy of the refractivity profiles derived from RO are on the order of a few percent, when compared to numerical predictions from the European Centre for Medium-Range Weather Forecasts (ECMWF). Accuracy of the corresponding temperature profiles is on the order of 1-2 degrees Kelvin (Wickert et al, 2003). An example of accuracies for CHAMP vs. ECMWF is shown in Figure 1.2. The shaded region is one standard deviation of error.

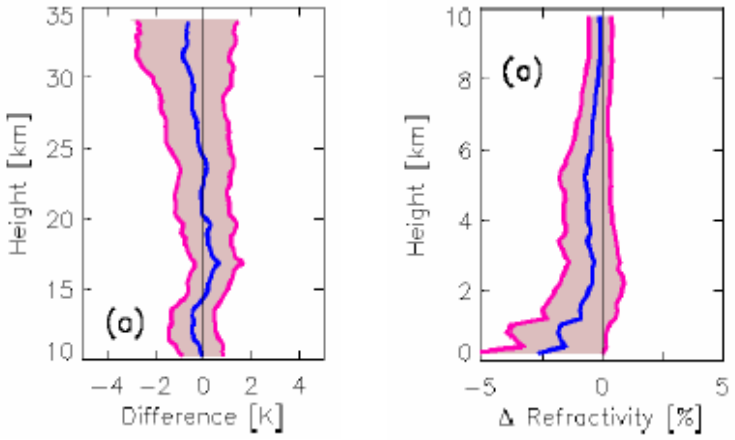

Figure 1.2: Example of accuracy of profiles derived from CHAMP (from Wickert et al, 2003)

Radiosonde observations provide another source of comparison data for RO. Radiosondes are packages of atmospheric sensors typically launched vertically through the atmosphere attached to weather balloons. The sensors record atmospheric parameters, including temperature and pressure, profiles of which can be produced when the instrument is recovered. Agreement between RO and radiosonde comparable to ECMWF agreement has also been shown (Marquardt et al, 2002).

In Canada, the primary source for numerical weather data is not ECMWF, but rather the Global Environmental Multiscale (GEM) model run by the Canadian Meteorological Centre (CMC), a branch of Environment Canada. The GEM model is a variable resolution model designed as a tool to assist weather forecasting, climatology, and air quality assessment (Côté et al, 1998). The operational regional resolution of the model is 0.33ºx0.33º, which applies over most of North America as shown in Figure 1.3. The

model output contains fields for geopotential height, temperature, humidity, and others for 28 isobaric levels. Forecasts are produced twice a day for three hour intervals.

Figure 1.3: Extent of regional operational resolution of the GEM model (from Côté et al, 1998)

Currently, RO data is not among the data types assimilated into the operational runs of the GEM model at CMC. However, a study was done into the effect of assimilating these data products into the forecast system (Aparicio & Deblonde, 2004). Data from CHAMP and SAC-C were included as input into the model, and the result compared to model output without RO measurements. In general, there was an improvement in forecast accuracy with RO data included, at the expense of some additional processing time.

1.2. Objectives

It is expected that integration of RO data products into operational meteorology and climatology will see increasing focus in Canada in the coming years. However, the majority of the existing research on RO has focused on either European or global events, and has used the ECMWF model for required inputs. It is the aim of this thesis to examine measurements of occultations occurring over Canada, using instead the GEM model, to provide a framework for any future Canadian occultation work using this model. This work has the following primary goals:

- to assess the requirements for orbital and boundary condition accuracy for temperature retrievals for Canadian weather conditions specifically.
- to assess the requirements for occultation-derived refractivity and NWP temperature profile accuracy to compute humidity retrievals for Canadian weather conditions.
- to assess the suitability of the GEM model as a source of temperature boundary conditions for temperature profile retrieval, and as a source of temperature profiles for humidity retrieval.

In order to achieve these goals, three regions have been selected as providing a cross section of Canadian weather. These are the arctic, the maritime region of Eastern Canada, and the prairies (the arid central region). Three occultations have been selected from each of these regions from each of the three month summer and winter seasons. Thirty-seven additional events occurring over Canada were selected to supplement the

data set. Each of these occultations is compared to corresponding CHAMP products and radiosonde data.

1.3. Outline

Chapter 2 of this thesis provides a technical overview of the GPS observables as they pertain to radio occultation. The GPS phase observable is discussed, along with the errors associated with it and the necessary corrections required to mitigate ranging errors relevant to occultation retrieval. Following a discussion of the observable, the equations used to extract excess atmospheric phase delay from raw GPS data are presented. Chapter 3 describes how the excess atmosphere phase delay can be used to compute a refractivity profile, along with how to obtain temperature and humidity profiles from refractivity, following established algorithms.

Original research begins in Chapter 4, which presents sensitivity analyses of the radio occultation retrievals to errors in satellite orbits and temperature boundary values. The effect of refractivity and input temperature error on humidity retrieval is also discussed. Requirements for the level of these errors in order to perform successful retrievals are estimated and discussed.

Chapter 5 includes the results of temperature and humidity retrieval using GEM temperature data as input. Multiple scenarios for selecting a temperature boundary condition are examined. Humidity retrievals are performed using GEM temperature

profiles as input. Accuracies of retrieved temperature and humidity profiles are assessed against CHAMP products and radiosondes.

Chapter 6 summarizes the major conclusions and findings of this research.

Chapter 2 - Background to the atmosphere and GPS

2.1. The Earth's atmosphere

In the context of radio navigation, the Earth's atmosphere consists of two regions. The troposphere, or neutral atmosphere, is the portion of the atmosphere that has a non-dispersive refraction effect on radio signals. The ionosphere is that portion of the atmosphere which contains free electrons, and consequently is dispersive at radio frequencies. The troposphere extends from the surface to roughly 50-70 km; the ionosphere exists between roughly 60 and 1000-1500 km (Figure 2.1).

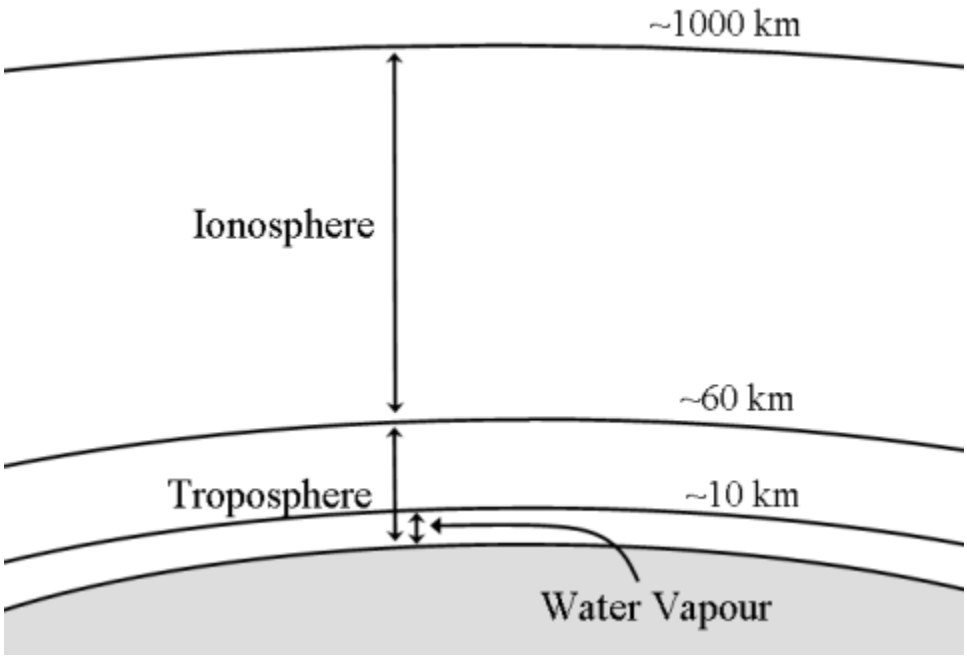

Figure 2.1: Structure of the atmosphere

This definition of the troposphere is in contrast to the meteorological definition of the regions of the atmosphere, in which the atmosphere is broken down in to various strata

based on inflections in the temperature profile. In meteorology, the troposphere is defined as the lowest region of the atmosphere and in which temperature decreases with height. It contains effectively all of the atmosphere's water vapour. It has a usual thickness of 10-12 km, and the local minimum of temperature that marks the upper boundary is known as the tropopause.

In this work, the terminology used is that of the radio navigation community. The troposphere is the entire region of the atmosphere having a non dispersive effect on GPS signals. While the location of the tropopause is relevant to define the height below which water vapour is present, no distinction is made in terminology between the atmosphere above and below the tropopause.

A typical temperature and pressure profile of the troposphere is shown in Figure 2.2. Temperature is generally decreasing with altitude until the tropopause, then begins to increase. Here the tropopause occurs at roughly 12 km. Pressure increases exponentially with decreasing height. Values are taken from the MSISE-90 (mass spectrometer incoherent scatter) empirical model (Hedin, 1991).

The typical delay on a GNSS signal passing through the ionosphere at zenith is on the order of 15 m. The typical tropospheric delay at zenith is on the order of 2.4 m (Lachapelle, 2004).

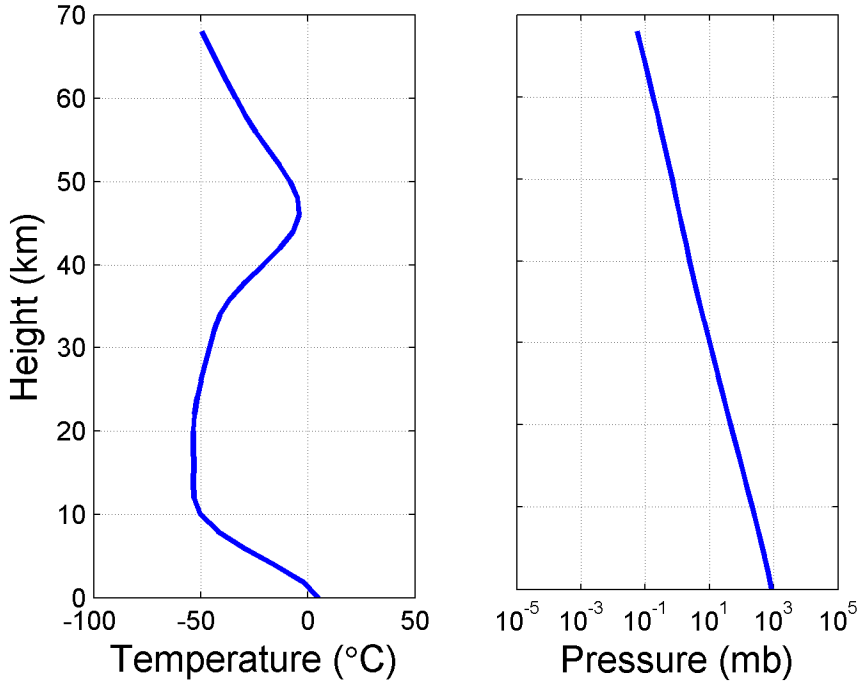

Figure 2.2: Typical temperature and pressure profiles in the troposphere

2.2. The Global Positioning System

The Global Positioning System (GPS) is comprised of space, user, and control segments. The space segment consists of the satellites, of which there are a minimum of 24, arranged in 6 orbital planes. Each plane is inclined at 55º, with 60º of separation between the right ascension of the ascending node of adjacent planes. The orbits are circular, having an altitude of ~20,200 km. This corresponds to an orbital period of one-half a sidereal day, so that two complete revolutions are completed each day. In February 2008 there were 31 active satellites.

The system uses two carrier signals at frequencies known as L1 and L2: 1575.42 MHz and 1227.60 MHz respectively. The system uses Code Division Multiple Access (CDMA) to differentiate between the different satellites broadcasting on the same frequency. Each satellite is assigned a unique Pseudo-Random Noise (PRN) code, which is modulated on the signals transmitted from that satellite. Two PRNs are used, a coarse acquisition (C/A) code which is public and intended for civilian use, and a precise (P) code intended for the military. A navigation message is also modulated onto the signal, containing information about the satellite clocks and orbits. Each member of the user segment computes their own position, using the signals broadcast from the satellites.

The control segment consists of a number of monitoring stations at various locations on the ground, with a master control station at Colorado Springs. The control segment monitors the orbits of the satellites, and computes the current orbital parameters. These are periodically uploaded to the satellites to update the navigation message which is broadcast to the users. The control segment also maintains the synchronization of the atomic clock onboard each satellite to a common time frame.

For a more thorough description of the GPS and signal structure, the reader is referred to many standard references (e.g. Parkinson & Spilker eds., 1996, Kaplan & Hegarty eds., 2006). Of primary relevance for this work are the errors on the carrier phase observable, and how they are reduced to compute excess phase delay.

2.3. The carrier phase observable

The carrier phase observation can be described by the following equation (after Lachapelle, 2004):

$$\phi = \rho + d\rho + cdt + cdT + \lambda N + trop - iono + \varepsilon_m + \varepsilon \tag{2.1}$$

with,

ϕ,	phase observation
ρ,	true geometric range
$d\rho$,	orbital errors
c,	speed of light
dt,	receiver clock error
dT,	satellite clock error
λ,	wavelength of signal
N,	integer ambiguity
$trop$,	troposphere (neutral atmosphere) error
$iono$,	ionosphere error
ε_m,	multipath
ε,	noise

All quantities can be expressed in units of either length or phase angle.

The goal of atmospheric retrieval is to isolate and solve for the troposphere delay, which requires elimination or minimization of all other error sources. In conventional positioning applications, true geometric range is an unknown quantity. In atmospheric retrieval, it is assumed that the receiver position is known, and thus the geometric range becomes a known quantity. Errors in the known receiver position will contribute to $d\rho$. Phase noise is typically at a level of 1-2 mm (Lachapelle, 2004). Each of the remaining error terms is discussed briefly below.

2.3.1. Orbital error

Errors in the GPS satellite positions as calculated from the broadcast orbits are on the order of 1-6m, with the majority of the error occurring in the along-track direction of the orbit (Kaplan & Hegarty, 2006). When the errors are projected onto the line-of-sight vector, magnitudes are typically on the order of 0.8 m. To minimize this error precise orbits are used, which are derived from the combined solutions of multiple data processing centres worldwide. A common source for precise orbit products is the International GNSS Service (IGS), which produces a post-mission precise orbit product with accuracies better than 5 cm (IGS, 2007).

In radio occultation applications, $d\rho$ is the sum of the position error of both the GPS and LEO satellites, as the LEO position must be known to extract the tropospheric delay. It is therefore necessary to model the orbit of the LEO with high accuracy as well. This can

be accomplished through application of a reduced-dynamic approach, in which an appropriate dynamic model is supplemented by GPS observations introduced as artificial accelerations. Other alternatives are pure dynamic modeling, a purely kinematic approach using only GPS observations, and a reduced-kinematic approach where the position solution is driven by the GPS observations, but dynamic information is included as a constraint. For further reading, see e.g. Wu et al (1991), Svehla & Rotacher (2005).

2.3.2. Satellite Clock Error

Each satellite is equipped with a precise cesium or rubidium atomic clock. The synchronization error and drift of each clock is monitored by the control segment, which uploads corrections to be included in the navigation message. Residual clock error, *dT*, after the corrections is on the order of 1-13 ns, corresponding to 0.3-4 m (denoted *cdT)*, (Kaplan & Hegarty, 2006). This error can be minimized by applying precise clock solutions. The IGS precise clock product is accurate to less than 1ns (30cm) (IGS, 2007). The term *cdT* can also be completely eliminated by differencing, as is described in section 2.3.4 below.

2.3.3. Receiver Clock Error

No external corrections exist for the receiver clock error, *cdt*, to allow it to be minimized in the same manner as *cdT*, as receivers are not typically equipped with precise clocks. The instability of the receiver clock requires that *cdt* must be estimated as a parameter, or

be eliminated by differencing. All simultaneous measurements made by a receiver share the same *cdt*. Therefore, by forming the difference between the measurements to two different GPS satellites, the common quantity *cdt* is removed.

2.3.4. Differencing in Radio Occultation

It is possible to use either a single or double difference technique in radio occultation. Both require a second, or base, satellite, which should be non-occulting in order that the ray path from the LEO to the satellite will not travel downward and enter the Earth's atmosphere. This will mean that the signal only encounters the atmosphere at altitudes above the LEO and should not experience significant tropospheric effects (see Figure 2.3).

In the single difference case, for two GPS satellites A (occulting) and B (base), neglecting for now the true range, satellite clock, orbital, ambiguity, and multipath errors from equation 2.1, the difference is as follows:

$$\begin{aligned} \phi^A &= cdt + trop^A - iono^A + \varepsilon \\ \phi^B &= cdt - iono^B + \varepsilon \\ \Delta\phi^{AB} &= \phi^A - \phi^B = trop^A - \Delta iono^{AB} + \varepsilon \end{aligned} \tag{2.2}$$

The resulting difference now contains only the troposphere delay to the occulting satellite, the differenced ionosphere delay, and noise.

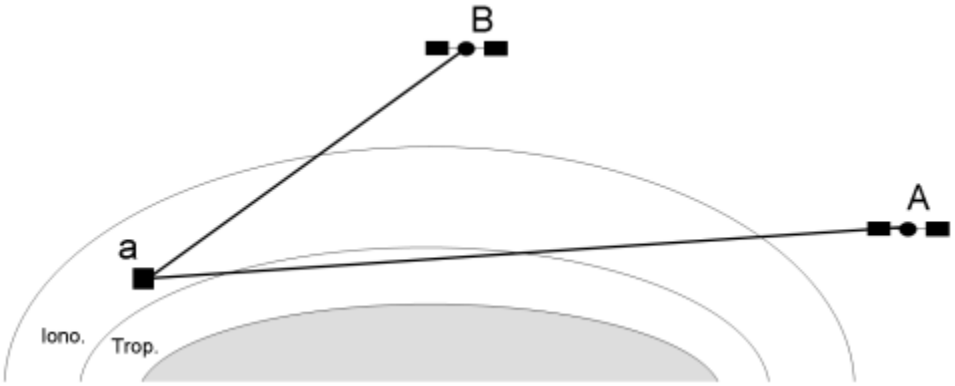

Figure 2.3: Radio occultation single difference

It is also common to form a double difference, where the between-satellite single difference at two different receivers is then differenced again. This has the advantage of completely removing *cdT*, eliminating the residual centimetre-level error present in the IGS precise clocks. The second receiver in this case is typically a ground station (see Figure 2.4). This is the procedure followed in processing for both the CHAMP and GPS/MET missions (Ware et al, 1996, Wickert et al, 2003). For two receivers *a* (LEO) and *b* (ground station) to the transmitters *A* and *B* in equation 2.2, the double difference (denoted by $\nabla\Delta$) is as follows:

$$\begin{aligned}
\Delta\phi_a^{AB} &= trop_a^A - \Delta iono_a^{AB} + \varepsilon \\
\Delta\phi_b^{AB} &= \Delta trop_b^{AB} - \Delta iono_b^{AB} + \varepsilon \\
\nabla\Delta\phi_{ab}^{AB} &= \nabla\Delta trop_{ab}^{AB} - \nabla\Delta iono_{ab}^{AB} + \varepsilon
\end{aligned} \tag{2.3}$$

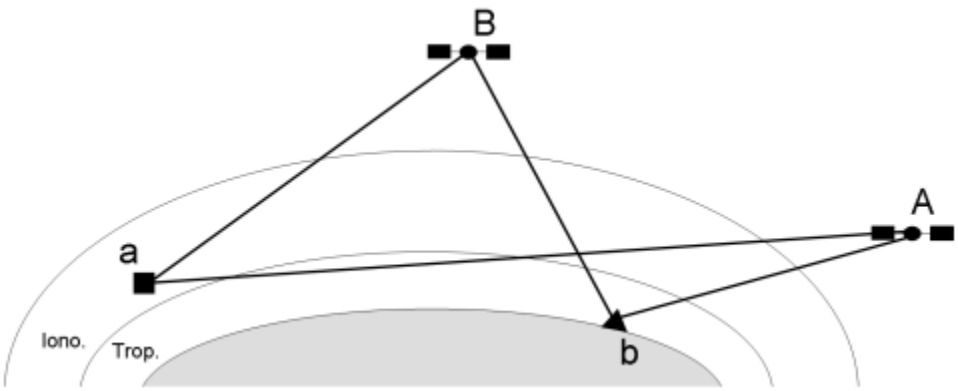

Figure 2.4: Radio occultation double difference

Note that the base station is not above the troposphere as the LEO is, and so experiences tropospheric delay on signals to both satellites. The double differenced tropospheric error in equation 2.3 thus contains tropospheric delays from three ray paths:

$$\nabla\Delta trop_{ab}^{AB} = \left(trop_{a}^{A}\right) - \left(trop_{b}^{A} - trop_{b}^{B}\right) \tag{2.4}$$

In order to extract the troposphere delay from the LEO to the occulting satellite ($trop_{a}^{A}$) for the retrieval, the tropospheric delays on the signals received at the ground station must be eliminated. This can be achieved by applying a tropospheric correction product, in which the tropospheric delay at the ground station has been computed to high accuracy. The IGS provides a tropospheric delay product which is accurate to 4 mm (IGS, 2007). When the tropospheric delays to the ground station have been corrected, the double difference contains only the troposphere delay from the LEO to the occulting satellite, the double differenced ionosphere delay, and noise.

Testing by Wickert et al (2002) suggests that the single and double difference techniques provide statistically identical results following the removal of Selective Availability (intentional dithering of the satellite clocks prior to May 2, 2000).

2.3.5. Integer ambiguity

The integer ambiguity *N* represents the number of whole cycles in the carrier phase between the transmitter and receiver. As the receiver only measures the incident phase of the wave, the ambiguity is unknown, and the measurement does not represent the full range to the transmitter. In positioning applications, it is necessary to resolve the ambiguity in order to compute positions from the phase measurement. Radio occultation however, requires only the time difference of the excess phase measurement, or atmospheric Doppler, which is described in Chapter 3. As *N* remains constant with time, it is eliminated in the time-differenced measurement.

2.3.6. Multipath

Multipath error is caused by multiple signals traveling along different paths and arriving at the receiver at the same time, resulting in interference. In conventional applications multipath typically results from signals striking nearby surfaces and reflecting towards the receiver. For a satellite, only signals reflecting off other surfaces of the satellite before reaching the receiver will be present, as there are no other local reflectors. In

radio occultation, multipath of this nature is typically grouped with noise (e.g. Hajj et al, 2002; Wickert et al, 2001b).

A second form of multipath is present in radio occultation, which results from signals taking different paths through the atmosphere on the way to the LEO. This can result from complicated structure of the lower troposphere, especially in the tropics, and also from ground reflected signals (Gorbunov, 2002b). Multipath of this nature can cause severe signal degradation, leading to loss of lock, or introducing errors into the retrieved parameters. Smoothing of the data can eliminate higher frequency multipath effects, but at the cost of information about small scale atmospheric structure (Gorbunov & Gurvich, 1998).

Accuracy of retrievals in the presence of atmospheric multipath effects can be greatly improved through the application of the canonical transform (CT) method (Gorbunov, 2001, Gorbunov, 2002a). In this method, the spatial coordinates of each ray are transformed into a ray coordinate space, defined by impact parameter. In this space, the derivative of the ray phase is the bending angle. This method is applicable in any case where the rays can be uniquely defined by impact parameter. While this is sometimes not the case in the presence of strong horizontal refractivity gradients, such conditions are rare (Gorbunov, 2001). In this work the CT method is not applied; only the conventional geometric optics approach (described in Chapter 3) is used, as extending retrievals into very low altitudes is not a primary objective of this work.

Chapter 3 - Derivation of atmospheric parameters from excess phase delay

Following the error corrections described in Chapter 2, what remains is the excess phase delay caused by the atmosphere as the GPS signal travels through it. This excess delay is the sum of both tropospheric and ionospheric contributions, on both GPS frequencies. In this work, the excess phase delay product from the CHAMP mission is used as the input data and the procedures described in Chapter 2 are conducted as part of the pre-processing by the CHAMP data centre. The CHAMP phase measurements are given in units of length, not phase angle, and this convention will be maintained throughout this work.

This chapter outlines the steps required to derive profiles of refractivity, temperature, pressure, and humidity from the excess phase delay data. These steps were implemented with original software in this work, based on established algorithmns (see e.g. Vorob'ev & Krasil'nikova,1993, Syndergaard, 1998, Steiner et al, 1999, Hajj et al, 2002).

3.1. Spherical approximation of the atmosphere

In order to derive bending from the excess delay, it is necessary to assume that the atmosphere is spherically symmetric. In making this assumption, the positions and velocities of the LEO and occulting GPS satellite must be expressed relative to a spherical approximation to the Earth, which is tangential to the Earth at the location of

the occultation. The location of the occultation is also referred to as the tangent point (see Figure 3.1).

The tangent point of the occultation is ideally defined as that point on the Earth where the inter-satellite vector is tangent to the surface. For this it is appropriate to approximate the Earth with an ellipsoid. In this work the WGS-84 ellipsoid is used, as it is the reference frame for GPS. However, the problem of intersecting a line in an arbitrary plane with an ellipsoid is non-trivial. Instead of a direct solution for the tangent point, a simpler method is used. For all epochs of the occultation, the point on the inter-satellite vector closest to the origin of the coordinate system (earth centre of mass) is calculated. Each of these points is transformed into a set of curvilinear coordinates on the WGS-84 ellipsoid. The point having the smallest magnitude of the height coordinate is treated as being most tangential to the ellipsoid. The profile location is then defined as having the same latitude and longitude of that point, with a height of 0 m.

Once the tangent point of the occultation is defined, it remains to find the sphere which is tangential to the ellipsoid at that point, and has the same radius of curvature. This is achieved by finding the circle lying in the occultation plane having the same radius of curvature and tangent to the ellipsoid. The radius of the circular approximation is computed using equations 3.1 to 3.6. An example, not to scale, is shown in Figure 3.1. The occultation plane is defined here and throughout this work as the plane containing

the LEO, occulting GPS satellite, and the origin, at the epoch from which the tangent point is defined. The implementation in this work follows that of Syndergaard (1998).

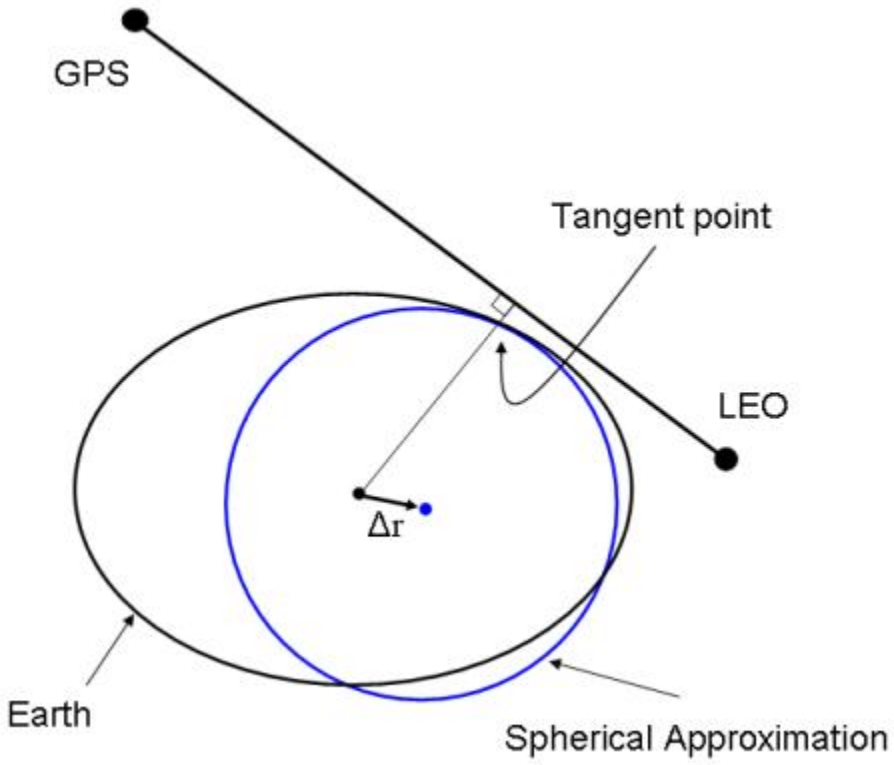

Figure 3.1: Spherical approximation to the earth at the tangent point

The colatitude, θ, of the tangent point, which is the angle between the positive z axis and the point, is given by:

$$\theta = \arccos\left(\frac{z}{\sqrt{x^2 + y^2 + z^2}}\right) \tag{3.1}$$

with x, y, z, the Cartesian coordinates of the tangent point with respect to the ellipsoid origin. The geocentric radius at this point, R, is given to first order as:

$$R = a\left(1 - f\cos^2\theta\right) \tag{3.2}$$

where a and f are the semi-major axis and flattening of the ellipsoid, respectively. The local normal vector to the ellipsoid at this point is given as:

$$\vec{n}_s = \begin{pmatrix} \tilde{x} \\ \tilde{y} \\ \tilde{z} \end{pmatrix} - 2f\tilde{z}\begin{pmatrix} \tilde{x}\tilde{z} \\ \tilde{y}\tilde{z} \\ \tilde{z}^2 - 1 \end{pmatrix} \tag{3.3}$$

where $\tilde{x}$, $\tilde{y}$, and $\tilde{z}$ are the components of the unit vector in the direction of the origin, given by the latitude and longitude of the tangent point, φ and λ:

$$\begin{pmatrix} \tilde{x} \\ \tilde{y} \\ \tilde{z} \end{pmatrix} = \begin{pmatrix} \cos\varphi\cos\lambda \\ \cos\varphi\sin\lambda \\ \sin\varphi \end{pmatrix} \tag{3.4}$$

The vector radius of curvature at this point, $\vec{R}_c$, is given by:

$$\vec{R}_c = \frac{\vec{n}_s}{\left|d\vec{n}_s / ds\right|} \tag{3.5}$$

$$\frac{d\vec{n}_s}{ds} = J_s\vec{n}_p \tag{3.6}$$

with $d\vec{n}_s/ds$ being the derivative along the surface in the occultation plane, and $\vec{n}_p$ being a unit vector parallel to the surface in the occultation plane. The inter-satellite vector

used to define the tangent point is used as an approximation to $\vec{n}_p$. A closed form solution for the matrix J_S is given by Syndergaard (1998). With $\vec{R}_c$ known, the centre of the circular approximation is found by subtracting it from the coordinates of the tangent point, P.

$$\Delta r = P - \vec{R}_c \tag{3.7}$$

All coordinates of the LEO and occulting GPS satellite are then calculated using Δr as the origin, and these new coordinates are used throughout the remainder of the retrieval. Also, the radius of the circle, $|\vec{R}_c|$, is used in place of the Earth radius whenever necessary.

3.2. Deriving atmospheric Doppler from excess phase

It is necessary to compute from the excess phase delay the atmospheric Doppler, which is not Doppler in the conventional sense, but rather the time derivative of the excess phase delay on the signal caused by the atmosphere. Following the implementation of Hajj et al (2002) the excess phase is smoothed over the length of time necessary for the signal to vertically cross the first Fresnel zone, which is the region through which the majority of the signal power travels. Diffraction caused by refractivity structures in the atmosphere smaller than the diamteter of the first Fresnel zone can cause interference with the direct signal, limiting the effective resolution of the technique to the size of the Fresnel zone.

Smoothing across this distance removes diffraction effects from the final signal. The time is computed based on the size of the Fresnel diameter, and the vertical velocity of the tangent point of the ray. The formulae for computing the smoothing time are given as follows:

$$F_0 = \sqrt{\frac{\lambda D_{GPS} D_{LEO}}{D_{GPS} + D_{LEO}}} \tag{3.8}$$

$$M = \left(\frac{SNR}{SNR_0} \right)^2 \tag{3.9}$$

$$T = \frac{2F_0}{V_0 \sqrt{M}} \tag{3.10}$$

with

F_0, the magnitude of the first Fresnel diameter

λ, the wavelength of the signal

D_{GPS}, D_{LEO}, the distance from the ray tangent point to the occulting GPS satellite and LEO, respectively

M, an atmospheric scale factor

SNR, SNR_0, the observed signal to noise ratio and signal to noise ratio in free space, respectively

T, the time for the signal to cross the Fresnel diameter

V_0, the vertical velocity of the tangent point

The tangent point of the ray at a given epoch is defined as described in section 3.1, as the point on the inter-satellite vector nearest the origin. The vertical velocity of the tangent point is computed simply as the derivative of the time series of the tangent point height at each epoch. Signal to noise ratio of the C/A code signal is recorded by the CHAMP satellite for the duration of the occultation. The SNR in free space is approximated by the SNR for the first epoch of the data for a setting occultation, before the occultation event has begun (last epoch for a rising occultation).

For each epoch, a second order polynomial is fit using a least squares estimate to the excess phase data within a window of size T centred on the epoch. The atmospheric Doppler at that epoch is then computed as the analytical derivative of the polynomial fit. The sign convention for atmospheric Doppler employed in this work is that increasing range rate or increasing excess phase (as in a descending occultation) gives negative Doppler.

3.3. Deriving bending from atmospheric Doppler

From the atmospheric Doppler, the bending experienced by the ray can be derived. The observed atmospheric Doppler can be expressed as the difference between the geometric Doppler (Doppler expected in the absence of the atmosphere), and the actual Doppler along the true bent ray path. Refer to Figure 3.2 for a depiction of the geometry and definition of several geometric quantities. All velocities are projected into the occultation plane.

The geometric Doppler, d_g, is simply the difference of the projection of the two satellite velocities onto the inter-satellite vector:

$$d_g = v_{GPS} \cos \phi_{GPS} + v_{LEO} \cos \phi_{LEO} \tag{3.11}$$

with ϕ_{GPS} being the angle between the velocity vector of the GPS satellite and the inter-satellite vector, and ϕ_{LEO} being the corresponding angle for the LEO. Note that the LEO velocity projection is positive in equation 3.11 because it is being projected onto the negative of the inter-satellite vector.

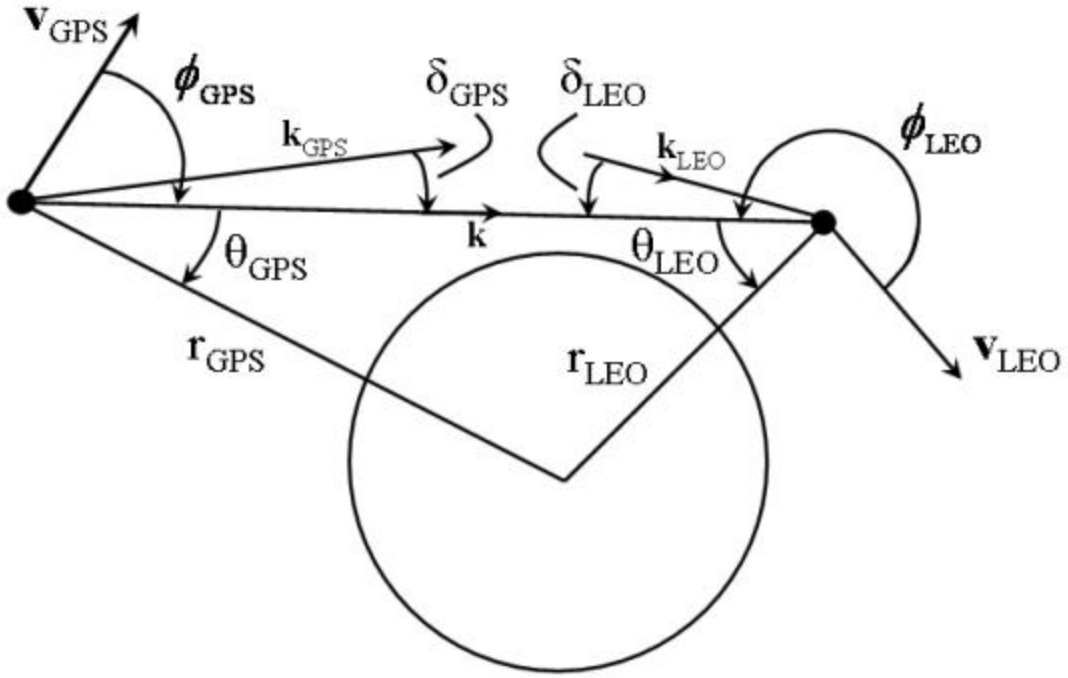

Figure 3.2: Occultation geometry with angular quantities

The actual Doppler is the projection of the satellite velocities onto $\boldsymbol{k}_{GPS}$ and $\boldsymbol{k}_{LEO}$, the respective vectors in the direction of the actual bent signal path at either end. This value is expressed as follows:

$$d = v_{GPS}\cos(\phi_{GPS} - \delta_{GPS}) + v_{LEO}\cos(\phi_{LEO} - \delta_{LEO}) \tag{3.12}$$

And the atmospheric Doppler as discussed in section 3.2, d_a, is then:

$$\begin{aligned} d_a = d - d_g = &\left(v_{GPS}\cos(\phi_{GPS} - \delta_{GPS}) + v_{LEO}\cos(\phi_{LEO} - \delta_{LEO})\right) \\ &- v_{GPS}\cos\phi_{GPS} + v_{LEO}\cos\phi_{LEO} \end{aligned} \tag{3.13}$$

All quantities save for δ_{GPS} and δ_{LEO} are known, or can be computed from the satellite positions and velocities. Note that the actual geometry can vary significantly from that depicted, depending on the direction of the GPS satellite velocity, and whether the occultation is rising (LEO approaching the GPS satellite) or descending (LEO receding from the GPS satellite). In order that formulae are correct for all cases, care must be taken when solving for ϕ_{GPS} and ϕ_{LEO} to ensure that they are correctly the clockwise angle from $\boldsymbol{v}_{GPS}$ to $\boldsymbol{k}_{GPS}$ and $\boldsymbol{k}_{LEO}$ to $\boldsymbol{v}_{LEO}$, respectively. This ensures that the subtraction of the δ angles from their respective ϕ values is consistent with assumed conventions. If the computed angles are clockwise, the following expressions apply:

$$\begin{aligned} &(\mathbf{k}_{GPS} \times \mathbf{v}_{GPS}) \cdot \mathbf{n} > 0 \\ &(\mathbf{v}_{LEO} \times \mathbf{k}_{LEO}) \cdot \mathbf{n} > 0 \end{aligned} \tag{3.14}$$

with n being the normal vector to the occultation plane, defined as $\boldsymbol{r}_{LEO} \times \boldsymbol{r}_{GPS}$.

Angles δ_{GPS} and δ_{LEO} represent the deflection from the straight line ray path at either end of the ray. Their sum is the total atmospheric bending angle, α.

$$\alpha = \delta_{GPS} + \delta_{LEO} \tag{3.15}$$

In order to solve for the bending, Snell's Law is introduced as a second equation with these variables.

$$\mathbf{r}_{GPS} n_{GPS} \sin(\theta_{GPS} + \delta_{GPS}) = \mathbf{r}_{LEO} n_{LEO} \sin(\theta_{LEO} + \delta_{LEO}) \tag{3.16}$$

where n_{GPS} and n_{LEO} are the indices of refraction at the GPS satellite and LEO respectively. It is assumed that at both the satellites' locations the index of refraction is equal to 1. This equation assumes spherical symmetry of the atmosphere, which is the reason for reducing all coordinates to the spherical approximation introduced in section 3.1.

Solving both equations simultaneously with Newton's method yields the total bending angle α. The impact parameter, a, is also computed, which is the distance from the origin to the point on the ray path on either side of the atmosphere at which bending begins (see Figure 3.3).

$$a = r_{GPS}\sin\left(\theta_{GPS} + \delta_{GPS}\right) = r_{LEO}\sin\left(\theta_{LEO} + \delta_{LEO}\right) \tag{3.17}$$

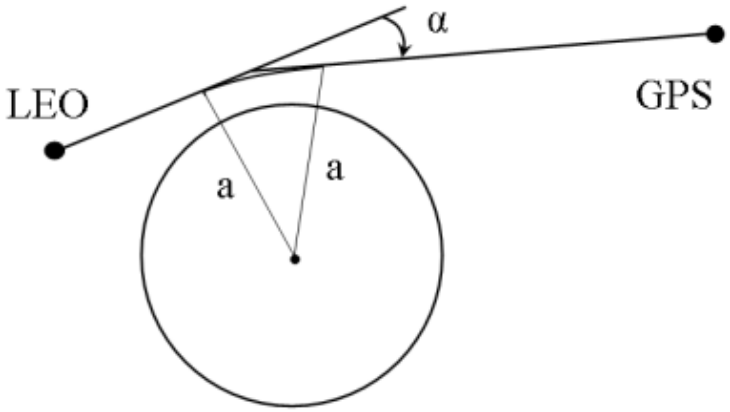

Figure 3.3: Bending angle α and impact parameter a

3.4. Dual frequency removal of ionospheric delay

Computation of atmospheric Doppler, bending angle, and impact parameter is performed on both frequencies independently. As such, the computed bending remains the sum of both tropospheric and ionospheric contributions. Since the ionosphere is dispersive at GPS frequencies, the L1 and L2 frequency signals will be bent by different amounts. This can be exploited to obtain the bending due to propagation only in the troposphere, α_{IF}, by linearly combining the L1 and L2 bending angle profiles (Vorob'ev & Krasil'nikova, 1993).

$$\alpha_{IF}(a) = \frac{f_{L1}^2 \alpha_{L1}(a) - f_{L2}^2 \alpha_{L2}(a)}{f_{L1}^2 - f_{L2}^2} \tag{3.18}$$

It is necessary that both the L1 and L2 bending angles correspond to the same impact parameter. To achieve this, the L2 bending angle profile is interpolated to the impact parameters of the L1 profile using a cubic spline.

As the profile begins to descend into the troposphere, poor signal tracking on L2 results in severely degraded performance. The L2 signal begins to experience increased noise and frequent cycle slips, which prevent using L2 observations directly in the linear combination above. L2 tracking is affected more than L1 because the squaring techniques required to track the L2 signal result in a signal power loss of at least 17 dB. Steiner et al (1999) propose three solutions to the problem. The method implemented in this work is to model the difference between the bending angles calculated from the two frequencies as being linearly dependant on height below 25 km altitude. A total of 101 data points are taken and averaged at 25 km and 15 km to define the linear relationship. Below 12.5 km (an approximate value for the tropopause), L2 bending angles are replaced by L1 bending angles with an additional component extrapolated from the linear relationship.

3.5. Deriving index of refraction from bending angles

The bending angle profile can be related to the index of refraction, *n*, by the following integral (e.g. Fjeldbo et al, 1971, Hajj et al, 2002):

$$\alpha(a) = 2a\int_a^\infty \frac{1}{\sqrt{x^2 - a^2}} \frac{d\ln(n)}{dx} dx \tag{3.19}$$

In order to solve for *n* given *α(a)*, this integral can be inverted using an Abel integral transform, yielding the following:

$$\ln(n(a)) = \frac{1}{\pi}\int_a^\infty \frac{\alpha(a)}{\sqrt{x^2 - a^2}} dx \tag{3.20}$$

Applying integration by parts to this integral, the following expression is obtained:

$$\ln(n(a)) = \alpha(a)\ln\left(\frac{x}{a} + \sqrt{\left(\frac{x}{a}\right)^2 - 1}\right) - \int_a^\infty \ln\left(\frac{x}{a} + \sqrt{\left(\frac{x}{a}\right)^2 - 1}\right) \frac{d\alpha(a)}{dx} dx \tag{3.21}$$

Lastly, it is necessary to restructure the boundaries of the integral to avoid a singularity which occurs when $x = a$ (Hajj et al, 2002). The final integral is

$$\begin{aligned} \ln(n(a)) = \alpha(a)\ln\left(\frac{x}{a} + \sqrt{\left(\frac{x}{a}\right)^2 - 1}\right) \\ - \int_a^{a_{\text{int}}} \ln\left(\frac{x}{a} + \sqrt{\left(\frac{x}{a}\right)^2 - 1}\right) \frac{d\alpha(a)}{dx} dx + \int_{a_{\text{int}}}^\infty \frac{\alpha(a)}{\sqrt{x^2 - a}} \end{aligned} \tag{3.22}$$

with a_{int} being an intermediate value of impact parameter slightly higher than a. In this work, it is taken as the first profile point above the base of the profile a. This integral is solved numerically to yield a profile of index of refraction as a function of impact

parameter a. The tangent point radius, r, or distance from the origin to the tangent point of the ray, is given by $r = a/n$.

Above ~50 km, the residual ionospheric effect is comparable in magnitude to the bending caused by the neutral atmosphere (Hajj et al, 2002). Because of this, it is not practical to integrate the bending angle derived from the occultation upward to the top of the atmosphere as equation 3.22 would require. Instead, bending angles from a functional or climatological model are introduced at higher altitudes to allow the upward integration beyond the practical limits of the derived angles.

In this work, high altitude bending angles are taken from the MSISE-90 empirical model. The choice of the MSISE model for upper atmosphere bending angles is based on work by Steiner et al (1999). The occultation derived bending angles are combined with the MSISE bending angles between 50 and 60 km. At 50 km the occultation derived angle has full weight, and is progressively and linearly de-weighted in favour of the MSISE bending angles, which have full weight at 60 km. Above 60 km only the MSISE data is used. Integration is continued up to a height of 750 km.

3.6. Deriving temperature and humidity from index of refraction

Temperature, pressure, and water vapour pressure in the atmosphere can be related to the index of refraction by an empirical model. One common model is that of Smith and Weintraub (1953), which is used in this work.

$$N = 77.6\frac{P}{T} + 3.73\times10^{5}\frac{e}{T^{2}}$$
$$N = (n-1)\times10^{6} \tag{3.23}$$

with,

n, index of refraction

N, refractivity in parts per million

P, pressure in mbar

T, temperature in ºK

e, partial water vapour pressure in mbar

Hajj et al (2002) offer a second equation for temperature, pressure, and water vapour pressure, derived from the ideal gas law and the constraint of hydrostatic equilibrium.

$$\frac{dP}{dh} = -\frac{gm_{d}}{77.6R}N + \frac{3.73\times10^{5}\,gm_{d}}{77.6R}\frac{e}{T^{2}} + \frac{g(m_{d}-m_{w})}{R}\frac{e}{T} \tag{3.24}$$

with,

g, acceleration due to gravity (m/s2)

h, height in m

R, ideal gas constant

m_{d}, m_{w}, molecular mass of dry air (28.97 g/mol) and water vapour (18.0 g/mol)

Together these equations comprise a set of differential equations in three unknowns: P, T, and e.

Above the tropopause, where e is zero, pressure and temperature can be solved for by applying a boundary condition. Pressure and temperature can be solved below the tropopause by setting e to zero, but the resulting profiles will be biased as a result of neglecting the contribution of water vapour.

Below the tropopause, it is necessary to have *a priori* knowledge of one of the three terms (typically temperature) in order to accurately solve for the remaining two. If a temperature profile is provided, the pressure and humidity are solved by an iterative process (after Hajj et al, 2002).

a) Set $e = 0$
b) Compute a boundary value for P using equation 3.23
c) Integrate through the profile with equation 3.24 to solve for P
d) Using T and P in equation 3.23, solve for e
e) Repeat steps c and d until e converges

This yields a profile of the partial pressure of water vapour, e, as a function of height, along with the pressure, P, which takes into account the presence of water vapour. The

boundary value of P applied in this work is taken from the dry profile at 15 km, where there is no water vapour.

If dew point (the temperature at which water vapour pressure reaches the saturation point) is required (e.g. for comparison to radiosonde or NWP products), the saturation vapour pressure must first be computed. This is done using the Goff-Gratch equation (Goff & Gratch, 1946).

$$\begin{aligned}\log(e^*) = &-7.90298\left(\frac{T_{ST}}{T}-1\right)+5.02808\cdot\log\left(\frac{T_{ST}}{T}\right)\\ &-1.3816\times10^{-7}\left(10^{11.344(1-T_{ST}/T)}-1\right)\\ &+8.1328\times10^{-3}\left(10^{-3.49149(T_{ST}/T-1)}-1\right)+\log(e^*_{ST})\end{aligned} \tag{3.25}$$

with,

e^*	the saturation vapour pressure in hPa
T	the air temperature in ºK
T_{ST}	the steam point temperature (373.15 ºK)
e^*_{ST}	the saturation pressure at the steam point pressure (1013.25 hPa)

With saturation vapour pressure, the dew point is given by the following equation (derived from the Magnus-Tetens formula for vapour pressure (Barenbrug, 1974), after Paroscientific (2008)).

$$T_d = \frac{237.7 \cdot \alpha}{17.27 - \alpha}$$
$$\alpha = \frac{17.27 \cdot T}{237.7 + T} + \ln(RH) \tag{3.26}$$

with,

T, the temperature in ºC

RH, the relative humidity (e / e*)

3.7. Summary of occultation retrieval

A flowchart showing an overview of the retrieval process is shown in Figure 3.4. The section highlighted in orange represents steps that for this work were carried out at the CHAMP processing centre, and are described in Chapter 2. The section highlighted in blue represents steps implemented in this work, and described in Chapter 3.

The final product of the retrieval process is vertical profiles of refractivity, dry temperature and pressure if a boundary condition is available, and humidity if a complete temperature or pressure profile is available,

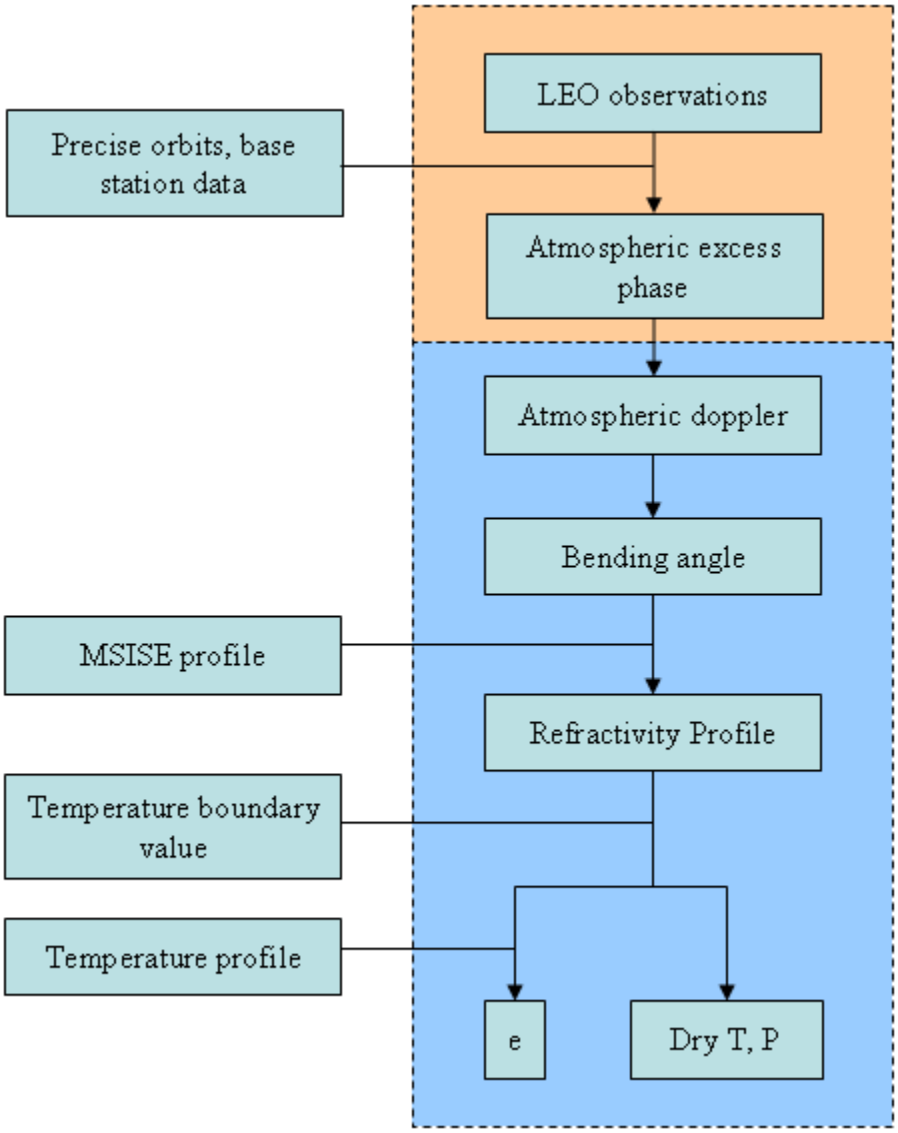

Figure 3.4: Overview of retrieval process

Chapter 4 - Error sensitivity analyses

The methods for retrieving temperature, pressure, and humidity described in Chapters 2 and 3 were applied using real occultation data and temperature data (boundary condition and full profile) from an NWP. Temperature and humidity profiles are produced as outlined in the previous chapters.

This chapter focuses on sensitivity analysis and error propagation for various error sources present in the input occultation and NWP data. The effect of orbital errors on the occultation measurements is examined, as well as the effect of boundary condition temperature errors in the boundary condition applied. The effect of errors in the input temperature profiles and in the occultation derived refractivity on the humidity profiles is also examined.

4.1. The CHAMP Mission

Data used in this work is from the Challenging Mini-satellite Payload (CHAMP) satellite, operated by GeoForschungsZentrum Potsdam (GFZ). CHAMP was launched on July 15, 2000, with the first data from the occultation experiment coming on February 11, 2001. CHAMP is a LEO with an orbital altitude of 454 km, an eccentricity of 0.04, and an inclination of 87.2º (Wickert et al, 2001c).

The initial data source for this work is the calibrated excess path delay product produced by GFZ, which consists of the signal delay after non-atmospheric error sources have been removed, as described in Chapter 2. Clock errors are removed in the CHAMP processing by double differencing with a ground station network consisting of ~40 stations (Wickert et al, 2003). Ground station data is sampled at 1 Hz for use in differencing to correct the clock errors. Occultation measurements are sampled at 50 Hz. Precise orbits for both the GPS and CHAMP satellites are computed by GFZ using a two step dynamic solution. In the first step, GPS satellite positions are estimated along with ground station coordinates. These are then held fixed and passed along with satellite clock corrections into the second step, where the LEO position is calculated using onboard GPS and accelerometer measurements with an appropriate dynamic model (König et al, 2002). GPS data for positioning of the LEO is sampled at a rate of 10 Hz. Comparison of the LEO orbit against satellite laser ranging (SLR) measurements yields residuals at the level of 6.8 cm RMS (Wickert et al, 2003).

4.2. Occultation Data Set

Occultation events were chosen by temporal and spatial collocation with radiosonde launch sites in Canada. A single event represents one time series of the LEO observing a setting GPS satellite. Initially, 18 events were selected to ensure representation of the range of seasonal and regional conditions in Canada. The events were classified by region, with three zones defined to cover a range of atmospheric conditions:

a) an arctic zone ranging from (62ºN, 60ºW) to (80ºN, 140ºW)

b) a maritime zone ranging from (44ºN, 50ºW) to (54ºN, 75ºW)

c) a prairie zone ranging from (49ºN, 100ºW) to (56ºN, 115ºW).

Three events from both the winter (December 2002 – February 2003) and summer (June – August, 2003) seasons were selected from each zone, to comprise the initial 18 events. A further 37 events between April 2003 and January 2004 were selected without regard to date or region to expand the data set, as no additional events meeting the original criteria and closely collocated with radiosonde launches were available. Figure 4.1 shows all 55 events and corresponding radiosonde launch locations. The distances and time differences from the nearest radiosonde launch are listed in Table 4.1.

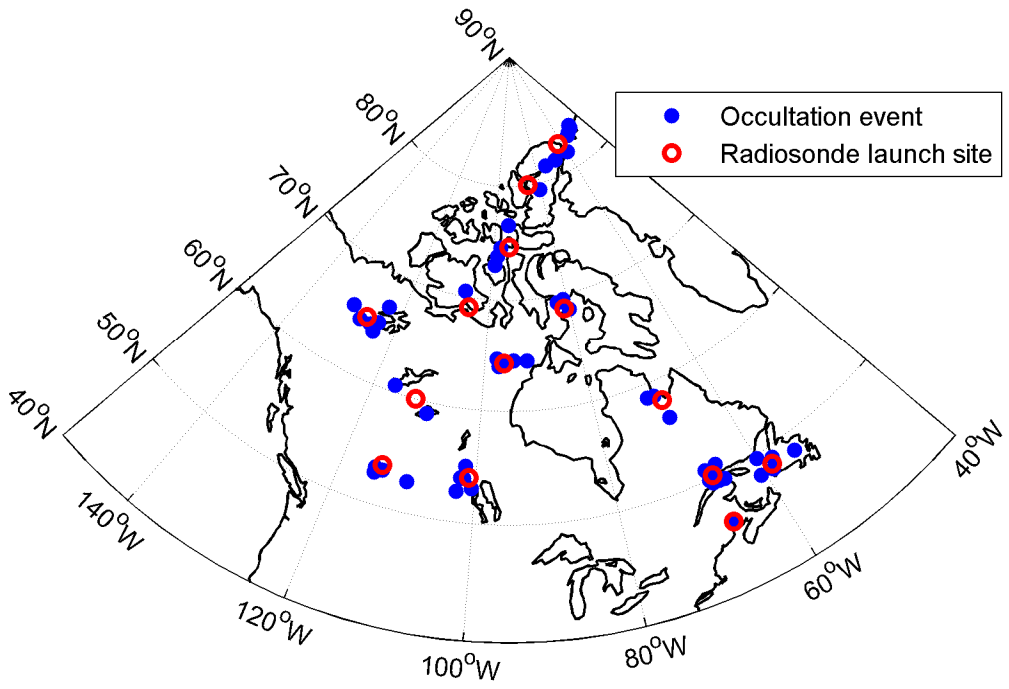

Figure 4.1: Locations of selected radio occultation events and corresponding radiosonde launch sites

Table 4.1: List of occultation events

#	Date	Distance to radiosonde (km)	Time from launch (min)	#	Date	Distance to radiosonde (km)	Time from launch (min)
1	Aug 13, 2003	94	89	29	May 27, 2003	244	8
2	Aug 16, 2003	91	22	30	May 31, 2003	124	-13
3	Aug 20, 2003	51	-56	31	Jun 1, 2003	156	22
4	Dec 18, 2002	92	-20	32	Jun 2, 2003	147	-23
5	Jan 26, 2003	87	-36	33	Jun 3, 2003	116	11
6	Jan 25, 2003	76	27	34	Jun 28, 2003	127	10
7	Aug 18, 2003	28	14	35	Jul 28, 2003	91	3
8	Aug 19, 2003	71	54	36	Aug 4, 2003	163	2
9	Aug 20, 2003	119	1	37	Aug 13, 2003	235	8
10	Dec 3, 2002	21	-45	38	Aug 14, 2003	158	-12
11	Dec 7, 2002	60	-71	39	Sep 6, 2003	26	32
12	Jan 3, 2003	88	-93	40	Sep 8, 2003	181	9
13	Jun 1, 2003	78	-59	41	Sep 9, 2003	75	-4
14	Jun 3, 2003	117	-69	42	Sep 23, 2003	65	-7
15	Aug 20, 2003	287	186	43	Sep 27, 2003	182	20
16	Dec 3, 2002	113	48	44	Sep 30, 2003	245	-8
17	Dec 30, 2002	180	7	45	Dec 12, 2003	192	-13
18	Jan 27, 2003	46	-116	46	Dec 17, 2003	145	-9
19	Apr 9, 2003	115	27	47	Dec 20, 2003	77	11
20	Apr 11, 2003	138	18	48	Dec 21, 2003	212	15
21	Apr 15, 2003	198	0	49	Dec 22, 2003	229	-12
22	Apr 18, 2003	184	-18	50	Dec 30, 2003	59	11
23	May 6, 2003	50	-19	51	Jan 1, 2004	249	-8
24	May 7, 2003	103	21	52	Jan 3, 2004	53	27
25	May 8, 2003	86	29	53	Jan 6, 2004	35	-8
26	May 9, 2003	71	11	54	Jan 11, 2004	108	-9
27	May 10, 2003	144	18	55	Jan 11, 2004	157	-11
28	May 12, 2003	226	8				

4.3. Common problems in retrievals

There are two fairly common problems with the occultation data which can lead to retrieved profiles which are, in whole or in part, unusable. The first is caused by poor tracking on the L2 signal at mid-altitudes. As discussed in section 3.4, L2 data is only used in forming the ionosphere-free (IF) bending angle above 12.5 km. Below this height, the IF bending angle is extrapolated from the L1 bending angle based on the trend

between L1 and L2 at higher altitudes. This is sufficient to produce realistic IF bending angles in the majority of cases. However, in some cases the L2 signal experiences significant cycle slips even above 12.5 km, which influence the IF bending angle. Bending angle profiles for one such event are shown in Figure 4.2.

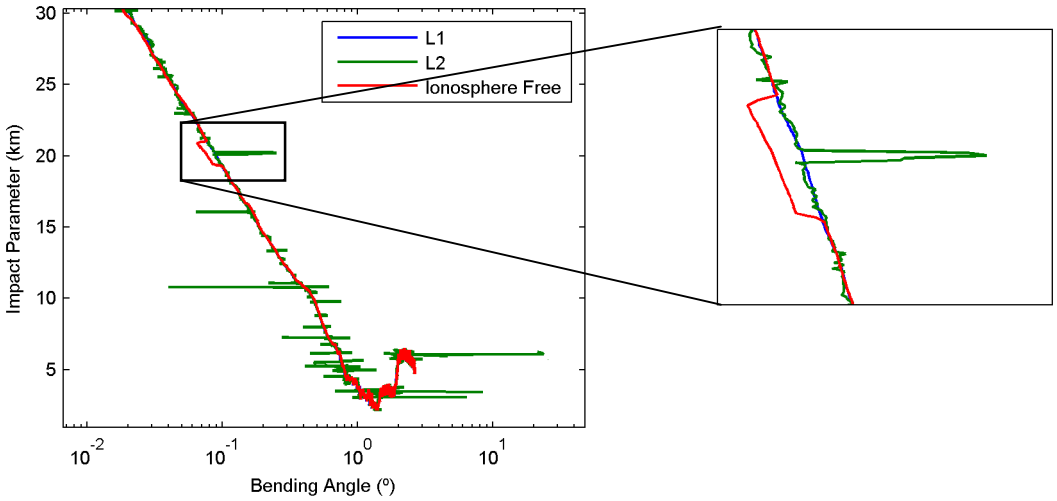

Figure 4.2: Bending angles for an event with poor L2 tracking above 12.5 km (Event 3 of Table 4.1)

A spike in the L2 bending angle caused by a cycle slip is clearly visible at 20 km. It has a direct effect on the ionosphere-free bending angle. The IF bending is biased with a lesser magnitude and over a larger altitude range as a result of a moving average filter being applied to smooth the IF bending angles. The effect of this spike on the temperature profile retrieved from this event is shown in Figure 4.3. There is a corresponding temperature error around 20 km caused by this bending angle error.

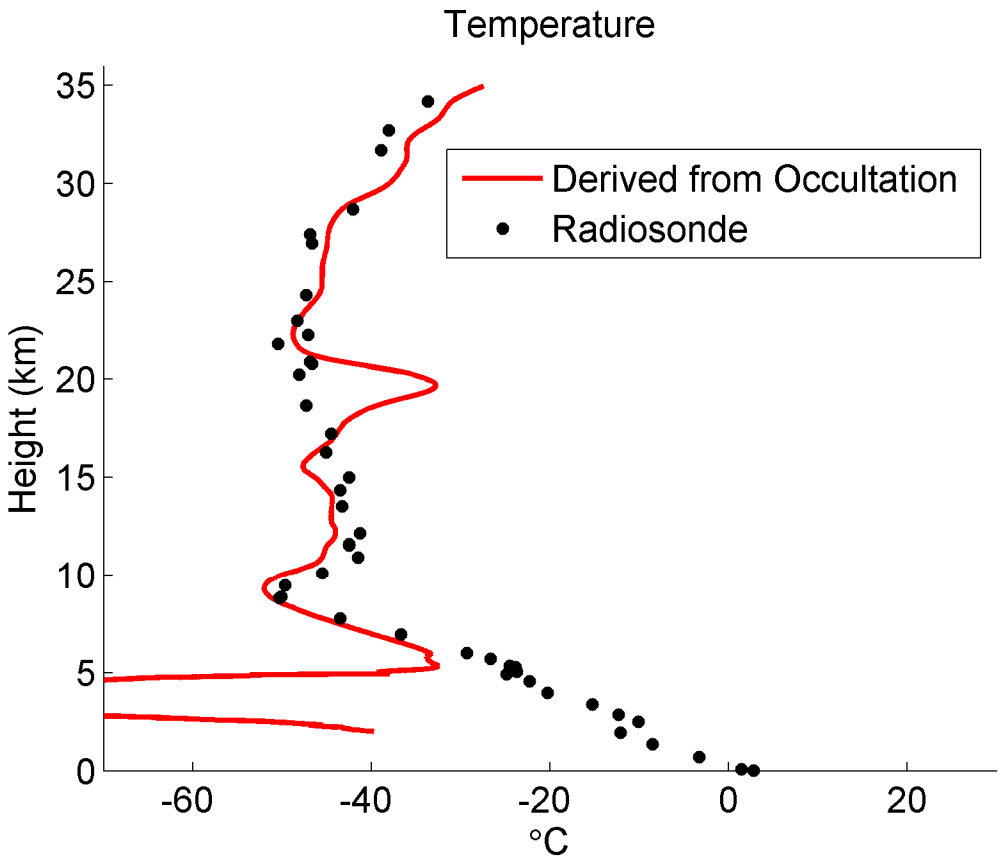

Figure 4.3: Temperature profile with errors resulting from L2 bending angle errors (Event 3 of Table 4.1)

It is possible to avoid this problem by adjusting the height below which L2 data is no longer used to compute the IF bending angle. Figure 4.4 shows the bending angles for this event if the height threshold below which L2 is not used is raised from 12.5 km to 22.5 km. The spike in L2 now has no effect on the IF bending angle, as it is never used in the computation. The IF bending angle at this altitude is based on the L1 bending angle, with a component extrapolated from the trend in L2 between 35 km and 25 km. The corresponding temperature profile is shown in Figure 4.5.

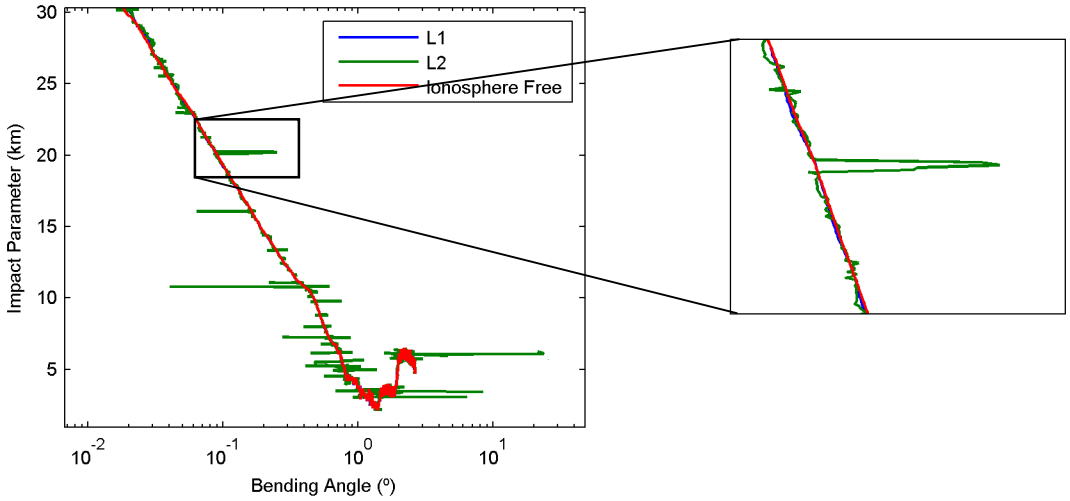

Figure 4.4: Bending angle profiles for Event 3 of Table 4.1 with L2 replacement threshold is raised to 22.5 km

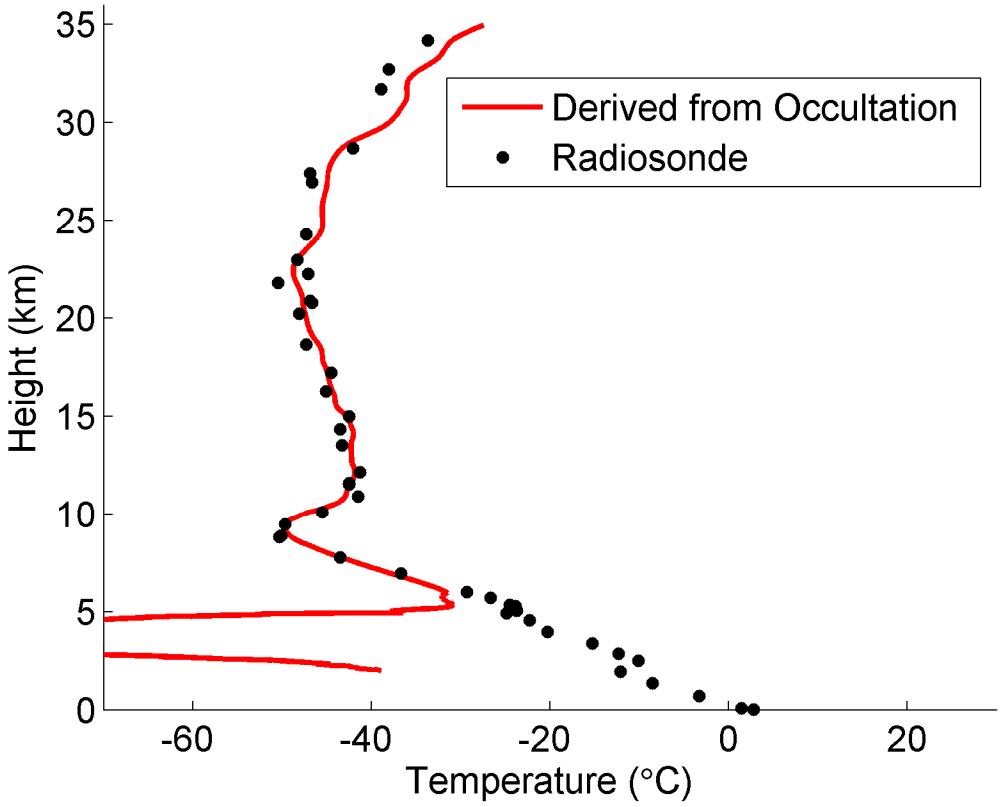

Figure 4.5: Temperature profile for Event 3 of Table 4.1 with L2 replacement threshold is raised to 22.5 km

The derived temperature profile no longer has the large errors around 20 km seen in the first profile. However, while it is possible to correct the gross errors in this case, the accuracy of the IF bending angles is unavoidably degraded by discarding the L2 data between 12.5 km and 22.5 km. This results in a corresponding loss of accuracy in the derived temperatures. Figure 4.6 shows temperature profiles and associated errors for L2 replacement thresholds of both 12.5 km and 22.5 km for Event 1, which does not suffer from L2 signal tracking problems above 12.5 km. There is an increase in mean error from 0.0 to 0.3 ºC, and an increase in RMS error from 0.4 to 0.8 ºC. Note that the error profiles differ only below 22.5 km, as above this height the IF bending angle is calculated using equation 3.18 in both cases.

A full examination of the refractivity (and thus, temperature) accuracy resulting from varying L2 replacement thresholds is beyond the scope of this work. As it is clear that adjusting the replacement threshold will have some effect, all events which would require a higher threshold for successful retrieval are rejected from further tests in order to avoid influencing statistics computed from the data set.

The second common problem in occultation data is a sharp degradation in accuracy at low altitudes (~0 km - 5 km). This is caused by several effects, including lens effects caused by complicated atmospheric structures, multipath caused by refraction or ground reflections, cycle slips, and loss of lock (Ware et al, 1996). A good example of this

(a)

(b)

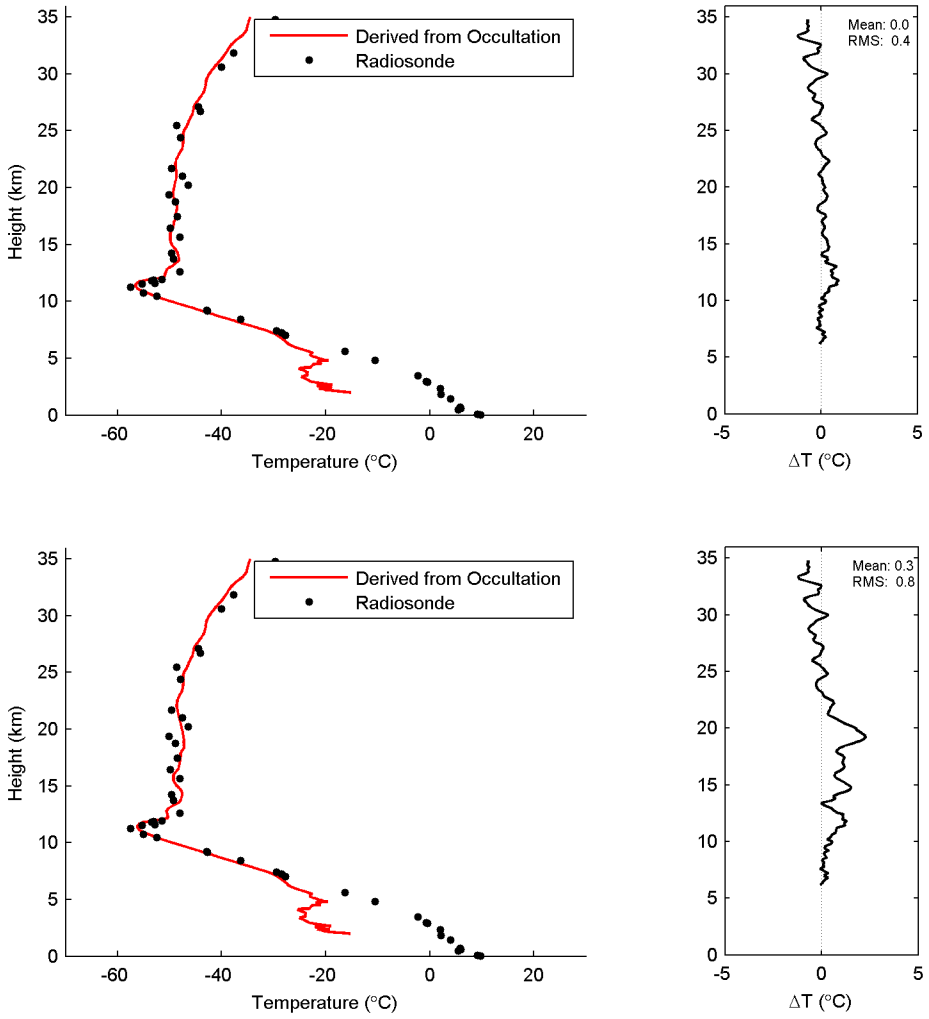

Figure 4.6: Temperature profiles and errors for an L2 replacement threshold of (a) 12.5 km and (b) 22.5 km (Event 1 of Table 4.1)

problem can be seen in the first of the events discussed in this section (see Figure 4.3), in the sharp downward spike in temperature at 6 km. This degradation occurs in all events to some extent, in most cases confined to heights below 5 km.

Derived dry temperatures will also tend to be biased cold at low altitudes in comparison to radiosonde, as a result of neglecting the contribution of water vapour below the tropopause. As the profile extends lower, the amount of water vapour increases, and so does the bias. Figure 4.6 shows an example in which the dry temperature profile begins to deviate strongly from the radiosonde around 5-6 km. This divergence is a real effect and is not considered to be an error (though it may overlap with the low altitude effects in some retrievals), however it is not appropriate to assess the accuracy of the dry temperatures at these heights when they are known to be biased for this reason.

To prevent both the dry temperature bias and low altitude refraction effects from affecting the results, all statistics given for dry temperatures in this work are computed down to a minimum height of 6 km. In some events, these low altitude problems begin to affect the profile even above 6 km; these events are rejected from future tests.

A total of 16 of the 55 events in Table 4.1 experience one or both of these two problems, and are not used in later tests. The remaining 39 events which do not suffer from L2 tracking problems above 12.5 km, and lower altitude effects above 6 km, are referred to as ‘retrievable events’ in later sections.

4.4. Sensitivity of temperature profiles to GPS measurement errors

The limiting factor of the accuracy of the atmospheric excess phase in most cases will be orbital error. GPS clock corrections are available with accuracies better than 3 cm, or can be completely removed by double differencing at the cost of introducing troposphere corrections which are accurate to 4 mm (refer to section 2.3.4). Carrier phase noise is typically at the level of 1-2 mm (Lachapelle, 2004). Precise GPS orbits offer accuracies on the level of 5 cm or better, with comparable accuracy attainable for the LEO orbits. Svehla and Rotacher (2005) give LEO orbit accuracies at the level of 2-3 cm. The CHAMP orbit product is given as being accurate to ~7 cm in 2003 (Wickert et al, 2003), and has improved to ~4 cm by 2005 as a result of improvements in the gravity field model being used (Konig et al, 2005). Pre-mission accuracy requirements for the CHAMP orbits and expected errors for the retrieved vertical temperature profiles are shown in Table 4.2.

Table 4.2: Accuracy requirements for CHAMP orbits (after König et al, 2002)

	Σ Position (cm)	σ Velocity (mm/s)	σ Temperature (ºK)		
			At 0 km Altitude	At 10 km Altitude	At 20 km Altitude
LEO	25	0.15	0.05	0.08	0.10
GPS	10	0.03			

As all residual error sources (GPS orbit and clock, LEO orbit) will be present in the excess phase observable, it is not possible to examine them independently using real data.

Instead, the impact of a given total magnitude of orbital error is assessed empirically by adding error to the input atmospheric Doppler phase measurements and observing the effect on the retrieved temperature profile. As the primary observable in the retrieval process is atmospheric Doppler, it is the rate of change of orbital error rather than absolute error which is of primary interest. This total error represents the combined effect of GPS and LEO orbital error.

Orbital errors tend to be strongly correlated in time (Olynik, 2002). They can be thought of as a slowly-varying difference between the estimated orbit and the true orbit, rather than a random noise sequence deviating from the true orbit. Therefore, the impact of residual errors is assessed by adding a small orbital bias into the measurements, and then observing the resulting perturbation in the temperature profile. This bias is added to the atmospheric Doppler rather than directly to the excess phase, as any constant bias term on the phase would be removed by time differencing and would not affect the Doppler. Thus, this represents a situation where the estimated orbit does not deviate from the true orbit by a constant amount, but rather drifts with respect to the true orbit at a constant rate.

Constant biases with values of 0.05, 0.10, 0.15, 0.20, and 0.25 mm/s were added to the atmospheric Doppler. These values were selected to provide the same order of magnitude of error as required for the CHAMP mission (see Table 4.2). Each set of biased Doppler measurements was then used to derive a temperature profile using the methods described

in Chapter 3. The derived temperature profiles were differenced against a reference profile computed with no bias in the Doppler measurements. The boundary condition applied to generate the temperature profiles was taken from the reference profile at 35 km. The reference profile was derived with a boundary condition from the MSISE functional model at 50 km. The use of the MSISE model as a sole boundary condition source is based on a method employed by Steiner et al (1999), in which temperatures from the MSISE model at 110 km are used to apply the boundary condition. Plots of the resulting temperature error at 10 km and 20 km (for comparison to Table 4.2) from 39 events are shown in Figure 4.7. Data within 200 m of the indicated elevation are included. The median error is indicated by the horizontal red line, blue boxes indicate the upper and lower quartiles of the data, the whiskers indicate the furthest data point falling within 1.5 inter-quartile ranges, and red crosses indicate outlying data points.

In general, the trend is for increased median error as well as an increase in the spread of the error at higher bias levels, as would be expected. However, there are a large amount of outliers. These can begin to have a significant impact on the statistics, as is seen particularly at 10 km in the 0.15 and 0.2 mm/s bias cases, and at 20 km in the 0.25 mm/s bias case. The majority of outliers belong to one or more outlying profiles, in which the entire profile is significantly in error, rather than outliers being evenly distributed across all profiles. An example of an outlying profile resulting from these small biases is shown in Figure 4.8. This is Event 11 from Table 4.1, with a 0.2 mm/s bias applied to the Doppler.

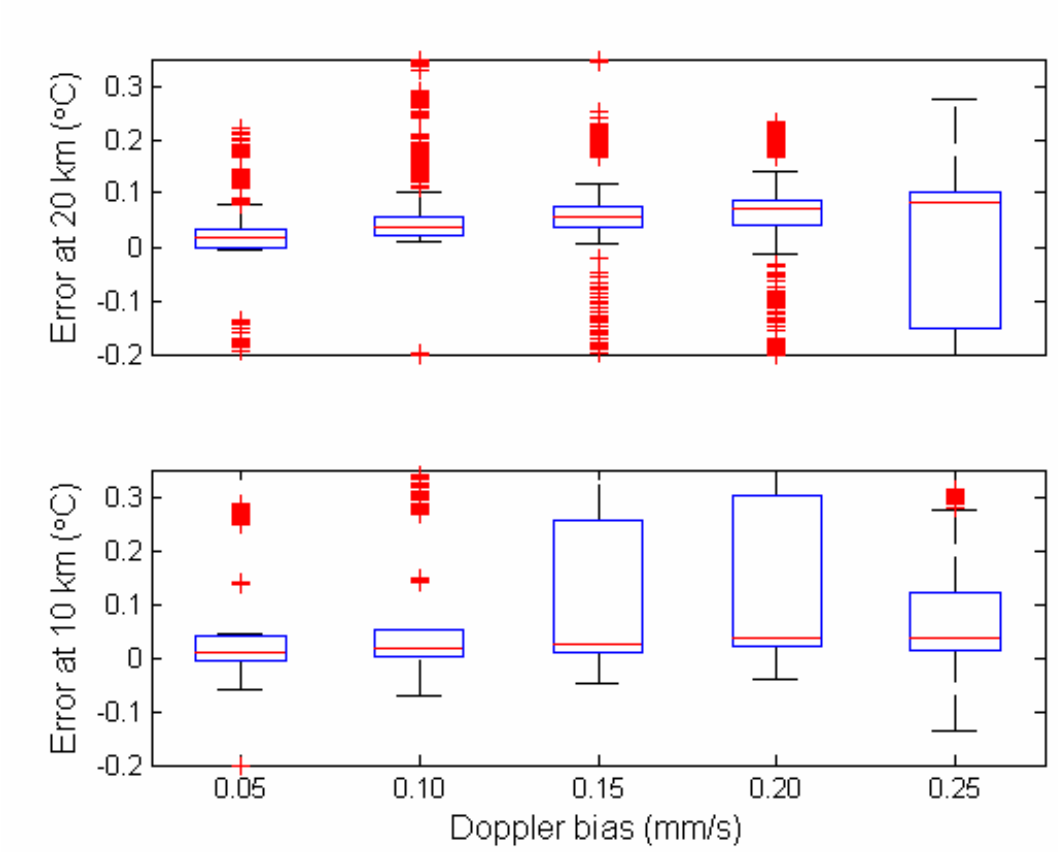

Figure 4.7: Temperature error resulting from biased atmospheric Doppler at 10 and 20 km altitude.

As the temperature profile is computed from a differential equation stepping downward through the refractivity profile, errors at a given altitude will affect the result at all subsequent heights. For some events, as in this case, the errors can add constructively and result in a significantly erroneous profile.

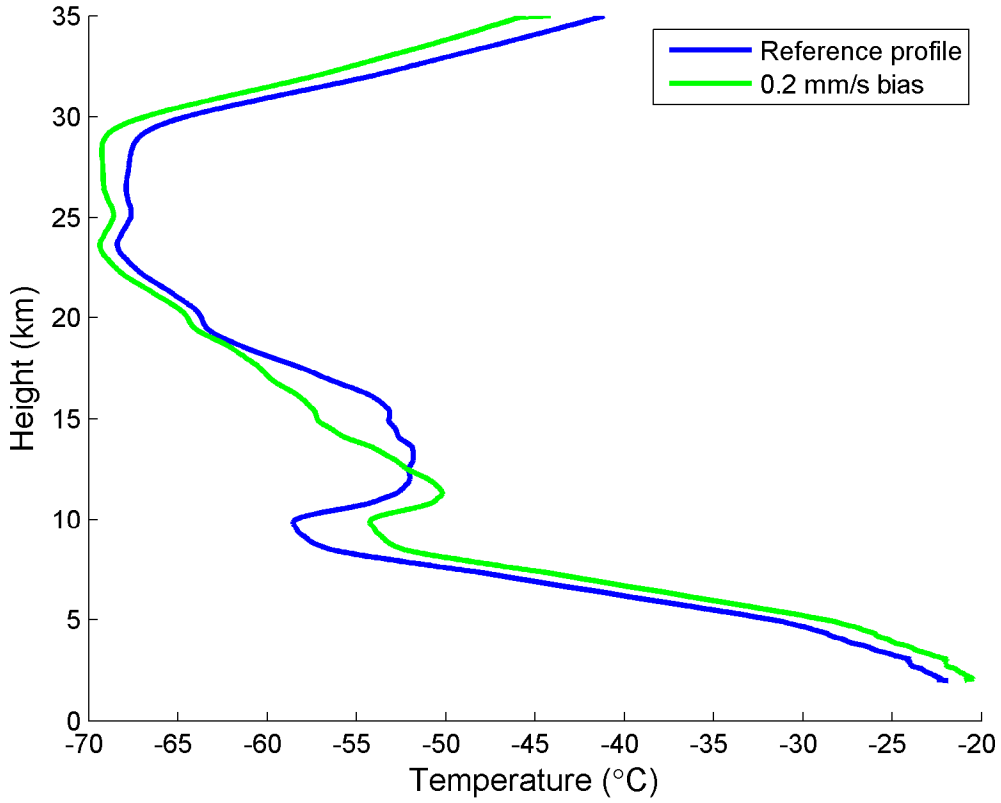

Figure 4.8: Large error resulting from 0.2 mm/s bias on the Doppler observable (Event 11 in Table 4.1).

Median errors for the data shown in Figure 4.7, which includes outliers, are at the same order of magnitude as the standard deviations in Table 4.2 given by Konig et al (2002). Using these standard deviations, all events having a mean error of more than 3σ were rejected from the dataset as outliers. The result is shown in Figure 4.9. The large skewing seen in Figure 4.7 which is caused by the rejected events is no longer present.

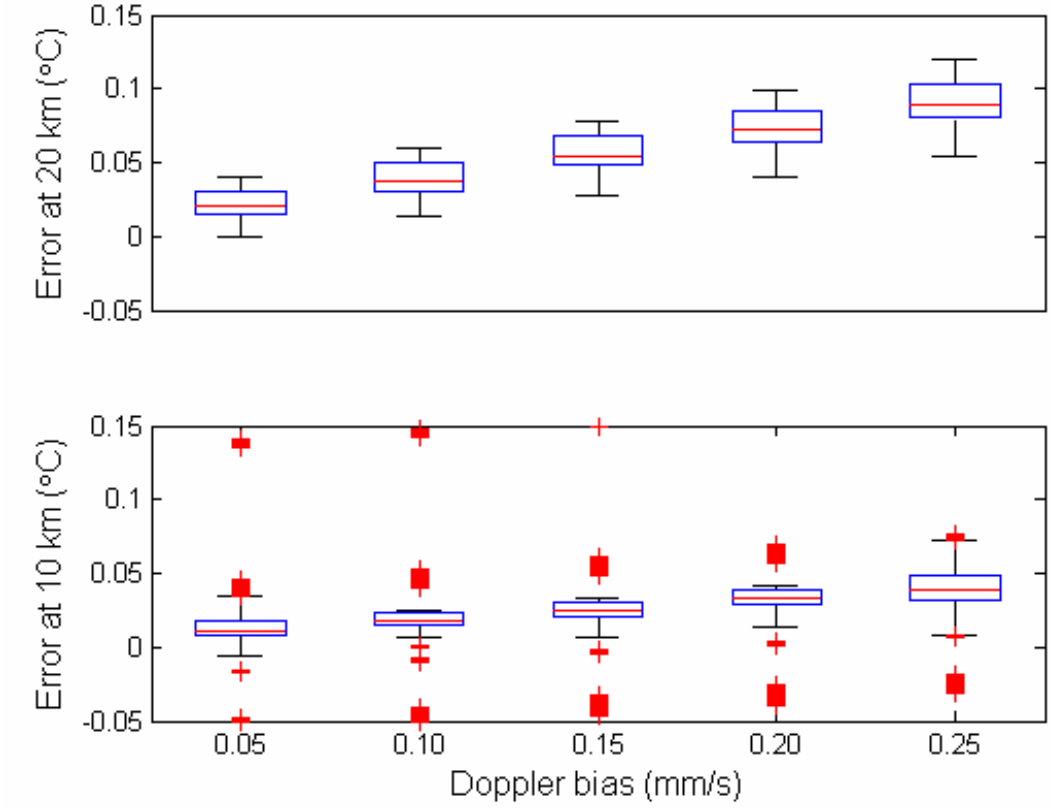

Figure 4.9: Temperature error resulting from biased Doppler at 10 and 20 km altitude with outlying profiles removed

The general trend is for larger temperature error higher in the profile, with a wider range of error at lower altitudes. At 10 km there are still four events which are classed as outliers based on the spread of these reduced data, and appear as such in the box and whisker plot, but these are not outliers based on the estimated standard deviations. The magnitude of the errors loosely agrees with the values given by Konig et al (2002). The expected errors from 0.15 mm/s GPS orbit error and 0.03 mm/s LEO orbit error are 0.10 ºC at 20 km, and 0.08 ºC at 10 km. The observed mean errors introduced from 0.2 mm/s of additional Doppler error are 0.09 ºC and 0.045 ºC respectively.

Perhaps more significant than the magnitude of the resulting temperature error is the number of outlying events which were rejected. In total, 24 events were classified as having an outlier for at least one height range for at least one value of the five bias levels tested, representing 62% of the profiles examined. If outlier detection is performed only for a single bias level, the number of rejected events ranges from 14 at 0.05 mm/s to 16 at 0.25 mm/s (36-41%). Therefore, while the majority of events support the expected error levels of Konig et al (2002), there is an increased need for outlier detection and rejection as the orbital error increases. If outliers are not rejected, the range of resulting temperature error rises dramatically, and there is the risk that clearly erroneous results like those in Figure 4.8 would be generated.

4.5. Sensitivity of temperature profiles to errors in boundary condition

The sensitivity of the temperature profiles retrieved from RO to errors in the boundary condition was tested by adding deliberate errors (biases) to the boundary condition used to compute the temperature profile. The temperature profile computed using a biased boundary condition is compared against a reference profile generated using an unbiased boundary condition. The unbiased boundary condition for these analyses is taken from the GFZ temperature profile product for the corresponding event, applied at a height of 35 km. Biases applied range from -5 ºC to 5 ºC. These bias values are reasonable for the temperature error observed in actual NWP data, as seen in the next chapter in Figure 5.1.

Selected error profiles for one event (Event 1 in Table 4.1) are shown in Figure 4.10. Displayed is error as a function of height for profiles initialized with a -5 ºC, -2 ºC, 2 ºC, and 5 ºC bias in the boundary condition.

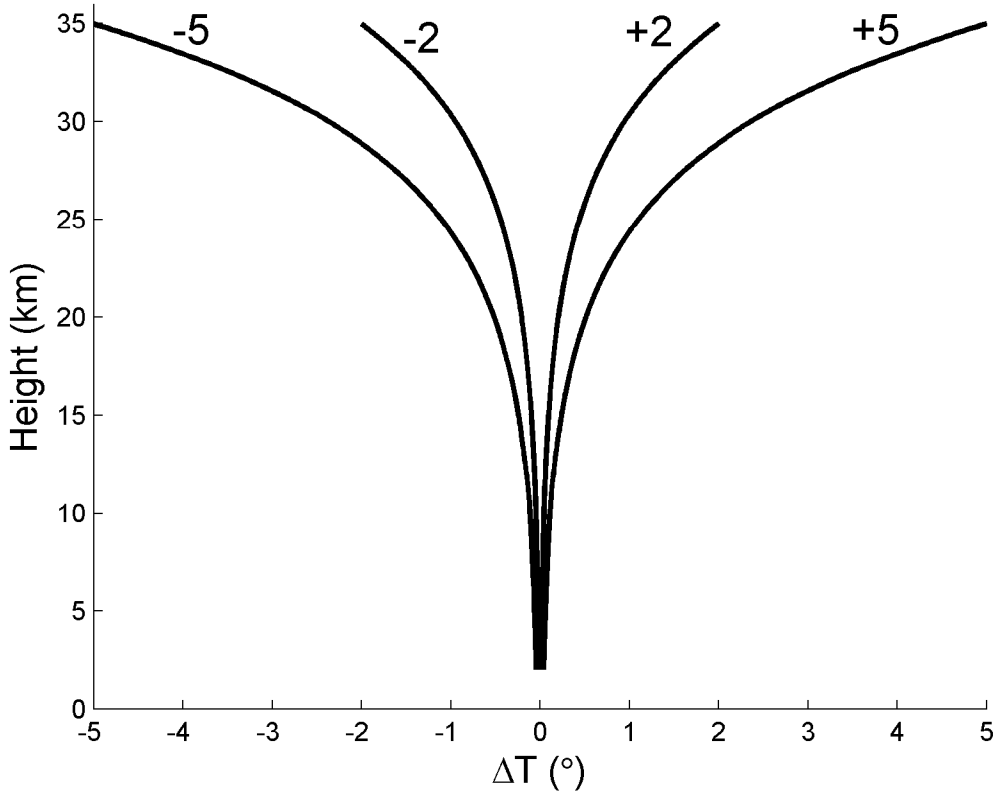

Figure 4.10: Temperature error resulting from biased boundary condition (Event 1 of Table 4.1)

The resulting error is symmetric with respect to the sign of the bias, with biases of equal magnitude producing temperature errors of equal magnitude. The majority of the error occurs at the top of the profile, with all profiles reaching a comparable level of accuracy after a suitable convergence time. As could be expected, greater biases require convergence over a greater height range before reaching the same level of accuracy. This

would suggest that problems arising from the use of inaccurate or uncertain boundary conditions can be somewhat overcome by initializing the profile at a much greater height than the heights at which the temperature data are to be used. Figure 4.11 shows the temperature error as a function of distance from the height at which the boundary condition was applied. The unbiased temperature profile for this event is shown in Figure 4.12.

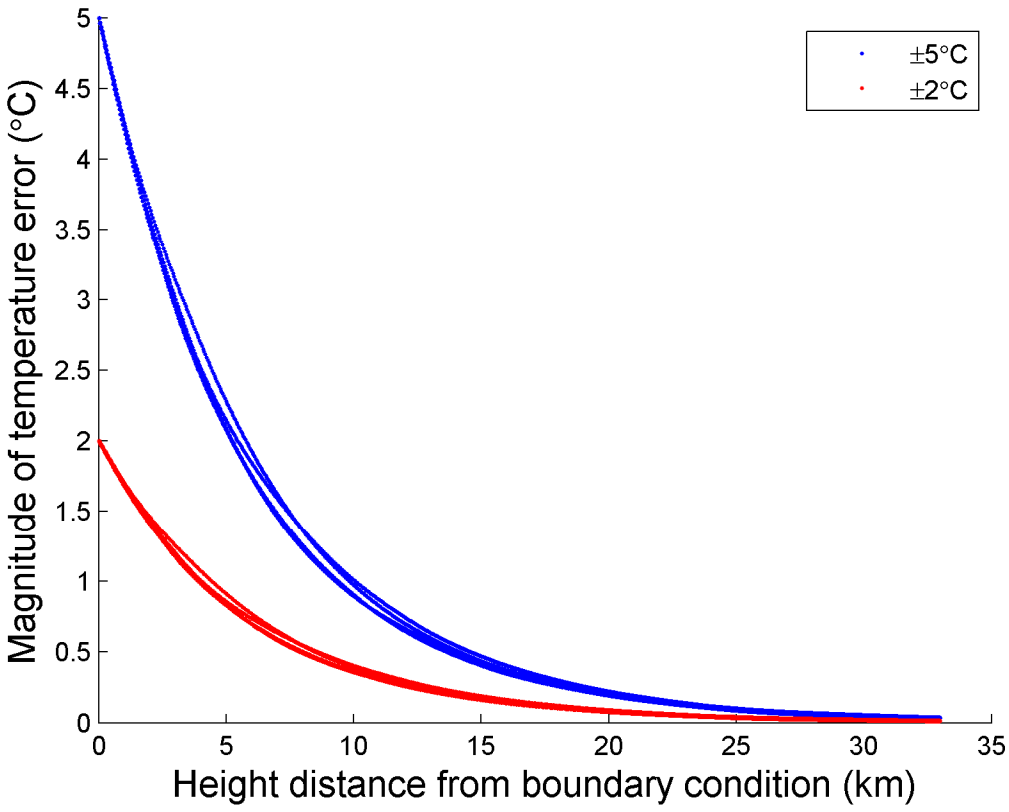

Figure 4.11: Temperature error as a function of distance in height from boundary condition

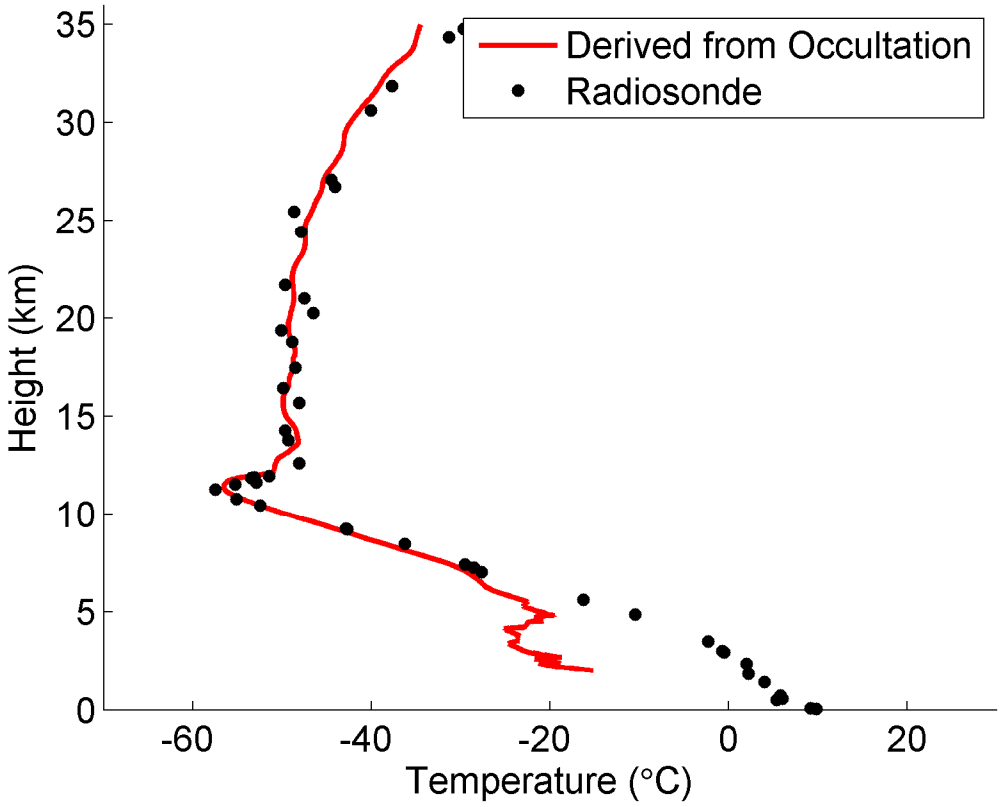

Figure 4.12: Reference profile bounded by unbiased GFZ temperature product (Event 1 of Table 4.1)

Seasonal differences in the impact of the boundary condition bias were also investigated, using the initial 18 events' data which were distributed equally between summer and winter. Biases of equivalent magnitude were introduced into boundary conditions taken from the GFZ temperature product for both summer and winter events. A bias of a fixed value will be a larger relative error for a winter event, as the temperature at the height at which the boundary condition is applied is typically lower. This difference in relative bias has no effect on the resulting temperature errors for the bias magnitudes examined. This is demonstrated in Figure 4.13, which shows selected error profiles for summer and

winter events (Events 1 and 5 in Table 4.1, respectively). Negative biases are shown for summer and positive biases for winter for display purposes only; both positive and negative biases give consistent results between seasons.

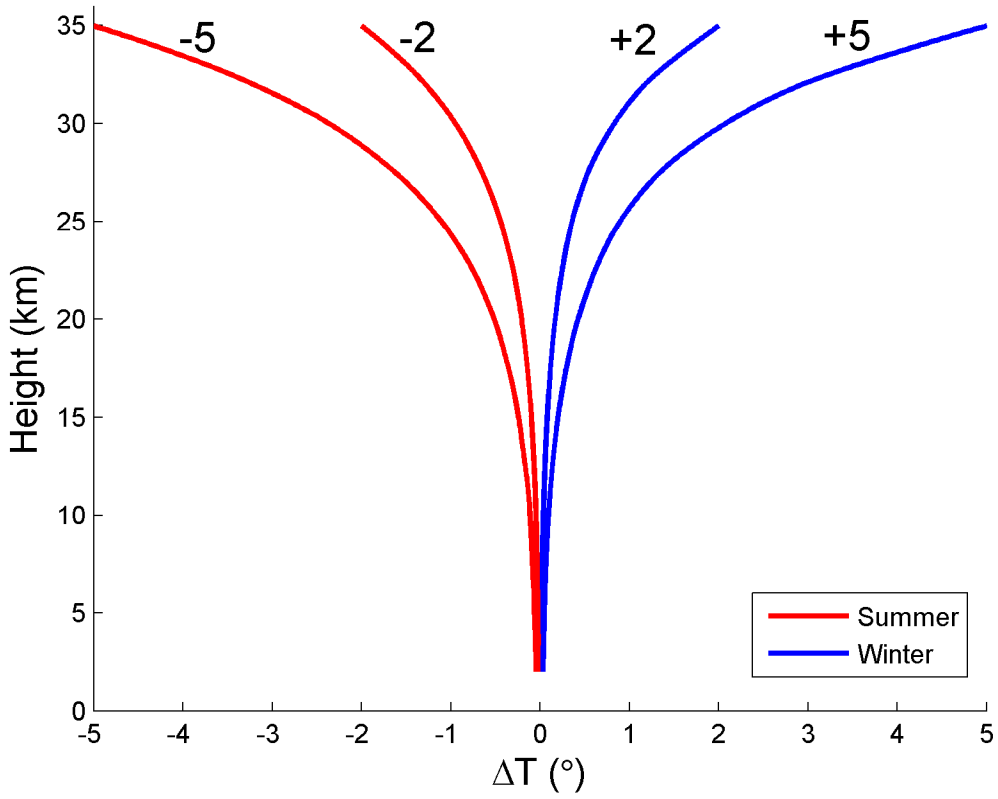

Figure 4.13: Temperature errors for a summer and winter event (Events 1 and 5 in Table 4.1)

Figure 4.14 shows a summary of the total error RMS of the temperature profiles resulting from biased boundary conditions across all retrievable events in the initial 18 event data set. Statistics are computed from data down to only 6 km to prevent errors caused by

poor raw data quality from having an impact on the result. The relationship of resulting error to bias is linear, symmetric, and seasonal differences are insignificant.

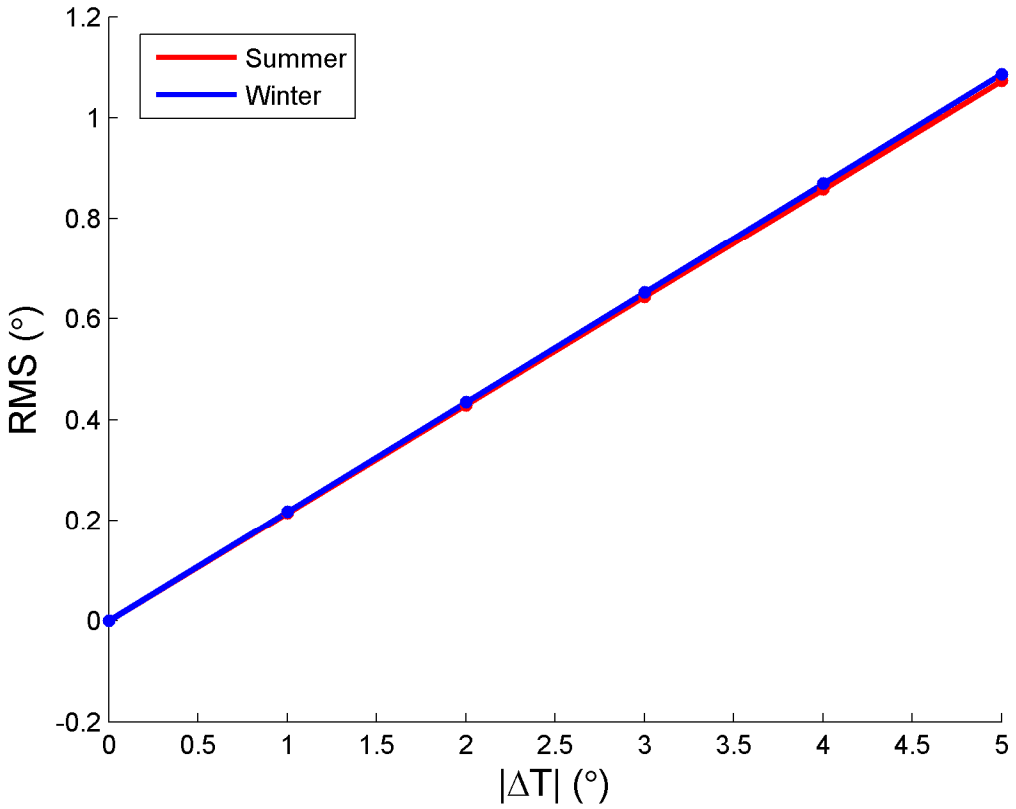

Figure 4.14: Summary of temperature errors (RMS) resulting from biased boundary conditions (ΔT)

4.6. Sensitivity of humidity retrievals to errors in refractivity and external temperature profiles

As is seen in Chapter 3, partial water vapour pressure, e, is solved using two inputs: refractivity, N, and temperature, T. Pressure, P, is solved simultaneously with e. These terms are related according to equation 3.23. This equation rearranged to solve for e is:

$$e = \frac{T^2}{3.73 \times 10^5}\left(N - 77.6\frac{P}{T}\right) \tag{4.1}$$

Refractivity is derived from the radio occultation data as described in Chapter 3, and temperature is typically supplied by a numerical weather prediction model. Both of these quantities will contain errors which will affect the humidity estimates.

The partial derivatives of equation 4.1 with respect to temperature and refractivity are as follows:

$$\frac{\partial e}{\partial T} = \frac{2NT}{3.73 \times 10^5} - \frac{77.6P}{3.73 \times 10^5} \tag{4.2}$$

$$\frac{\partial e}{\partial N} = \frac{T^2}{3.73 \times 10^5} \tag{4.3}$$

As both relationships are a function of temperature, the temperature value for a given profile will affect the degree to which temperature and refractivity errors will propagate into the water vapour solution. To assess the likely range of the derivatives that can be expected from these data (and for Canadian weather in general), the partial derivatives for the coldest and warmest events in the dataset were computed. All other events will fall within the range defined by these two curves, as should the majority of Canadian retrievals. The results are shown in Figure 4.15.

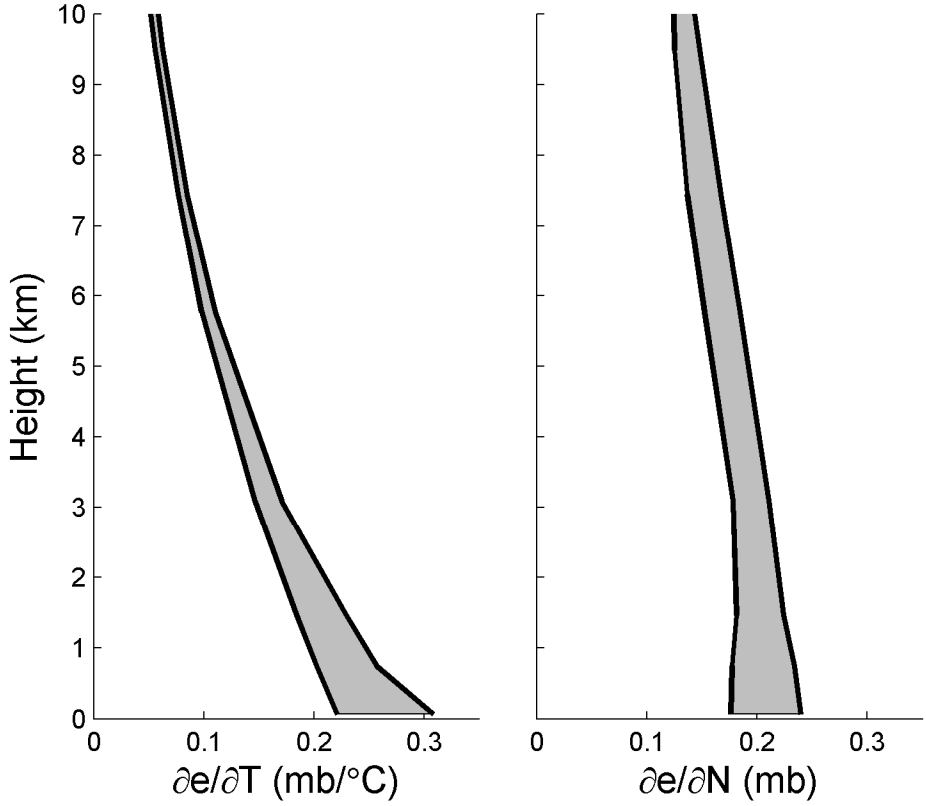

Figure 4.15: Partial derivatives of water vapour pressure to temperature and refractivity across the data set

The partial derivative with respect to temperature increases in an exponential fashion with decreasing height, as it is a function of the pressure (which is solved simultaneously with the water vapour pressure). The partial derivative with respect to refractivity varies more linearly, as it is a function of temperature only. For unit error, the magnitudes of the partial derivatives are comparable, but we cannot assume that the input temperature and refractivity will have equivalent error magnitudes. To properly assess the likely

impact of temperature and refractivity errors, the typical level of error for each quantity is required.

To obtain an estimate of the typical level of error in the temperature, the difference between radiosonde measurements and the GEM model (the NWP product used in this work, discussed in Section 5.1) was computed. Figure 4.16 shows the temperature differences between GEM and radiosonde for all events. Differences are only computed below 15 km, as that encompasses the region in which humidity is non-negative. The mean error is -0.01 ºC, with a standard deviation of 2.0 ºC

To estimate the refractivity error, the difference was similarly computed between the occultation derived refractivity profiles and refractivity profiles computed from radiosonde measurements. Differences are only computed above 6 km to avoid low altitude effects. The accuracy of the radiosonde measurements can not be precisely identified, as the exact model of the radionsondes used for these events is not known. For reference, however, the accuracy of the Vaisala RS-80 radiosonde is given by the manufacturer as better than 3% in relative humidity, 0.2 ºC in temperature, and 0.5 hPa in pressure (Niell et al, 2001). This is well below the level of variation between GEM and radiosonde seen above, suggesting that the difference stems mainly from error in the GEM values.

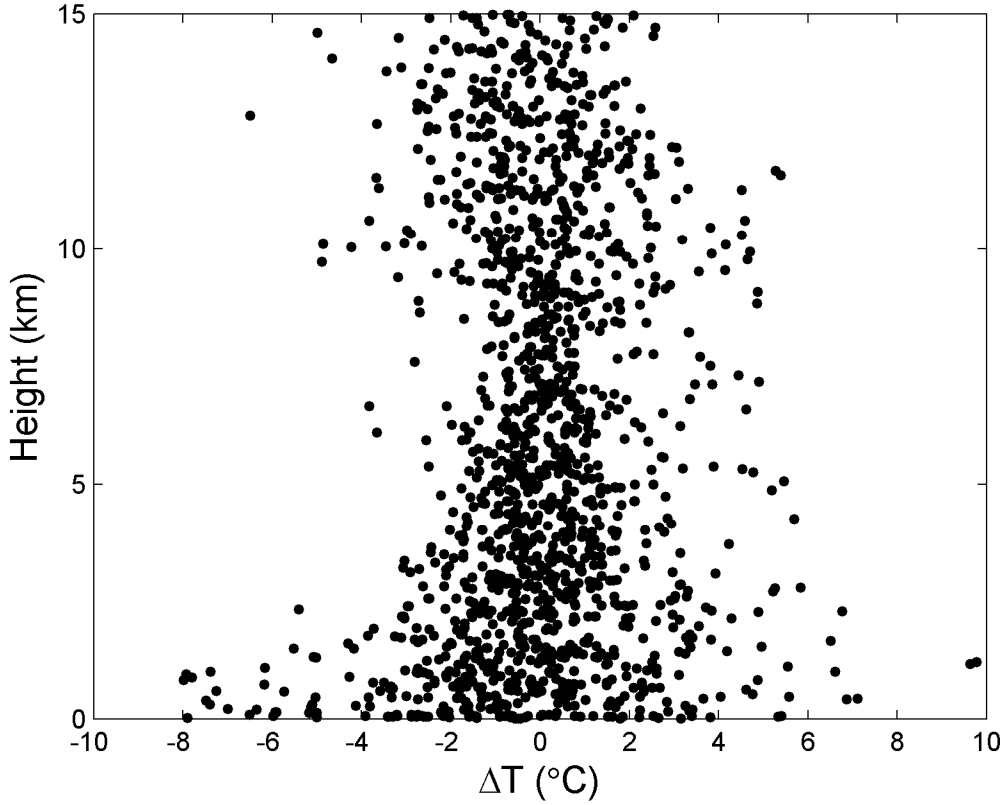

Figure 4.16: Temperature difference between GEM and radiosonde

The absolute error displays a clear exponential trend. If relative error is computed instead, the results are more consistent. Figure 4.17 shows the absolute and relative refractivity errors vs radiosonde for all retrievable events. Data is shown up to 30 km to highlight the difference in shape between the two error distributions. Mean relative error in refractivity below 15 km is 0%, with a standard deviation of 1.2%.

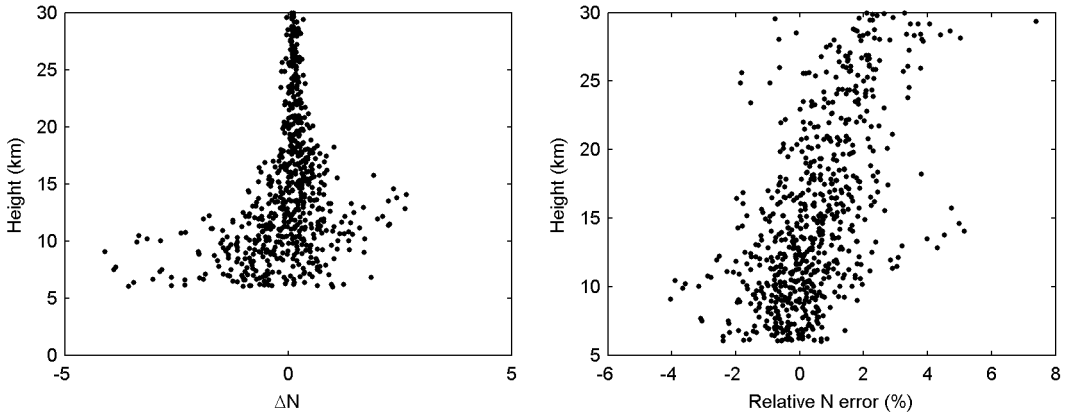

(a) (b)

Figure 4.17: Absolute (a) and relative (b) refractivity difference between occultation and radiosonde

The expected levels of water vapour pressure error resulting from one standard deviation of temperature and refractivity error can now be computed. These are displayed in Figure 4.18, again for the range between the coldest and warmest events.

From this figure it is apparent that the error contribution to humidity retrievals from the refractivity error will be roughly 50-60% more than that from temperature error. This is true only for the accuracies of the input quantities observed in this work.

When the magnitude of the error in water vapour pressure gets too large, a mathematical effect can occur which results in entirely unrealistic estimations of the water vapour pressure. Physically, water vapour pressure is a non-negative quantity. However, it is possible for a negative value to emerge in equation 4.1 when the right half of the term in

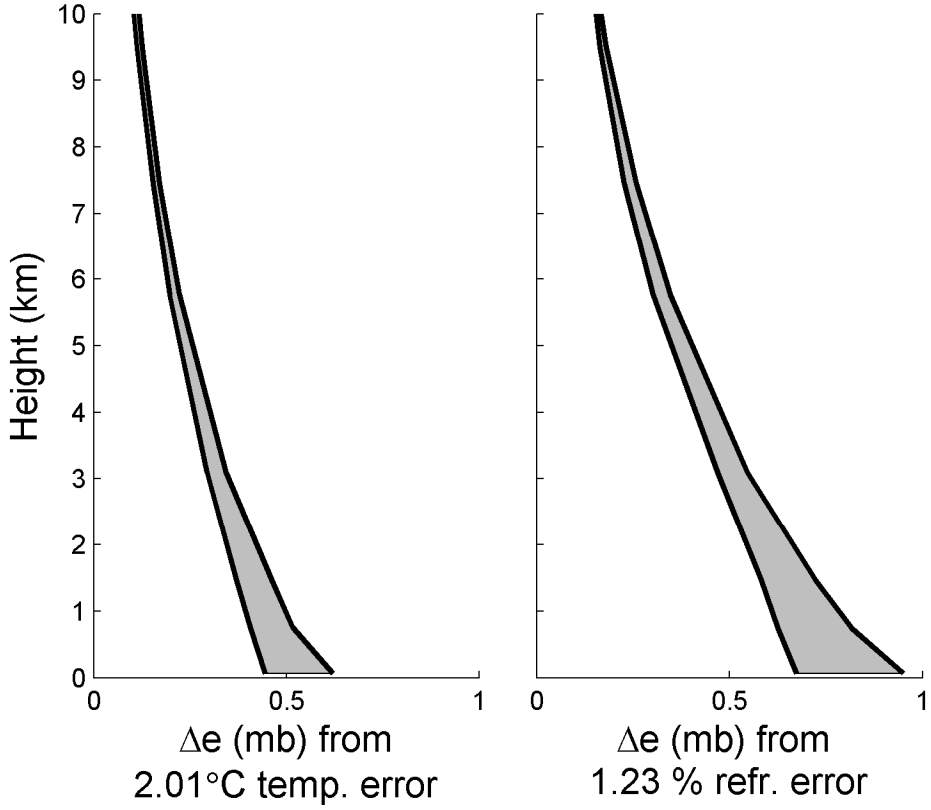

Figure 4.18: Water vapour pressure error resulting from typical refractivity and temperature error

brackets is greater than the refractivity value, giving a negative result. The term in brackets represents the level of the total refractivity contributed by the water vapour pressure. A negative value can occur when the combined magnitude of the errors exceeds the true value of this component of the refractivity. This occurs most commonly at altitudes approaching and above the tropopause, when the water vapour pressure is lowest. Forcing the estimated water vapour pressure to a non-negative value does not significantly improve the result, as the error effect which caused the negative value

typically also affects the neighbouring water vapour values, even though they may evaluate to non-negative values. This is demonstrated in more detail in Chapter 5.

To quantify this, expected water vapour pressure error was computed relative to the actual value of water vapour pressure at each height. This was done for both the wettest and driest events in the dataset, again to capture the range of likely values across the data. Figure 4.19 shows the water vapour pressure profiles for the wettest and driest events in the data set. The profile of mean water vapour pressure from GEM at each height is shown for comparison.

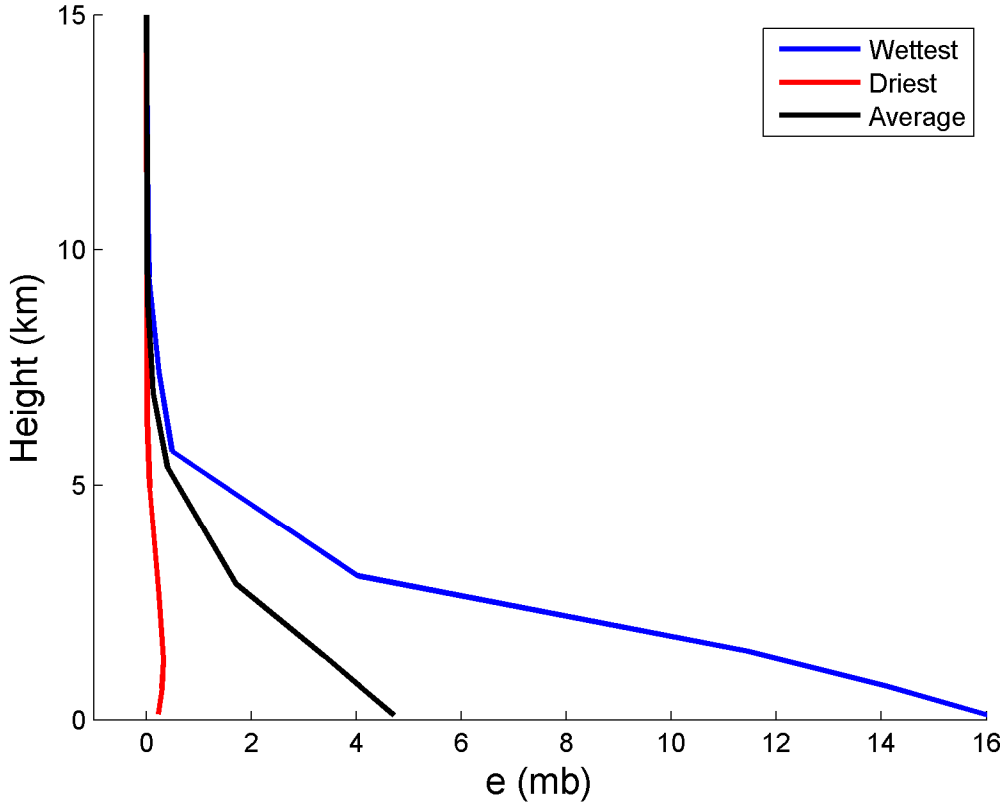

Figure 4.19: Water vapour pressure for wettest, driest, and an arithmetic average event (values from a Numerical Weather Prediction Model – GEM)

The expected water vapour error is here defined as the sum of squares of the errors resulting from temperature and refractivity at each height, as displayed in Figure 4.17. A variance sum is used as the expected errors are the standard deviations of the differences in temperature and refractivity observed, as described above.

$$\Delta e(h) = \sqrt{\Delta e_{temperature}(h)^2 + \Delta e_{refractivity}(h)^2} \tag{4.4}$$

The temperature and refractivity error contributions from the warmest profile in the dataset were used, as they represent a worst case (the derivatives increase with temperature). The results are shown in Figure 4.20.

From a computational standpoint, of primary importance in this figure is the point at which the error exceeds 100% of the true value. Around and above this height the likelihood of negative numbers resulting from equation 4.1 becomes very high. This occurs at all heights for the driest event because the magnitude of the true water vapour pressure is extremely low. This is an issue for humidity retrievals in the dry Canadian Arctic conditions especially.

Beyond the computational considerations in identifying the point of 100% relative error, there are considerations for the accuracy of the derived water vapour at lower heights. For the driest event in this data, the likelihood of retrieving any useful water vapour data

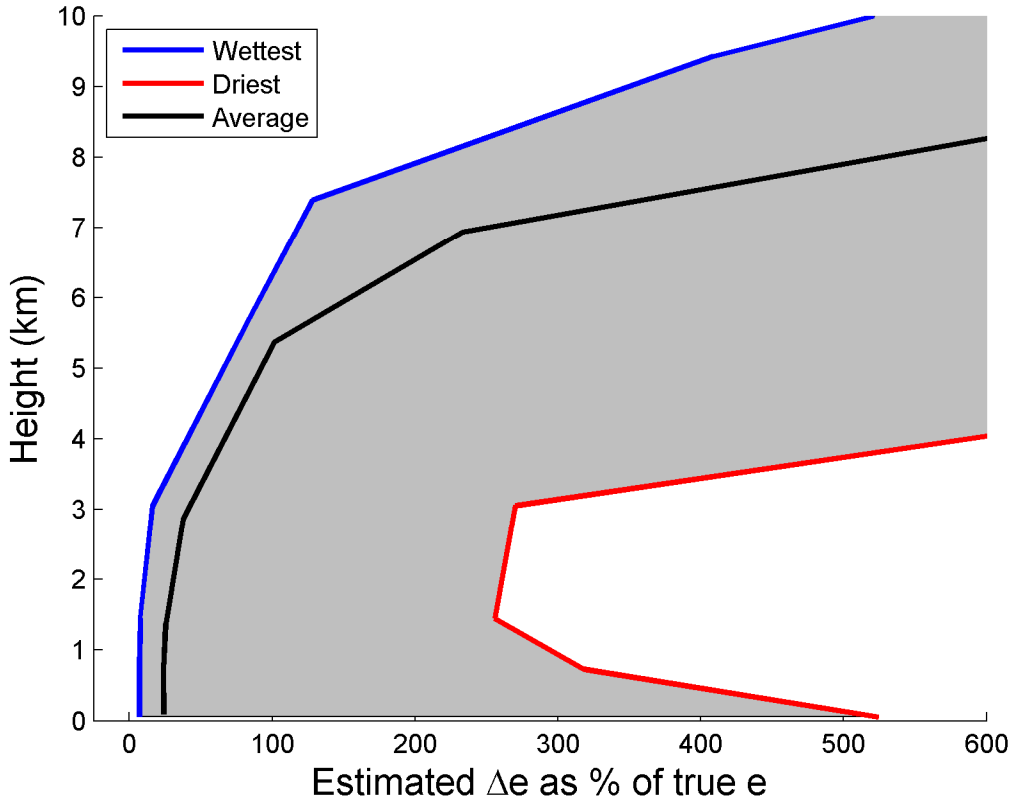

Figure 4.20: Expected water vapour pressure error relative to the true vapour pressure for the warmest profile in the data set

at all is minimal, given the level of error in the input temperatures and refractivities. In the wettest case, the expected relative error remains below 50% up to 3 km, but increases rapidly at higher altitudes (where the true vapour pressure becomes less). It is worth repeating that the absolute error remains the same. It should be noted as well that the results in Figures 4.18 and 4.20 are for one standard deviation of observed error; the mean errors are much lower.

4.7. Accuracy requirements for NWP products

The results for temperature error as a function of residual GPS errors derived in section 4.3 support the values given by Konig et al (2002) on which the CHAMP orbit accuracy requirements are based. As the CHAMP orbits are accurate to between 4 and 7 cm – within the accuracy targets in table 4.2 – we can expect that the temperature profile error resulting from the residual orbital error will not exceed the 0.10 ºC predicted by Konig et al (2002). As the expected accuracy of an occultation retrieval is on the order of 1-2 ºC (eg. Hajj et al, 2002), orbital errors will not significantly impact the total error budget.

It is not practical to fully isolate and examine all other non-NWP error sources, such as additional residual GPS errors (clock, troposphere products, residual ionospheric effects) and any systematic or computational errors introduced in the bending angle calculations and Abel inversion. If we conservatively assume that two thirds of a 1 ºC error budget is to be taken up by these errors, we are left with an allowable one sigma error of 0.57 ºC arising from error in the boundary condition. From Figure 4.14, we can see that this level of error will be introduced across the whole profile by a boundary condition error of ~2.5 ºC. However, from Figure 4.11 it can be seen that even a 5 ºC boundary condition bias will reach this level of error after 15 km. For boundary conditions applied at 35 km, as is the case in Figures 4.11 and 4.14, this would mean that temperature error from the boundary condition bias would be acceptable at heights from 20 km down. From Figure 4.16 it can be seen that the standard deviation of GEM temperature error with respect to radiosonde is 2 ºC. For a 2 ºC error, overall profile accuracy will be within the 0.57 ºC

budget, and all temperature values should meet the error budget at a distance of 9 km of height below the height at which the boundary condition is applied.

From section 4.5, it can be seen that the observed refractivity error in these data is on the order of 1-2%, one sigma. This is slightly worse than theoretical estimates of the attainable accuracy, which are 1% or less (Kursinski et al, 1997). This refractivity error will yield an absolute error in water vapour pressure as high as 1 mb at the surface. The mean surface vapour pressure in the data set used in this work is 4.5 mb. In order to achieve water vapour estimates with a relative accuracy of 50% or less at the surface, the NWP temperature profile must be accurate to 6.6 ºC, assuming the average level of refractivity error seen in these tests.

For events drier than average, the accuracy requirements of the NWP are correspondingly higher, with some events so dry as to not be realistically retrievable. If we assume the GEM temperatures are accurate to 2 ºC, as seen above, 50% relative accuracy at the surface is attainable for all events with a surface *e* greater than 1.12 mb. Figure 4.21 shows the surface *e* for all events, with a line at 1.12 mb. 50% relative accuracy would not be attainable for 19, or 28% of the events.

To achieve 50% relative accuracy at the surface for the driest event in the data set (0.23 mb) would not be possible with the refractivity errors observed here, and would require

NWP temperatures accurate to 0.4 ºC even if refractivity could be computed without error.

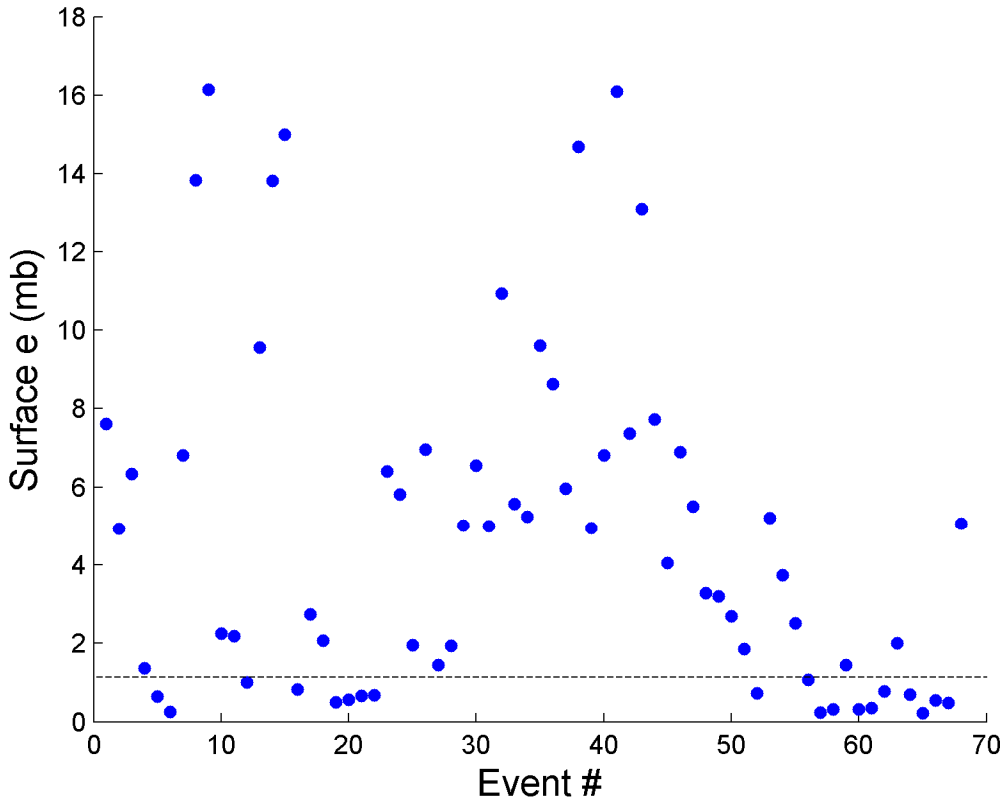

Figure 4.21: Surface *e* for all events

Chapter 5 - Results for NWP Data

While the focus of the previous chapter has been on sensitivity analyses and requirements for the retrieval process and input occultation and temperature data, in this chapter the results of retrievals using actual NWP data are examined. The effect of using different boundary conditions is examined, and the accuracy of the final retrievals is assessed against the CHAMP temperature profiles and radiosonde humidities.

Profiles derived from radio occultation observations using NWP boundary conditions are derived in Section 5.2. Then humidity profiles using input NWP temperatures and occultation derived refractivities are derived and presented in Section 5.3. The NWP used in this work was the Global Environmental Multiscale (GEM) model, developed and run by Environment Canada.

5.1. The GEM model

The GEM model is a NWP model developed by Environment Canada. It is currently used for operational meteorology and forecasting in Canada. Only those aspects of the GEM model relevant to this work are discussed here. A more thorough description of the model can be found in Côté et al (1998).

The GEM model was developed by the Meteorological Research Branch (MRB) and the Canadian Meteorological Centre (CMC), and became operational in 1998. The model

operates on a variable resolution horizontal grid, in order to allow modeling of parameters on a global scale while also offering enhanced resolution in areas of interest.

NWP data used in this work predates the current grid implementation, as a result of constraints on the availability of occultation data. The current public GEM products are described in section 5.4. The grid for the NWP data which are available at the same time as the occultations is a uniform latitude/longitude grid with a spacing of 0.25º (~ 14-28 km). For these data sets only 16 isobaric levels, ranging from 10-1000 mb are available. These levels are listed in Table 5.1. Analysis time NWP data are available for two initialization times each day, at 00h and 12h GMT. At these times, data from external sources is assimilated into the model. A 12 hour forecasted product is also available, having a time of applicability which is the same as the analysis time data, but having been produced from the initialization run 12 hours previous.

Table 5:1: Isobaric levels in GEM data used in this work

Level	Pressure (mb)	Level	Pressure (mb)
1	1000	9	200
2	925	10	150
3	850	11	100
4	700	12	70
5	500	13	50
6	400	14	30
7	300	15	20
8	250	16	10

5.2. Performance of GEM as a boundary condition source

To assess the performance of the GEM model as a source for the boundary condition required to obtain temperature profiles from radio occultation observations, temperature profiles were generated using GEM boundary conditions and the results were compared to the CHAMP temperature product for the corresponding event. The CHAMP product is used as it is an external comparison, and has been verified against ECMWF profiles, with an agreement at the level of 1-2 ºC (see Figure 1.2). In this chapter agreement is shown between GEM bounded profiles and the CHAMP product which is also at a level of 1-2 ºC. This agreement should not be interpreted as though the CHAMP product is an absolute truth, and GEM bounded profiles are thus accurate to 1-2ºC, but rather than GEM bounded profiles perform comparably with the CHAMP product, and are thus a suitable alternative result.

Even though the occultation data used to derive both the temperatures in this work and the CHAMP product is the same, the algorithms used to derive the temperature from the occultation data have been independently implemented, and the ECMWF model was developed and is run independently of the GEM model, so the CHAMP product is considered to be an independent check of the algorithm and boundary condition. The boundary condition for the CHAMP product is a combination of ECMWF and MSISE-90 data (Wickert et al, 2003). As the CHAMP product consists of dry temperatures, comparison against CHAMP also avoids colouring the results with the bias caused by

neglecting water vapour, which would appear if comparison was done to radiosonde or a NWP.

A temperature profile obtained using radiosonde temperature measurements as a boundary condition was compared against the CHAMP product, in order to have a baseline for comparison with which the effects of the algorithm implementation can be distinguished from the effect of using various boundary conditions taken from the GEM model.

GEM boundary conditions were tested for three different cases:

Case 1) Analysis-time GEM boundary conditions, corresponding in space and time to the occultation event. This should be the most accurate boundary condition, and should result in the profile with the least error vs. CHAMP.

Case 2) Analysis-time GEM boundary conditions, corresponding in time to the occultation but interpolated spatially to the location of the radiosonde launch. This boundary condition more closely matches the use of a boundary condition from a radiosonde, and will show the difference between using boundary conditions from GEM vs. radiosonde.

Case 3) 12-hour forecast GEM boundary conditions, corresponding in space and time to the occultation event. This case will show the effect on profile accuracy if forecasted, rather than analysis time, boundary conditions are used.

The inclusion of a 12 hour forecast data case is to simulate a real time or near real time scenario, when occultation data may be available before the corresponding NWP data. In such cases, it will be necessary to use forecast data from an earlier analysis run to produce the occultation profiles. The longest forecast interval will be 12 hours for GEM, as that is the maximum time between analysis runs. Forecast intervals of 3, 6, and 9 hours are also possible with the GEM products, but it is assumed that the accuracy of shorter forecasts will be better than the 12 hour case. Analysis-time data using the radiosonde location rather than the occultation location is done to assess the extent to which differences in accuracy between the radiosonde profile and the GEM profile described in case 1 are due to differences between the products, and to what extent they are due to the geographic separation of the radiosonde from the occultation.

5.2.1. Accuracy of GEM temperatures

Prior to applying boundary conditions obtained from the GEM model, an initial assessment of the accuracy of the GEM model temperatures was performed. GEM temperatures at the location and time of radiosondes were compared against all radiosonde measurements for all events in Table 4.1. The resulting temperature differences as a function of height are shown in Figure 5.1.

The vast majority of GEM temperature values agree with radiosonde values to within 2 ºC, with an overall RMS of the temperature error of 1.7 ºC. Referring to Figure 4.8, it is seen that a 1.7 ºC error will result in approximately 0.4 ºC error in the resulting profile, with the majority of that concentrated near the boundary condition. This is deemed to be within acceptable levels, as the expected accuracy of the radio occultation technique is only on the order of 1-2 ºC (Hajj et al, 2002). Therefore, further testing with GEM boundary conditions is justified.

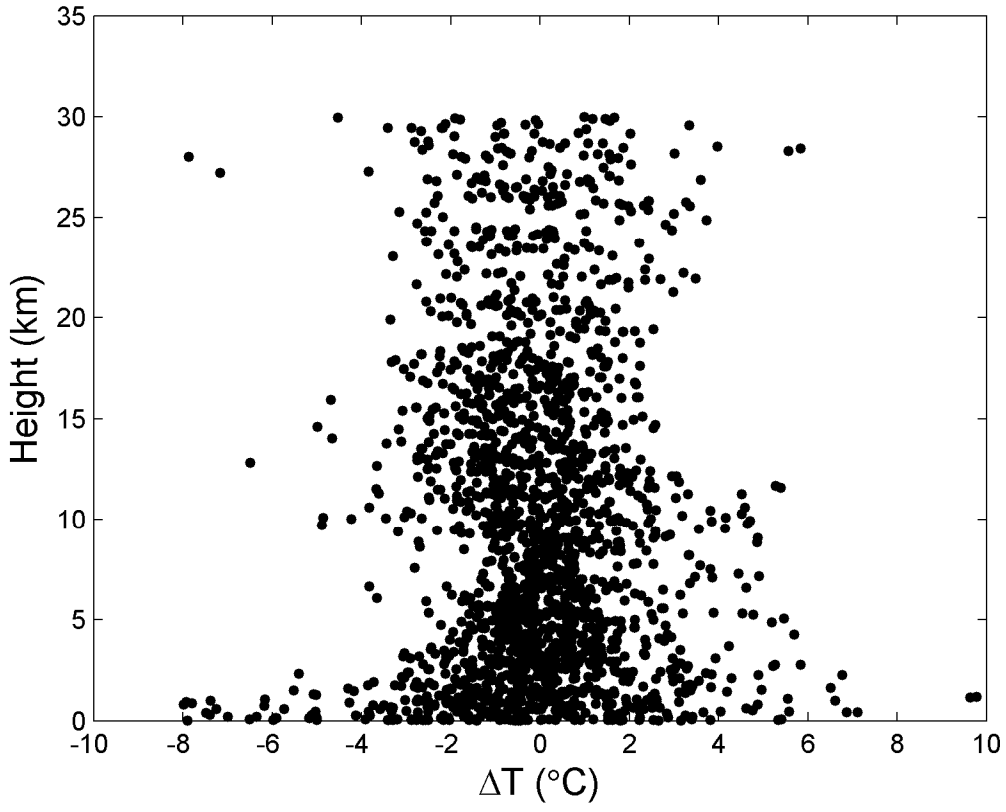

Figure 5.1: Difference between GEM and radiosonde temperatures for all events in Table 4.1

5.2.2. Boundary condition case 1: GEM at analysis time, occultation location

In this first case, boundary conditions were taken from the GEM model data from the analysis-time run corresponding to each occultation event. GEM analysis times are 00Z and 12Z, matching the radiosonde launch times which the occultation events were chosen around. The GEM data exists over a uniform grid with a spacing of 0.25 º. Boundary conditions were obtained by bilinear interpolation within the grid to the location of the occultation tangent point. Boundary conditions were applied at the 10 mb pressure level, which occurs at a height of approximately 30 km.

The reference profile bounded by radiosonde measurements and the error with respect to the CHAMP product for a single example event which displays behaviour representative of the general trend (Event 30 in Table 4.1) is shown in Figure 5.2 below. This event is separated from the radiosonde launch by 124 km and 13 minutes. As radiosonde measurements will not occur at precisely 10 mb, the measurement closest to 10 mb was used to bound the profile, and was applied at its exact height.

Immediately below the boundary condition there is a short convergence distance towards zero mean error. This is similar to the behaviour observed with deliberately biased boundary conditions in section 4.4, suggesting that the boundary condition from the radiosonde is slightly in error in this case.

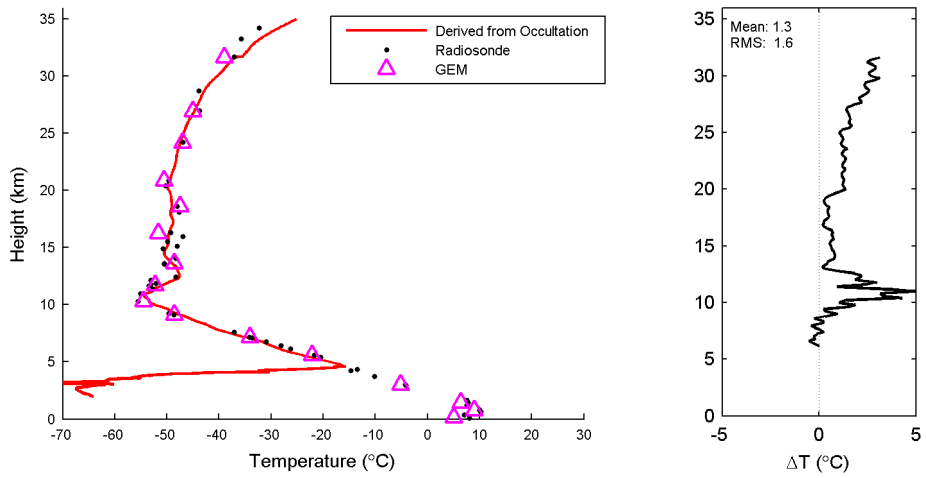

Figure 5.2: Example profile bounded by radiosonde and associated temperature error (Event 30 of table 4.1)

Ware et al (1996) suggest that radiosondes do experience reduced accuracy at high pressure levels, reaching errors as high as 4 ºC at 10 mb. Above the boundary condition height (31.7 km in this case), the accuracy of the profile degrades rapidly. The sharp loss of accuracy at the bottom of the profile is a result of lower troposphere data quality issues and occurs in the majority of events to some degree. In order to avoid biasing the results with known problem areas, all statistics shown do not include data below 6 km, or above the boundary condition.

The degradation in accuracy above the height at which the boundary condition is applied is a consistent effect in all profiles. An example of this effect is shown in Figure 5.3. A sample profile is derived using boundary conditions from analysis-time GEM temperatures at 10 mb (~21 km) and 50 mb (~10 km). The decreased accuracy above the boundary condition can be clearly seen. This divergence occurs regardless of boundary

condition height, and limits the use of the resulting profiles if only low altitude boundary conditions are available.

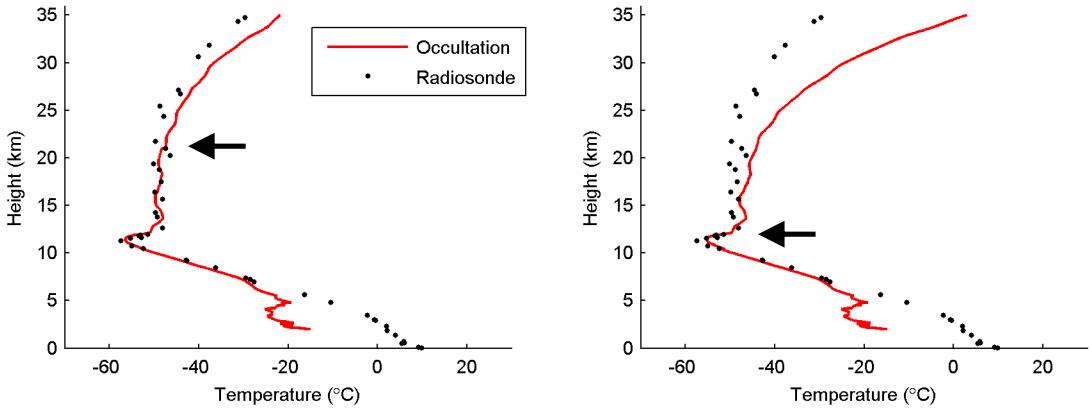

Figure 5.3: Boundary condition applied at (a) 21 km and (b) 10 km (Event 1 in Table 4.1)

The profile bounded by GEM data at analysis time and occultation location for this event is shown in figure 5.4. The 10 mb boundary condition occurs at 31.6 km in this case.

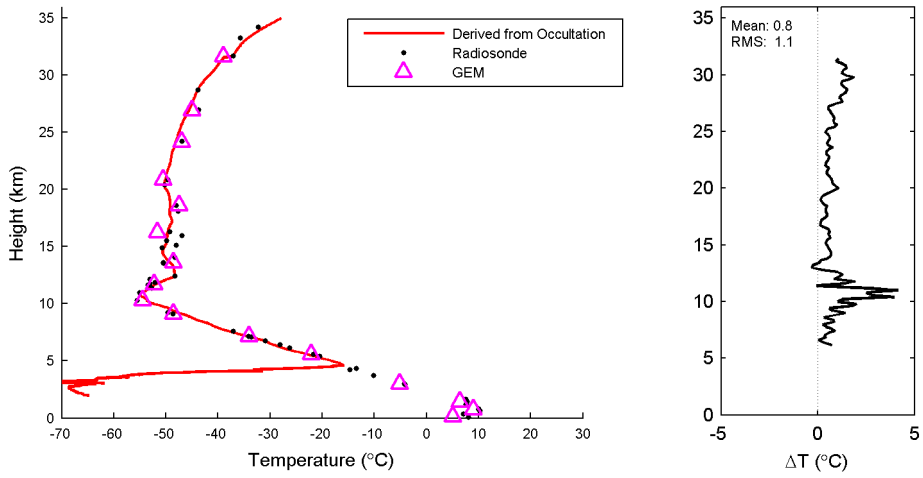

Figure 5.4: Example profile bounded by GEM at analysis time (Event 30 of table 4.1)

The profile overall is very similar to the radiosonde bounded case in Figure 5.2, but shows significantly improved mean and RMS error with respect to the CHAMP product. Inspection of the error curves suggests this is largely due to a more accurate boundary condition in the GEM data in this case, leading to a short convergence distance and improved accuracy overall.

This example event is shown because it shows an increase in accuracy visible from inspection. In the majority of events the GEM bounded profiles match the radiosonde bounded profiles much more closely. However, the general trend is for a slight improvement when using a GEM boundary condition. Statistics were computed across 33 events. Two events were excluded from the test because the radiosonde data did not extend high enough (only to 4 km and 13 km, respectively). Two additional events were excluded because the GEM temperature at 10 mb was a clear outlier. One of these two events with outlying GEM temperatures at 10 mb is shown in Figure 5.5. The outlying point at 10 mb is clear, standing well outside the trend of the lower GEM temperatures, which agree closely with the radiosonde. The effect of bounding the profile with this outlying value is very noticeable in the 10-30 km range.

Mean and RMS error for each event is shown in Figure 5.6. Collected mean and RMS error across all events is shown in Table 5.2. Cumulative distribution of the RMS error is shown in Figure 5.7. The temperature profiles derived in this work exhibit a slight warm bias with respect to the CHAMP temperature product. This is not a result of deriving the

profiles using boundary conditions from the GEM model however, as profiles derived using radiosonde boundary conditions are also biased warm with respect to CHAMP by nearly the same amount, as can be seen in Table 5.2.

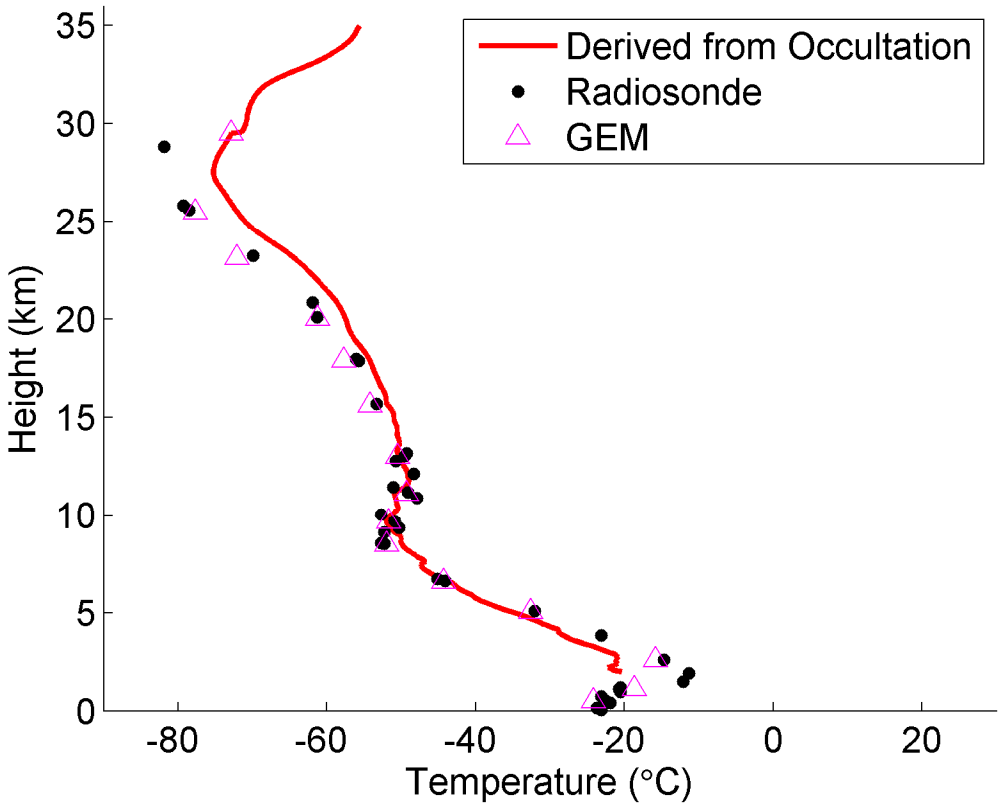

Figure 5.5: Event bounded by an outlying GEM temperature value at 10 mb (Event 5 of Table 4.1)

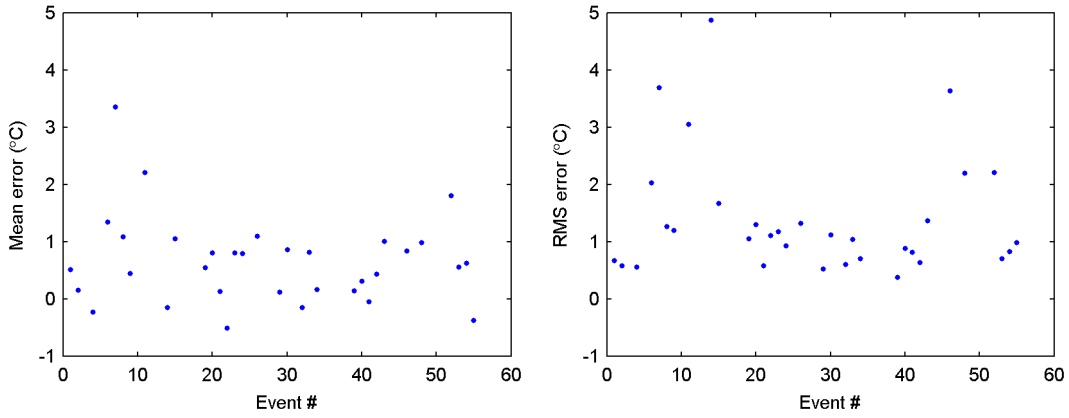

(a) (b)

Figure 5.6: Mean (a) and RMS (b) error for case 1 boundary conditions for all events

Table 5.2: Statistics for case 1 boundary condition across all events

	Radiosonde	Case 1
Mean error (ºC)	0.65	0.57
RMS error (ºC)	1.70	1.59
Improvement in RMS error over radiosonde	-	6%

The use of a boundary condition from the GEM model yields a slightly better RMS error on average than using a boundary condition from radiosonde, with an improvement factor of 6%. From Figure 5.6 (b) and the cumulative distribution shown in Figure 5.7, it can be seen that over 75% of events have an RMS error of less than 1.5 ºC, with a handful of events experiencing significantly higher errors. Some of these errors may be due to residual noise and error in the occultation derived refractivities, others may be a result of small errors in the boundary conditions from GEM.

A plot of temperature error RMS for case 1 bounded profiles as a function of temporal separation from the radiosonde launch and GEM time of applicability is given in Figure 5.8. The correlation between the two quantities is weak, with a coefficient of 0.24. It would be expected that the boundary condition would be less accurate the further in time it is from the occultation event. The lack of stronger correlation can be attributed to the fact that the rate of change of the temperature will vary from day to day; a delay of a given time interval will represent a greater shift in temperature for some events than for others.

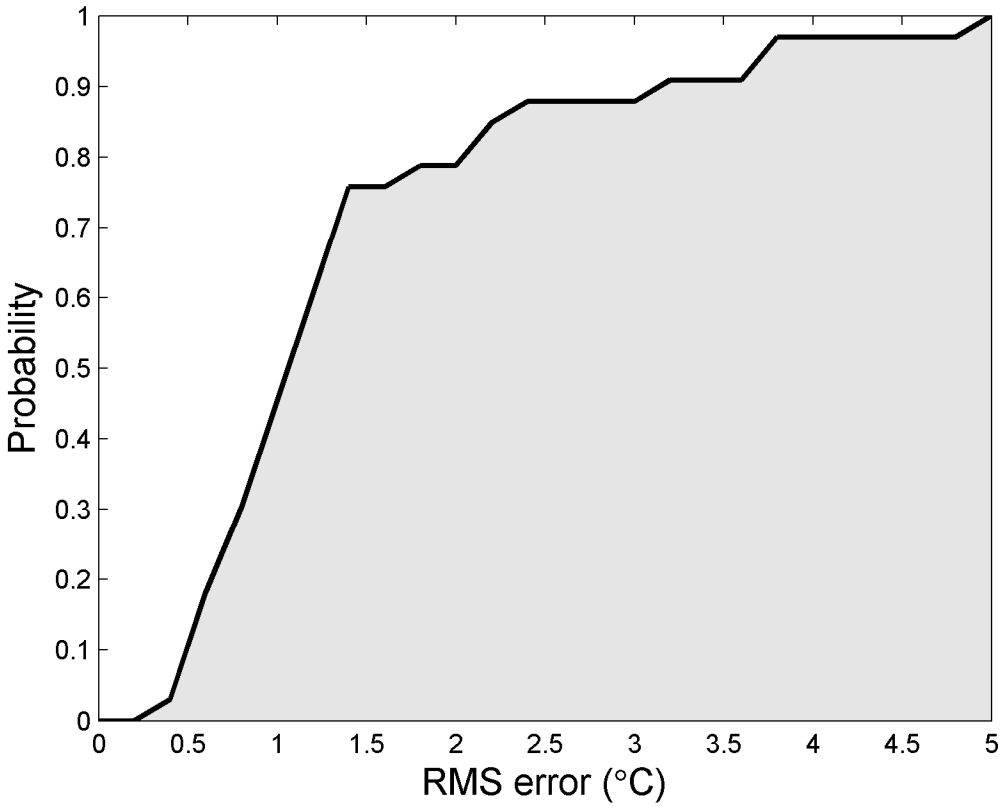

Figure 5.7: Cumulative distribution of RMS error for case 1 boundary conditions

The overall level of accuracy is comparable with results reported by other authors. Hajj et al (2002) report 0.5º K mean error and 1.5º K standard deviation between ECMWF profiles and GPS/MET retrievals down to ~6 - 8km.

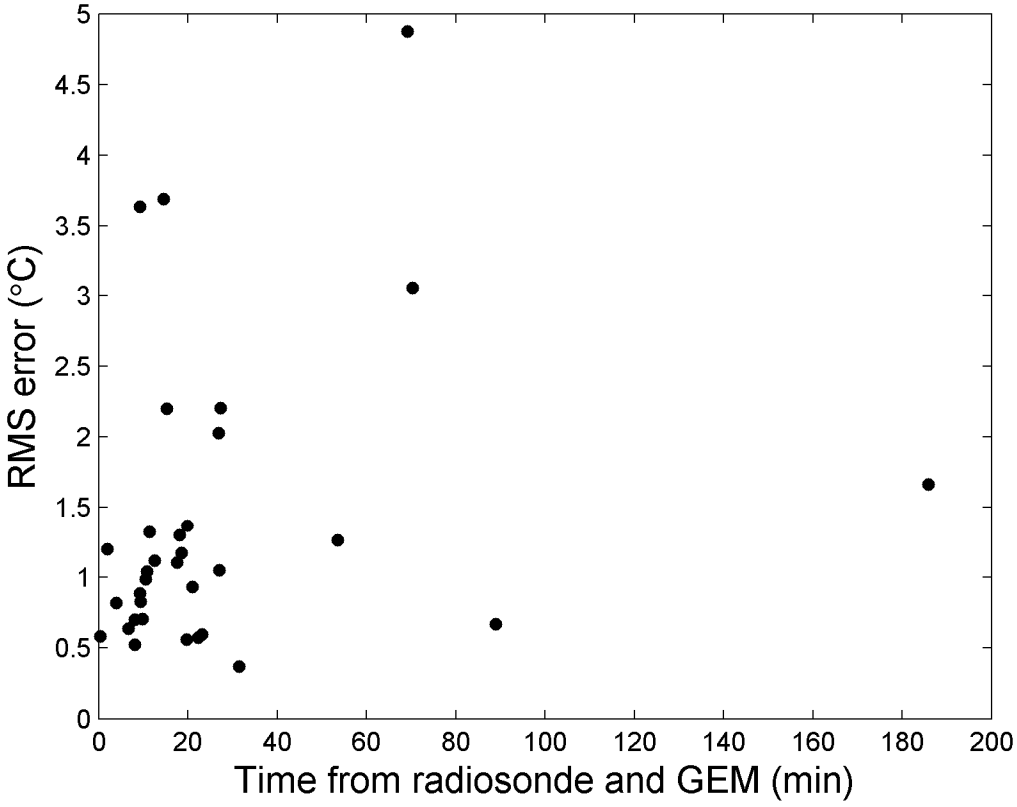

Figure 5.8: RMS error for case 1 boundary conditions as a function of temporal separation from radiosonde and GEM

5.2.3. Boundary condition case 2: Analysis-time GEM at radiosonde location

In the second case, profiles are bounded with data from the GEM model at analysis time, but interpolated to the location of the radiosonde, rather than the occultation event. This shows to what extent the improvement observed in case 1 is due to the shift in the spatial

location of the boundary value, and to what extent it is from using GEM as a data source rather than radiosonde.

Overall, profiles bounded with values from the radiosonde location give comparable errors to those bounded at occultation location. Figure 5.9 shows an event representative of the trend in this case. Figure 5.10 shows the associated errors for a profile bounded by radiosonde, GEM at occultation location, and GEM at radiosonde location. This is Event 21 in Table 4.1, 198 km and 0 minutes from the radiosonde launch.

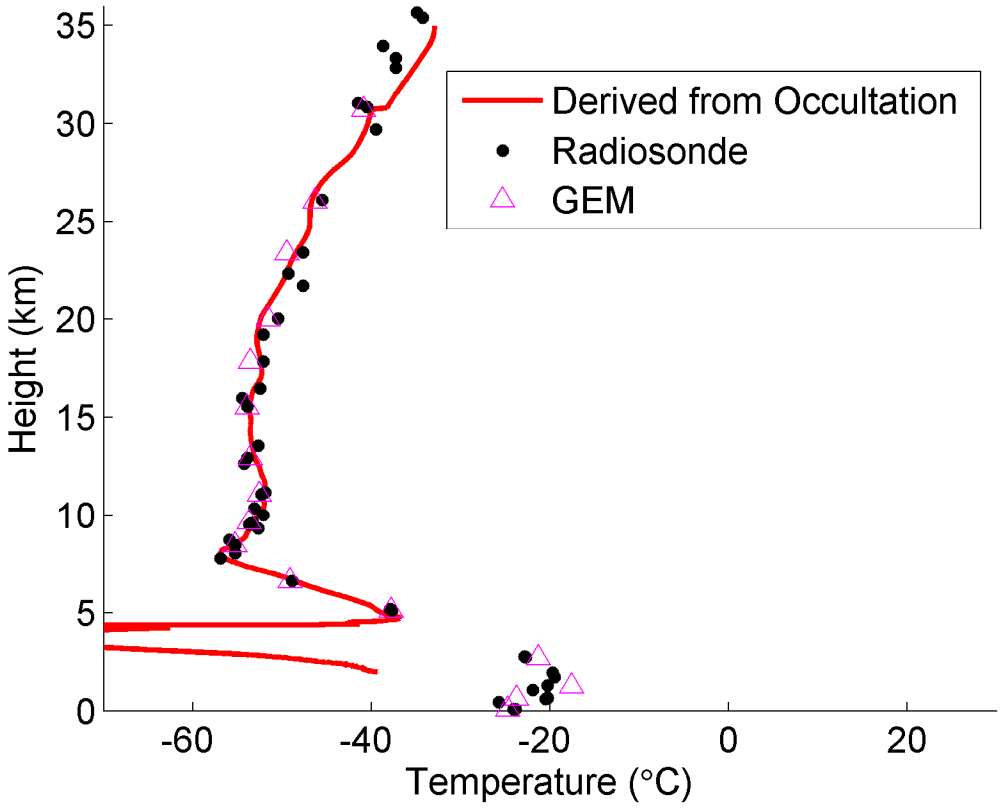

Figure 5.9: Temperature profile for Event 21 of Table 4.1

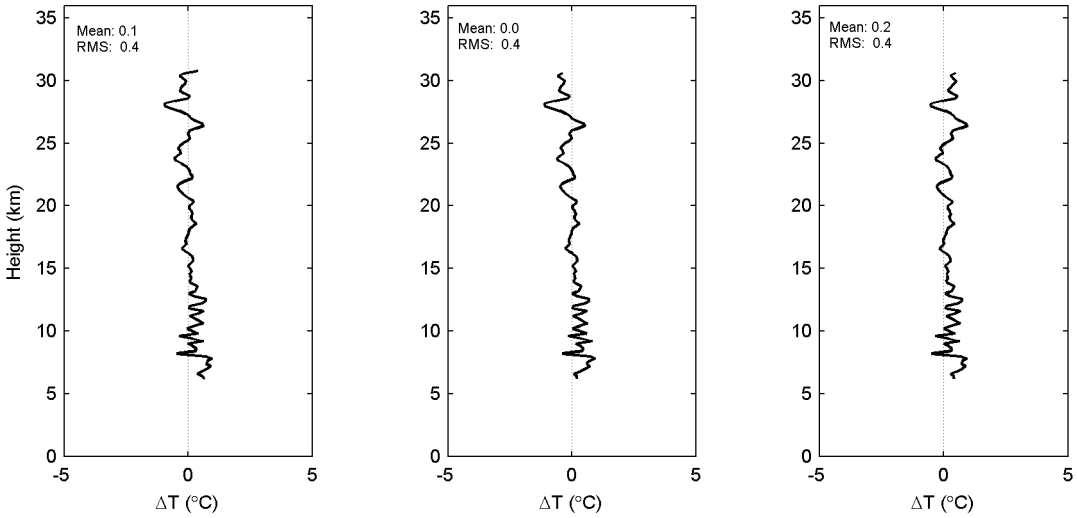

Figure 5.10: Error curves for a profile bounded with (a) radiosonde, (b) GEM at occultation location, and (c) GEM at radiosonde location (Event 21 in Table 4.1)

The difference is visible as a change in the bounding temperature (applied here at ~30.8 km), with the profiles converging at lower altitudes. Plots of mean and RMS error for all events are shown in Figure 5.11. Cumulative distribution of RMS error is shown in Figure 5.12.

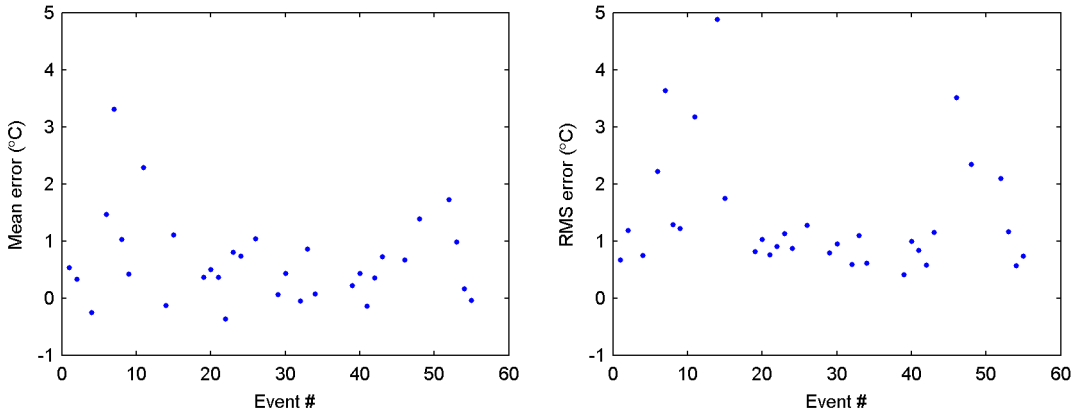

(a) (b)

Figure 5.11: Mean (a) and RMS (b) error for case 2 boundary conditions for all events

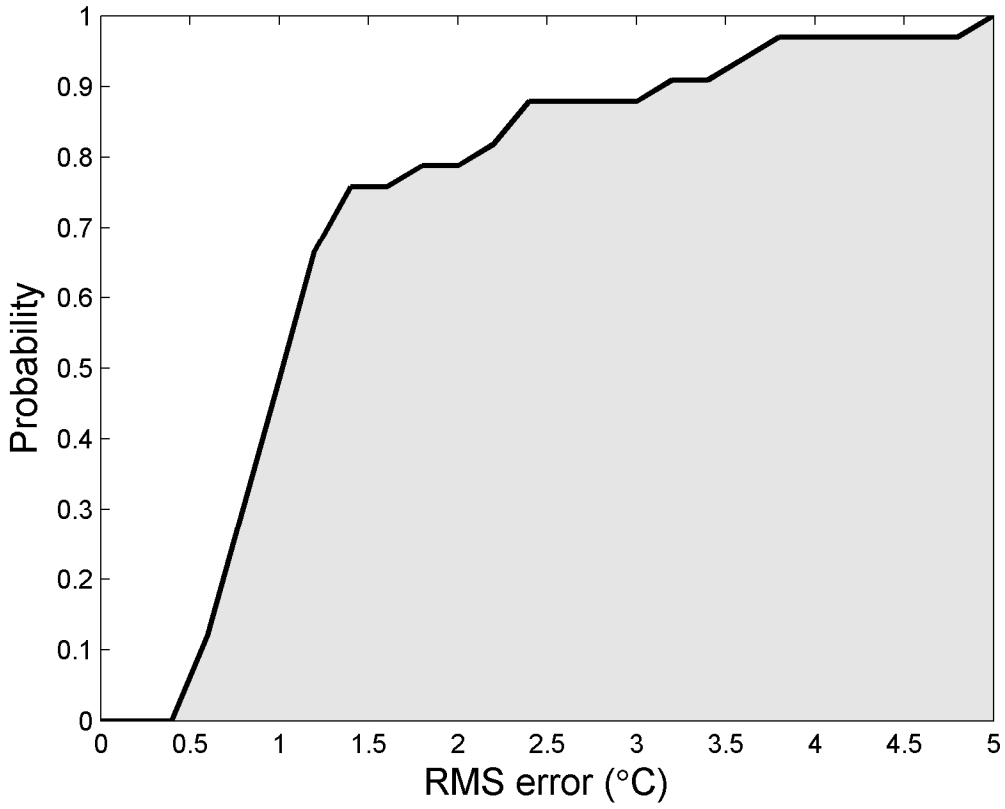

Figure 5.12: Cumulative distribution of RMS error for case 2 boundary conditions

By inspection, the differences from the first case are negligible. This is confirmed by the statistics for all events, shown in Table 5.3. This indicates that the slight improvement over the profiles derived from a radiosonde boundary condition can be attributed to the use of the GEM as a source for temperature values, and not to the improved spatial location of the boundary condition. It also suggests that the results are not highly sensitive to spatial interpolation, at least for the distances present in these data. This is confirmed by an examination of the temperature error RMS for profiles computed in this case as a function of distance from the radiosonde launch site (to which the GEM temperatures were interpolated), shown in Figure 5.13. The two quantities are almost entirely uncorrelated, having a computed correlation coefficient of -0.09. This is not unexpected, given the poor horizontal resolution of radio occultation.

Table 5.3 Statistics for case 2 boundary condition across all events

	Radiosonde	Case 2
Mean error (ºC)	0.65	0.57
RMS error (ºC)	1.70	1.59
Improvement in RMS error over radiosonde	-	6%

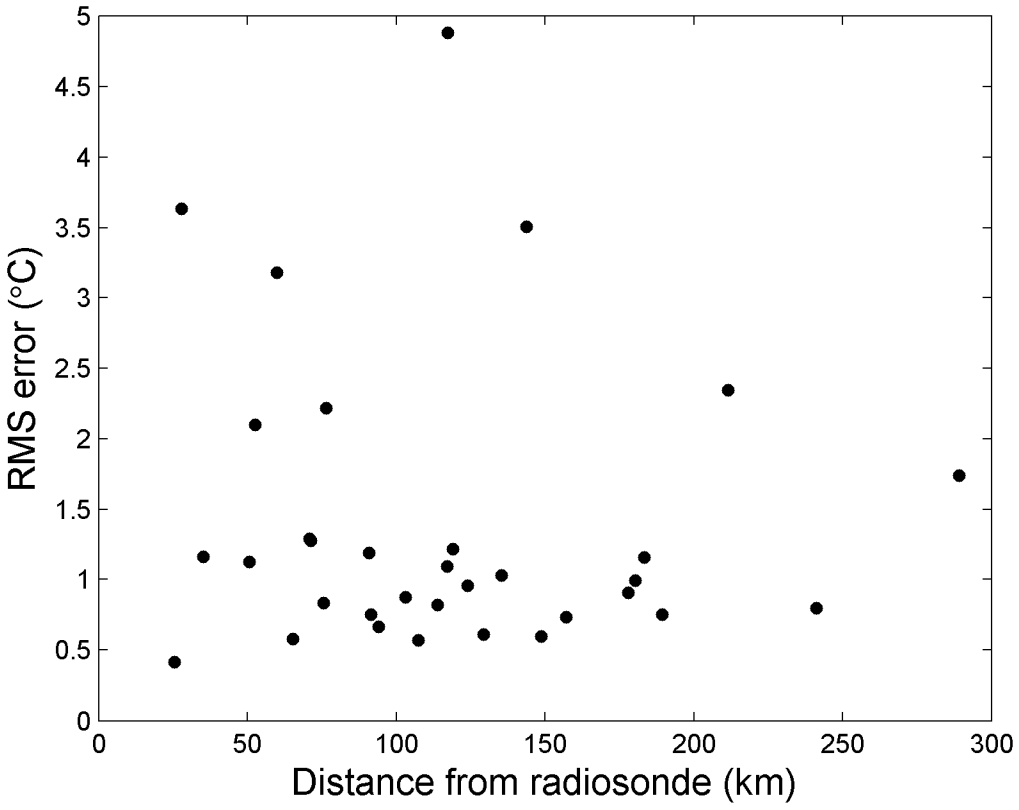

Figure 5.13: RMS error for case 2 boundary conditions as a function of distance from radiosonde

5.2.4. Boundary condition case 3: GEM at 12 hour forecast, occultation location

In the third case, curves are bounded with temperature values from the GEM 12-hour forecast product initialized 12 hours before each event. Thus, the temperatures are forecasted but still have a time of applicability corresponding to radiosonde and occultation event. Seven of the events tested in cases 1 and 2 were excluded from this test as forecasted temperatures at 10 mb were not available. In total, forecasted temperatures at 10 mb were available for 26 retrievable events. The temperature profile for an event which depicts the general trend of the data is shown in Figure 5.14, using a

boundary condition of the GEM temperature at analysis time. Error profiles for the event are shown in Figure 5.15. On the left is the profile bounded with the analysis-time data as in case 1, and on the right is the 12-hour forecasted data. This is Event 34 of Table 4.1, and is separated from the time for which the boundary values are applicable by 10 minutes. The boundary is applied at 32.2 km

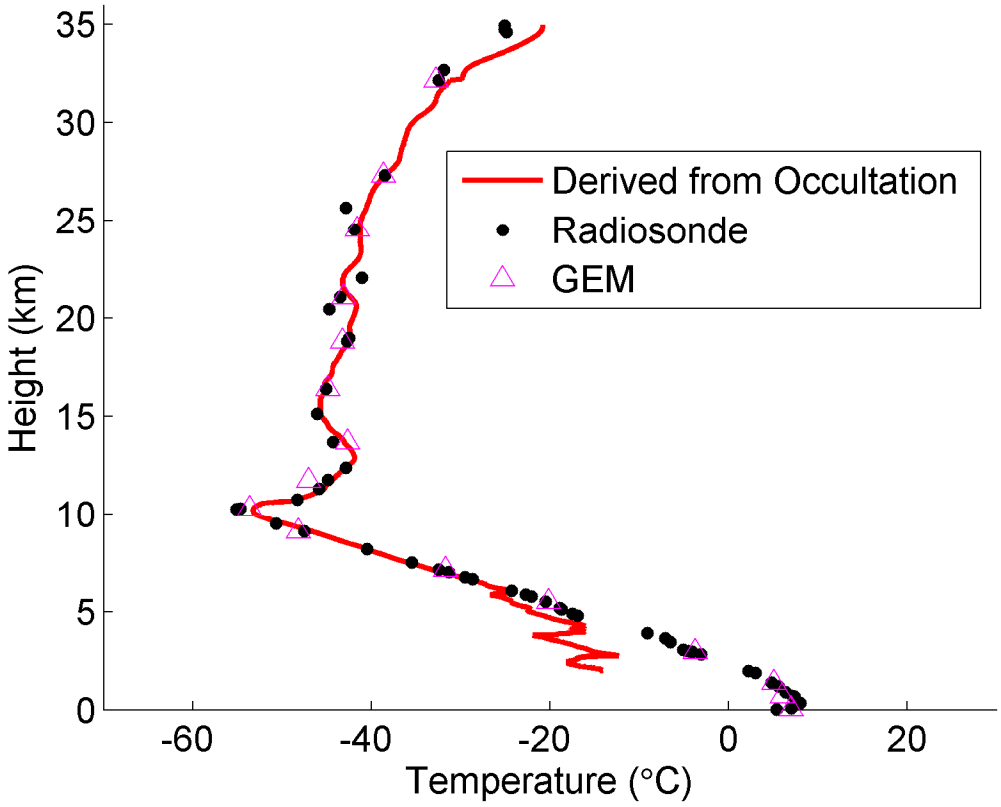

Figure 5.14: Temperature profile for Event 34 of Table 4.1

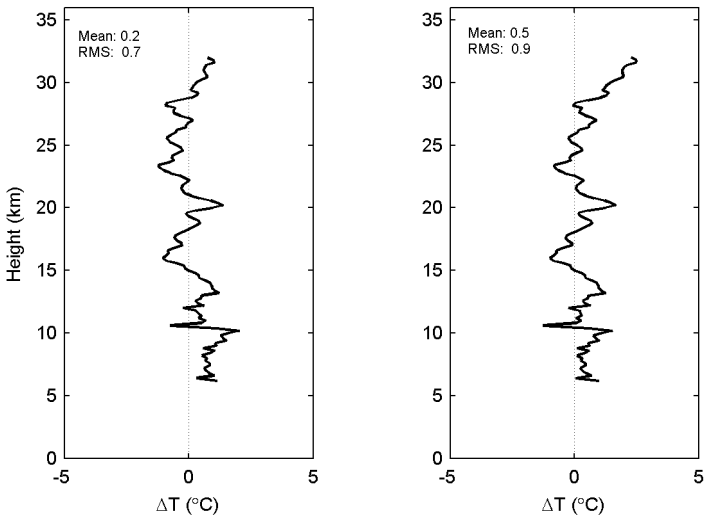

(a) (b)

Figure 5.15: Error profiles bounded with (a) GEM at analysis time and (b) 12-hour forecast (event 52 in Table 4.1)

The profile computed with a forecasted boundary condition shows a slight increase in error compared to the profile bounded by the analysis time temperature. Inspection indicates that the forecasted boundary value is biased more than the analysis-time value, giving a larger error at and near the 32 km height at which it is applied. In the lower half of the profile, after converging, the two error curves are very similar. This increase in error is characteristic of the trend across all events tested. While the errors in the profiles bounded by the forecasted temperature are less than in those bounded by analysis-time temperature in some cases, in general the analysis-time temperatures give better results. Mean and RMS errors for all 26 events are shown in Figure 5.16. Cumulative distributions of RMS for both cases 1 and 3 for these 26 events are shown in Figure 5.17.

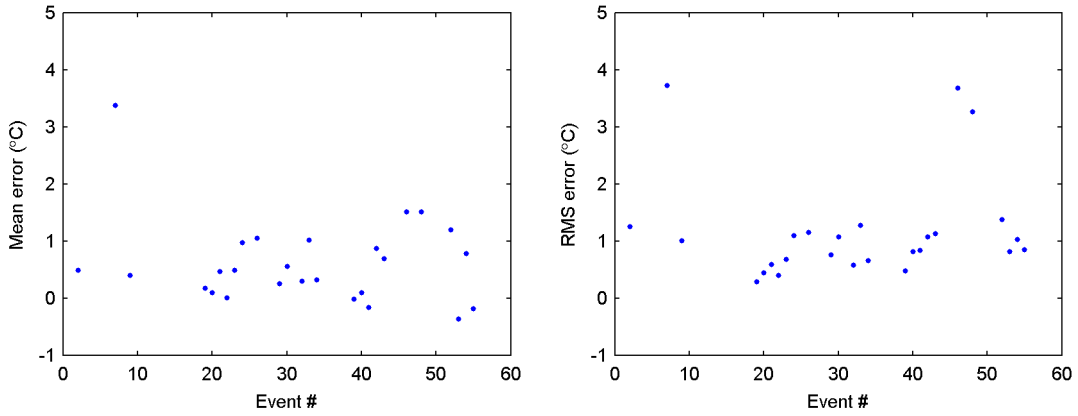

(a) (b)

Figure 5.16: Mean (a) and RMS (b) error for case 3 boundary conditions for all events

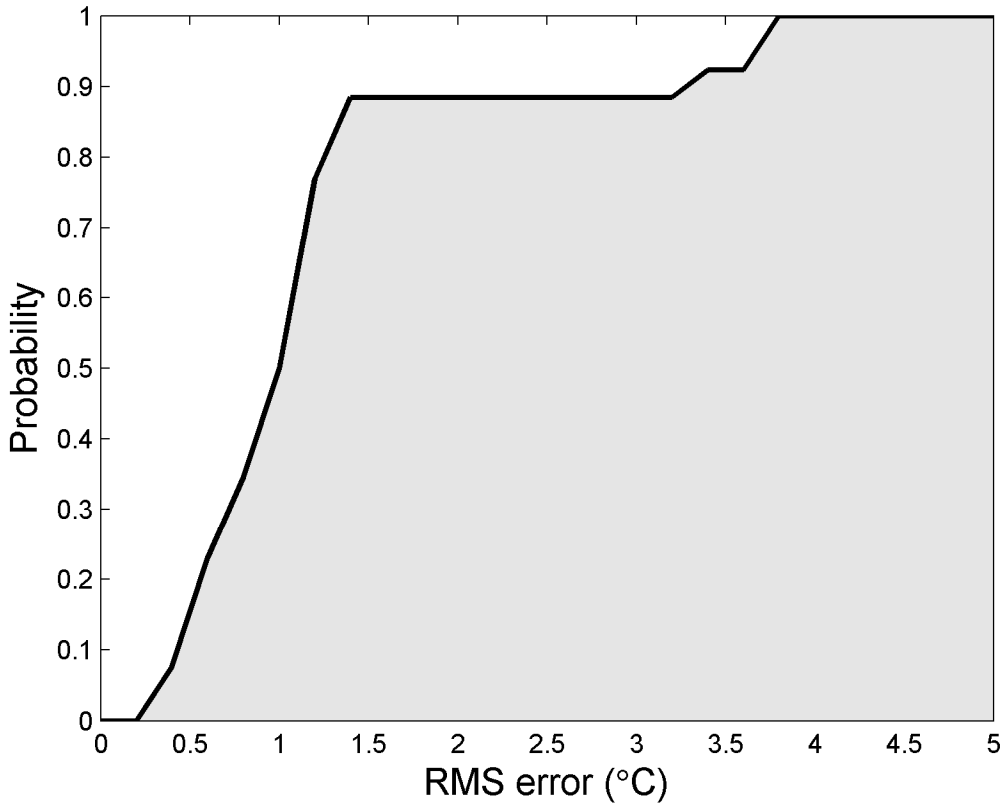

Figure 5.17: Cumulative distribution of RMS error for case 3 boundary conditions

Statistics for all events in this case are shown in Table 5.4. Statistics shown for profiles computed with a boundary condition from radiosonde and case 1 include only the 26 events used for the case 3 test, so as not to bias the results with the seven excluded events. Temperature profiles computed using case 1 boundary conditions show comparable improvement in error RMS over profiles bounded by radiosonde temperatures to that observed using 33 events (see Table 5.2), while temperature profiles computed with case 3 boundary conditions give comparable accuracy to radiosonde bounded profiles.

Table 5.4 Statistics for case 1 and 3 boundary condition across case 3 events

	Radiosonde	Case 1	Case 3
Mean error (ºC)	0.66	0.56	0.63
RMS error (ºC)	1.52	1.39	1.53
Improvement in RMS error over radiosonde	-	9%	-1%

As the only difference between the profiles computed in case 1 and in case 3 is the temperature value used as a boundary condition, it is reasonable to expect that the increase in error in the profiles reflects an increase in error in the boundary condition value. Figure 5.18 shows the temperature difference between the 12 hour forecast temperatures and radiosonde, compared with the difference between analysis-time temperatures and radiosonde.

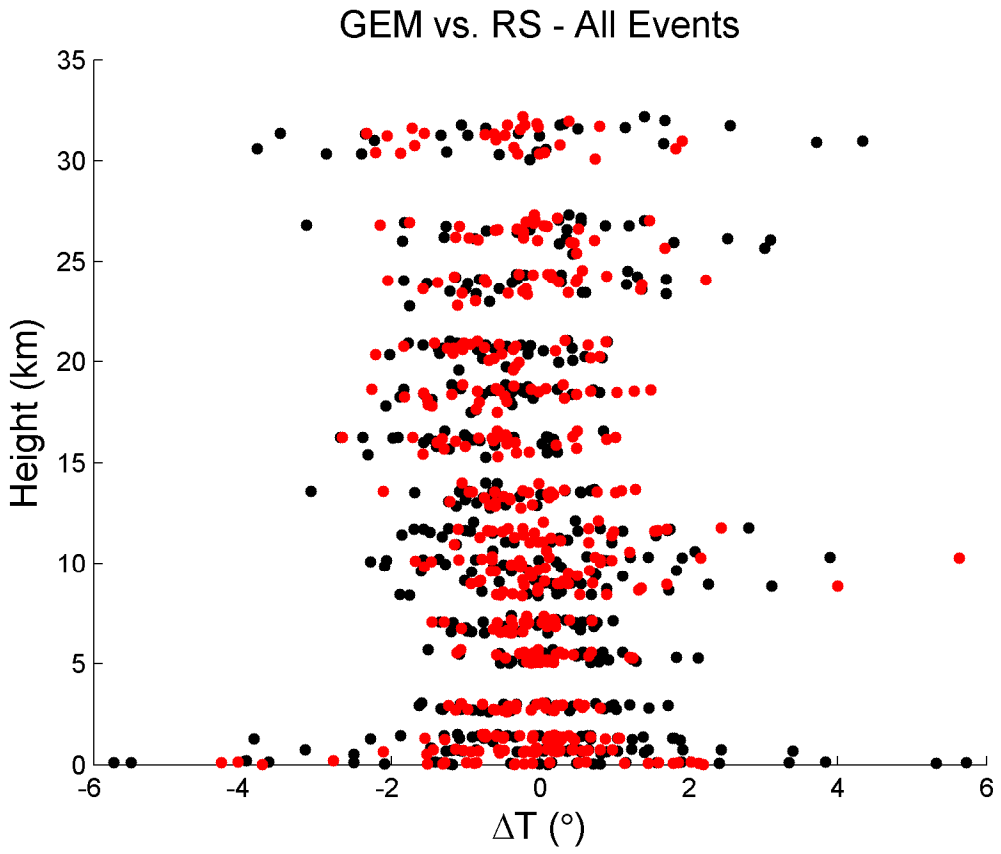

Figure 5.18: Difference between analysis time and forecast temperatures as compared to difference between analysis time GEM and radiosonde

It can be seen that the forecasted temperatures tend to have a slightly higher range of error than the analysis-time temperatures, when compared to radiosonde measurements. The RMS of the difference between analysis-time temperature and radiosonde is 1.0 ºC, compared to 1.4 ºC for the 12 hour forecast. Referring to Figure 4.8, a 0.4 ºC increase in boundary condition error is expected to produce approximately 0.1 ºC additional RMS error in the temperature profiles. This is comparable to the additional 0.14 ºC RMS error observed and listed in Table 5.4.

5.3. Humidity retrieval using GEM temperature profiles

As outlined in Chapter 3, in order to retrieve humidity information from radio occultation measurements, external information about either the temperature or pressure is required. In practice, a temperature profile from an NWP is most commonly used. Here, temperature profiles taken from the GEM model were used to derive humidity, and the results compared to radiosonde observations. Temperature profiles used are from the analysis-time GEM model runs, and cover 16 pressure levels between 1000 mb and 10 mb. The 16 data points are interpolated to the resolution of the occultation data using a piecewise cubic spline. In order to avoid any possible effects from using GEM boundary conditions, the boundary condition in all cases is taken from the MSISE model at 50 km.

5.3.1. GEM vertical resolution

A primary limitation of using the GEM temperature profiles to determine humidity is their sparse vertical resolution. In areas of large temperature gradients, most notably around the tropopause, the resolution of the model is not sufficient to describe the temperature profile well enough to obtain accurate humidity results. An example event in which the tropopause is not adequately sampled by the GEM profile is shown in Figure 5.19.

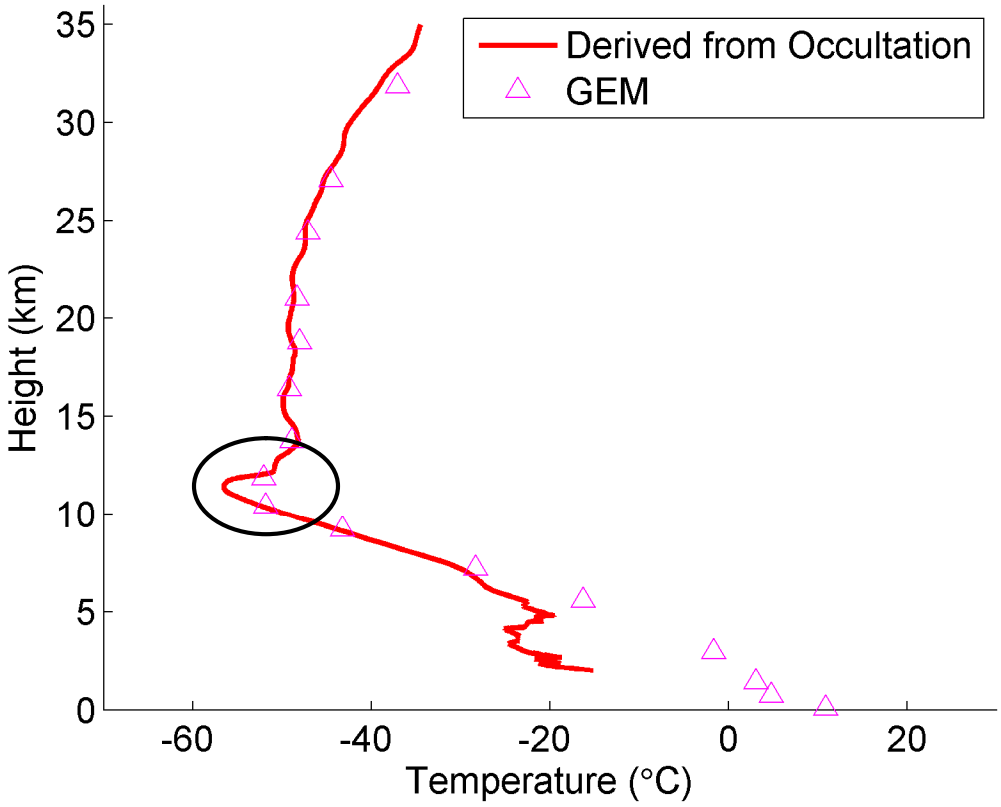

Figure 5.19: Temperature profile for an event in which the tropopause is not adequately sampled by the GEM profile (Event 1 of Table 4.1)

Here, the GEM model pressure levels bracket the tropopause, and the magnitude of the peak is not observed. The resulting water vapour pressure and dew point depression (difference between the temperature and the dew point) profiles derived from the occultation data for this event are shown in Figure 5.20, with radiosonde data for comparison. The effect of poor tropopause sampling is clearly visible, with the calculated water vapour pressure being biased high and the dew point depression significantly in error in the vicinity of the tropopause, 10-12 km.

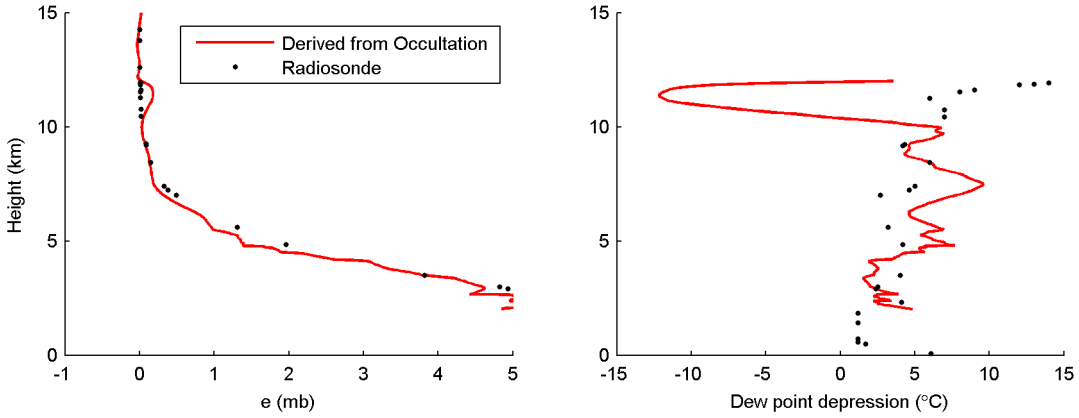

Figure 5.20: Water vapour pressure (a) and dew point depression (b) for an event in which the tropopause is not adequately sampled by the GEM profile (Event 1 of Table 4.1)

The effect of under sampling the tropopause is significant enough that calculations yield negative dew point depressions, a situation which has no practical meaning; dew point depression is non-negative by definition, as the dew point cannot be higher than the true temperature. It is good to note that the effect of the under sampling is confined to the values around the under sampled region (in this case, the tropopause). The estimated humidity below ten kilometres, where the temperature gradient is smooth enough to be described by the GEM profile, appears to be unaffected.

5.3.2. Practical effects of refractivity and temperature error on humidity retrieval

The fact that the combined effect of refractivity and temperature error can approach or exceed the value of the wet component of the refractivity when it is small, in some cases resulting in negative values of water vapour pressure being computed, is discussed in

Section 4.6. The likelihood of this occurring is higher for drier events, and at higher altitudes within a given event, as the absolute error constitutes a greater relative error. An example of this effect is shown in Figure 5.21 below.

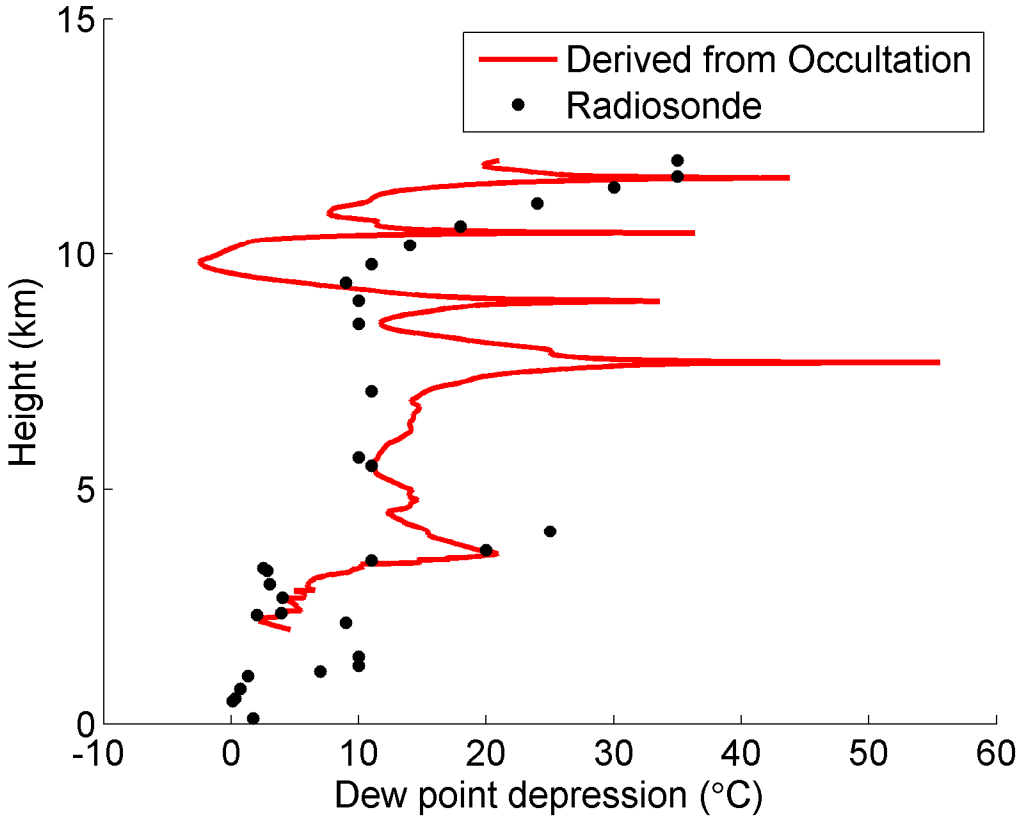

Figure 5.21: Dew point depression profile in a case where negative water vapour pressures result from refractivity and temperature error (Event 39 in Table 4.1)

The error spikes from 7-12 km result from this effect. Below 7 km, where the water vapour signal is stronger, negative water vapour pressures do not result from the computation and these error spikes are no longer present. This effect is most pronounced when the humidity is viewed in terms of dew point, as the values are outside the intended range of the equations to convert to dew point and they give progressively erroneous

returns as a result. The effect is not as severe if the water vapour pressure is examined, as the small negative values only occur when the true value is near enough to zero that it can be totally dominated by the noise. Both the full water vapour pressure profile and a close up of the values causing the effect are shown in Figure 5.22.

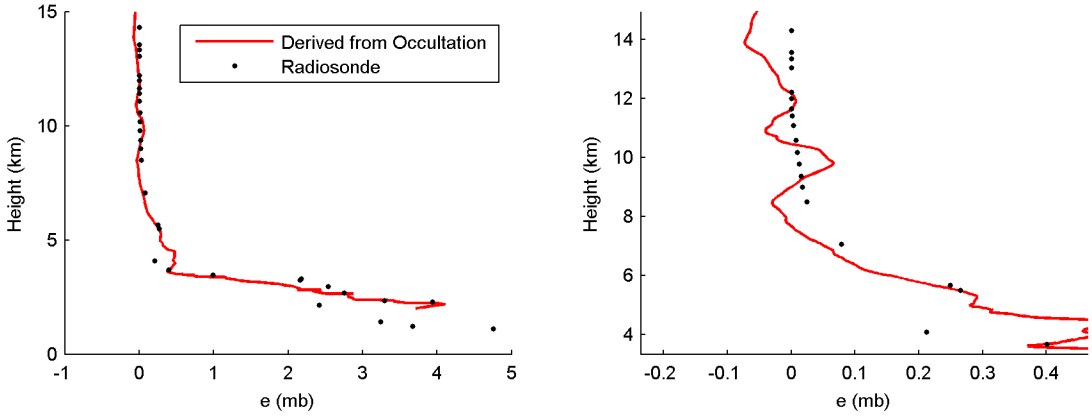

(a) (b)

Figure 5.22: Water vapour pressure profile (a) and close up of relevant region (b) for an event where negative water vapour pressures result from the calculation (Event 39 in Table 4.1)

The fluctuating nature of errors is clear in Figure 5.22 (b), indicating that the error in the refractivity and/or temperature profiles which causes this effect behaves more like noise, and not a systematic bias. It is also possible for significant negative partial pressures to arise from RO in some retrievals, possibly as a result of atmospheric multipath or non-spherical symmetry (Gerding & Weisheimer, 2003). This is not believed to be the case for the events seen in this work however, as the magnitude of the negative partial pressures is on the sub-millibar level, while multipath induced effects can reach 10 mb in some cases (Marquardt et al, 2000),

While these figures focus on highlighting the negative values of *e*, the problem cannot be avoided simply be eliminating these negative values. Figure 5.23 shows the resulting profiles if *e* is forced to be non-negative for all heights for the same event.

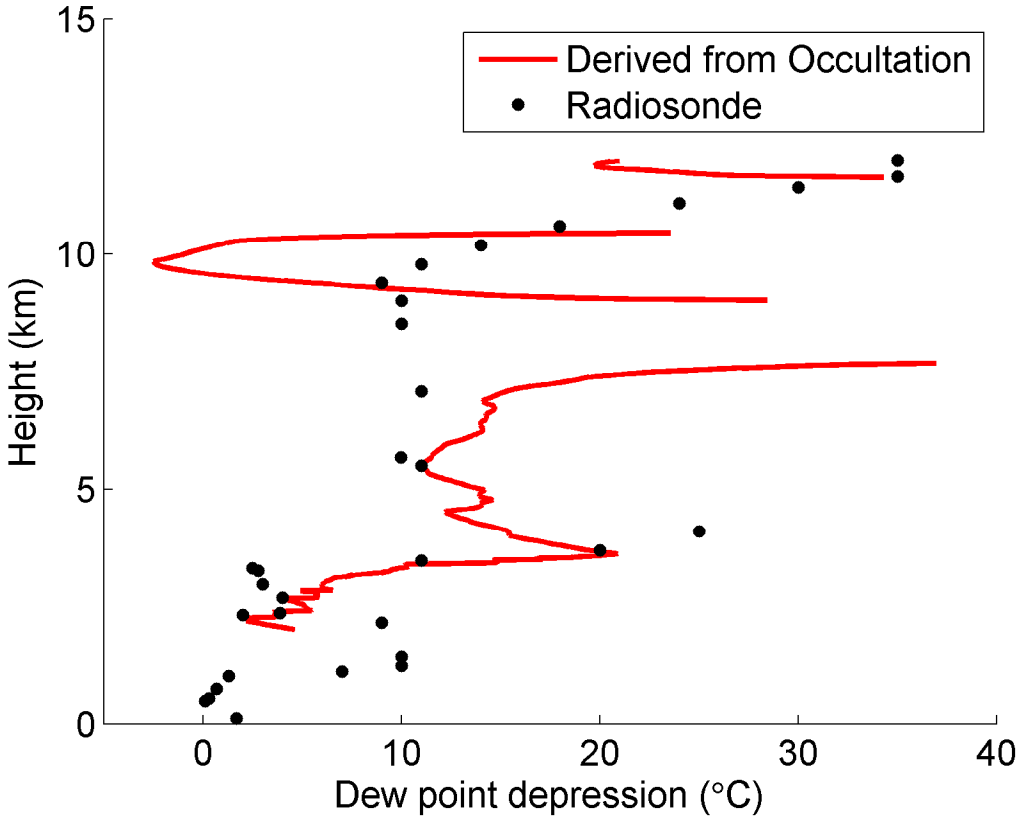

Figure 5.23: Dew point depression from a *e* profile constrained to be non-negative (Event 39 of Table 4.1)

In practice, this is no different than flagging and rejecting dew points at heights where *e* is negative, as setting it to zero here results in an undefined dew point. The computed values of *e* near the obviously erroneous points are also affected by the noise, and the result is very apparent, especially from 9-11 km. Slightly better results are obtained from smoothing out the noise in the *e* profile, as seen in Figure 5.24.

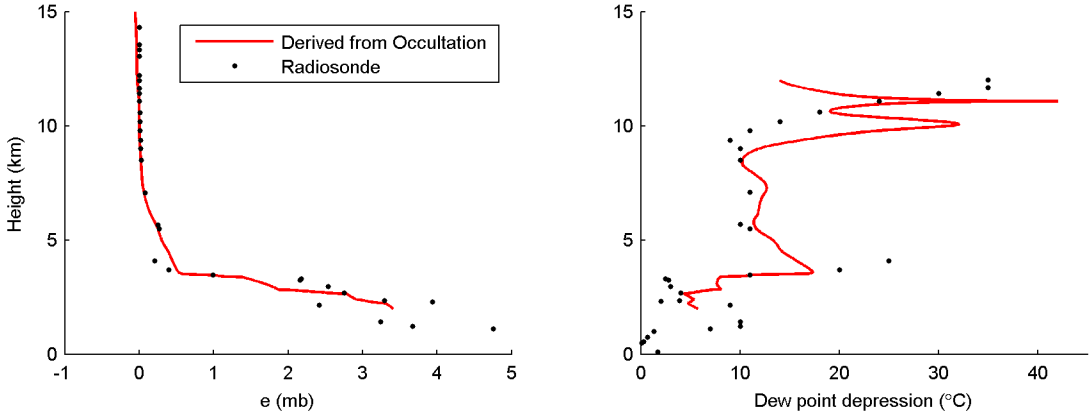

Figure 5.24: *e* (a) and dew point depression (b) profiles with *e* smoothed over 200 samples (Event 39 of Table 4.1)

Here *e* has been smoothed by a simple moving average filter over 200 samples, which corresponds to roughly 2 km. While some obvious outliers remain in the 9-11 km range, the majority have been smoothed out, at the expense of resolution and accuracy at the lower altitudes.

As seen in Figure 4.11, it can be expected that the effect of the refractivity/temperature noise will be most pronounced in events with the least humidity, as the noise is greater in relation to the total signal. Figure 5.25 attempts to support this, showing the height of the lowest negative *e* value as a function of the mean true (taken from radiosonde) *e* below 15 km for all events which experience negative *e* values. The humidity signal decreases with increasing altitude for all events, but the point at which the refractivity/temperature noise exceeds the signal can be expected to be higher for wetter events.

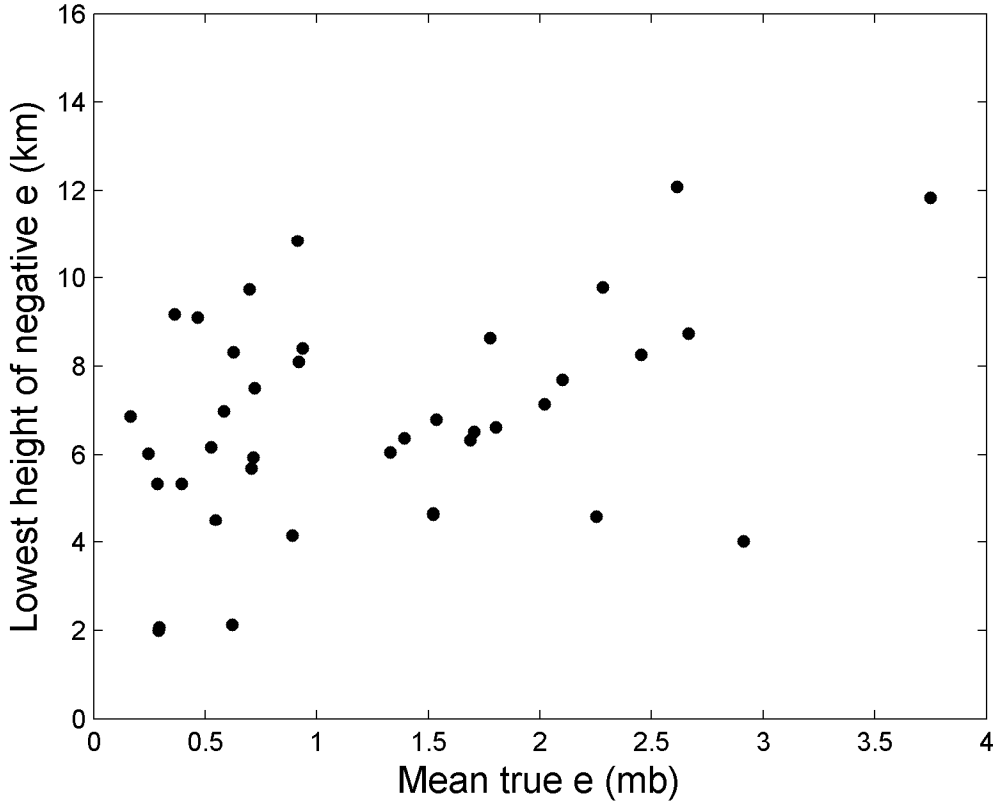

Figure 5.25: Height of lowest negative *e* value vs. mean radiosonde *e*

These two quantities are weakly correlated, having a correlation coefficient of only 0.31. It is worthwhile however to also examine the extreme cases. There are only three events where the noise is able to overcome the signal right down to 2 km, which is the lowest height that humidity was computed to, and these three events are among the driest in the data set. This suggests that computational errors will be a greater problem for drier conditions, such as those which occur in the Canadian arctic. In dry conditions, greater refractivity and temperature accuracy will be necessary to obtain accurate humidity retrievals than in wetter regions.

Overall statistics for all retrievable events are given in Table 5.5 below. Statistics are computed between 2 and 12 km, which encompasses the tropopause and below. *e* and dew point depression are compared against radiosonde.

Table 5.5: Statistics of occultation derived humidity minus radiosonde

	e (mb)	Dew point depression (ºC)
Mean	0.71	-6.34
RMS	3.20	15.71

For these results, no smoothing or other method was applied to the derived *e* values to limit the expansion of error into the dew point. As a result, the overall dew point errors are much larger than the errors in *e*. However, even if smoothing is uniformly applied over 200 samples, mean and RMS errors in dew point depression are nearly unchanged, at -6.02ºC and 15.80ºC respectively.

The errors in *e* are slightly higher than those reported by other authors. Rocken et al (1997) show agreement between GPS/MET data (using NCEP temperature profiles) and radiosonde below 0.3 mb on average, with a standard deviation of 0.5 mb at 3 km altitude. Marquardt et al (2000) obtain 50-75% relative error in specific humidity between GPS/MET (using ECMWF temperature profiles) and ECMWF. Relative error in *e* in this work is 81% on average. This increase in error may be in part due to GEM temperature profiles, but more likely results from limitations in the processing applied in this work as opposed to that in place at dedicated processing centres. Rocken et al (1997)

suggest that a temperature profile accuracy of 2 ºC will make it possible to obtain water vapour pressure accurate to 0.5 mb. As the GEM temperatures are accurate to 2 ºC as compared to radiosonde (Figure 5.1), the higher than expected *e* error most likely arises from error in the occultation derived refractivity, in turn arising from limitations in the processing employed in this work. Improved occultation data pre-cleaning (e.g. for half cycle slips) and more robust error smoothing in the bending angles and refractivities would likely reduce the water vapour pressure errors, as would application of the canonical transform technique.

5.4. Current Public GEM Products

The current public data products of the GEM model differ slightly from the GEM data used in this work. Currently, the GEM model is run globally for a grid with a spacing of 0.9º, and regionally for a grid covering North America having a spacing of 15 km, shown in Figure 5.26. The regional model has 58 vertical computation levels, but only 28 levels are included in the published product.

CMC provides two public data products: a high resolution product using the full horizontal grid spacing of 15 km over the extent of Canada, and a low resolution product with a horizontal spacing of 60 km. The vertical resolution of both products is 28 isobaric levels, shown in Table 5.6. Two initialization runs are made daily, at 00Z and 12Z. Forecasts are also produced for 3-hour intervals for the high resolution product, and for 6-hour intervals for the low resolution product, up to 48 hours from initialization time.

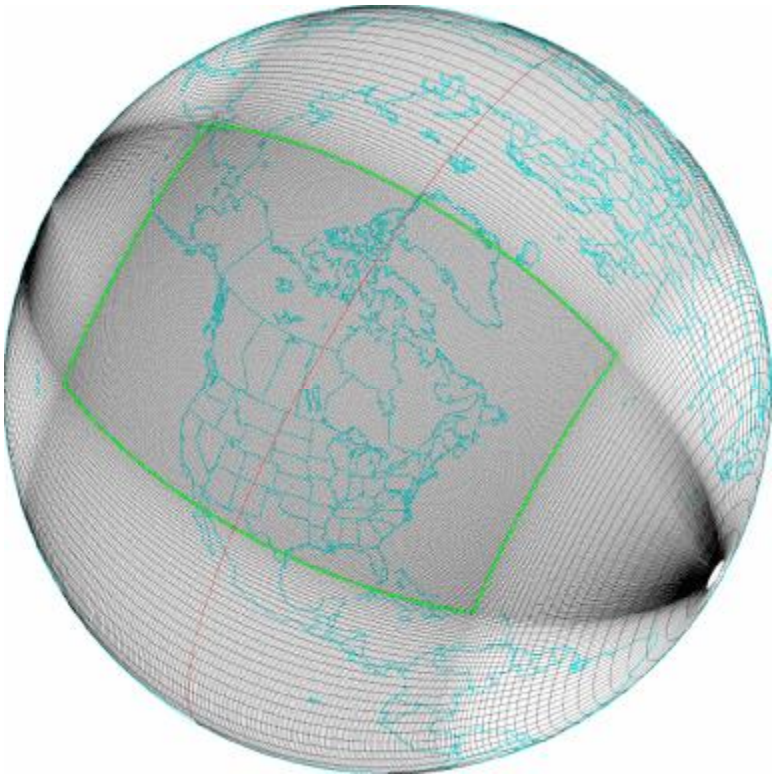

Figure 5.26: GEM regional grid as of May 18, 2004 (from Canadian Meteorological Centre, 2007)

In comparison to Table 5.1, the primary differences between the vertical resolution of the GEM data used here and that currently available from the CMC is increased resolution at lower altitudes (between 150-1000 mb), and a lack of coverage above 50 mb in the current product.

The horizontal resolution of the current grid is comparable to that used in this work, having a current spacing of 15 km, as compared to the ~14-28 km spacing of the uniform grid used here.

Table 5.6: Isobaric levels in the current public GEM product

Level	Pressure (mb)	Level	Pressure (mb)
1	1015	15	550
2	1000	16	500
3	985	17	450
4	970	18	400
5	950	19	350
6	925	20	300
7	900	21	275
8	875	22	250
9	850	23	225
10	800	24	200
11	750	25	175
12	700	26	150
13	650	27	100
14	600	28	50

The greater number of pressure levels between 150 and 1000 mb should provide increased resolution in humidity retrievals derived using GEM temperatures as input. These extra pressure levels all occur at or below the tropopause, which is the region over which water vapour retrievals are relevant.

The lack of pressure levels up to 10mb in the public product places limitations on mid-altitude temperature retrievals using GEM boundary conditions. Figure 5.3 (b) shows a case where the boundary condition is applied at 50 mb (~10 km in this case), the upper extent of the public product. The degradation above the boundary condition can be

clearly seen in the figure, and the temperatures above 10 km are not accurate. If the public product was used as a source of boundary conditions, only temperatures at and below the tropopause would be accurately retrievable. Alternatively, researchers seeking to use the current GEM products could seek to obtain data from one of the 58 computational levels of the model at a higher altitude than is published in the public product.

5.5. Summary

The use of the GEM product as a source for boundary conditions yields retrievals comparable in accuracy to the CHAMP temperature profile product as the CHAMP product is to the ECMWF output. Use of the GEM model shows an improvement in accuracy over using radiosonde observations as a source for boundary conditions, with an average level of improvement of 6%. This confirms the suitability of GEM as a source of boundary condition data for occultation retrievals.

Use of temperature profiles from the GEM model to derive humidity profiles from occultation data gives partial water vapour pressure accurate to 0.7 mb in mean, and 3.1 mb in standard deviation. This is slightly worse than results obtained by other authors, in part because of insufficient vertical resolution around the tropopause and difficulty in retrieving humidity for extremely dry events. However, the accuracy of the GEM temperatures as compared to radiosonde is at the levels recommended in the literature for humidity retrievals accurate to 0.5 mb, suggesting it is suitable for this application.

Chapter 6 - Conclusions and Recommendations

This chapter summarizes the findings of this work with respect to the initial objectives, and identifies recommendations for future work. The primary objectives of this work were to evaluate the accuracy requirements for orbits and NWP products for successful retrievals, and to determine if the GEM NWP is a suitable source of required inputs into radio occultation retrievals. Routines were implemented to perform temperature and humidity retrievals beginning with the excess atmospheric phase delay, using data from the GEM model as input.

6.1. Conclusions

With regards to the accuracy requirements of orbits, it has been seen that errors in the temperature profiles resulting from residual orbit errors are minimal with respect to the overall temperature accuracy, at error levels currently present in the CHAMP orbits. The contribution of orbital error is on the order of 0.05-0.1 ºC, and overall temperature error is at the level of 1-2 ºC. As it can be expected that the accuracy of LEO orbits will continue to improve as continued improvements are made to modeling the gravity field (until limited by other factors, e.g. atmospheric drag, albedo pressure), residual orbital error should not be a concern for future missions.

The accuracy required of the temperature value used as a boundary condition is a function of the height at which the boundary is applied, with respect to the heights at

which the retrieved temperatures are to be used. For boundary conditions in error by up to 2 ºC (one standard deviation for the difference between GEM temperatures and radiosonde) overall profile error is below 0.6 ºC. Since the effect of boundary condition error decreases as the refractivity increases, boundary conditions in error by 2 ºC applied at 35 km will result in less than 0.6 ºC error at and below a height of 26 km.

The required accuracy for temperature profiles used to retrieve humidity is a function of the level of humidity present for the event being retrieved. For the average humidity present in the data used in this work, temperatures would only need to be accurate to 6.6 ºC to retrieve water vapour with 50% relative accuracy. This is well within the accuracy available from NWP. Drier events have correspondingly higher requirements to reach the same level of error, with the driest events not being realistically retrievable at all. This suggests problems retrieving water vapour for very dry conditions, such as are common in the Canadian arctic. For temperatures accurate to 2 ºC, water vapour pressure would be retrievable with a relative accuracy of 50% or less for 72% of Canadian events. To increase the proportion of events for which water vapour can be accurately retrieved, refractivity error arising from the retrieval would need to be reduced, or more accurate temperature profiles used.

Tests using the CMC's GEM model as a data source for both temperature boundary conditions and temperature profiles suggest that it is a suitable data source for occultation retrievals. Dry temperature profiles produced using GEM boundary conditions are

accurate to 1.59 ºC RMS when compared to CHAMP profiles bounded by ECMWF. This is a 6% improvement over profiles computed using boundary conditions from radiosondes. In a small number of events, the GEM temperatures at 10 mb used for the boundary condition were obvious outliers in comparison to radiosonde measurements at that height, and to the general lapse rate of the GEM temperatures lower in the profile. Retrievals using these outlying boundary conditions experience significant error.

Spatial location of the boundary condition has no significant effect on the profile accuracy, however some degradation is observed using forecasted GEM data, as opposed to analysis time data. Overall, a 16% increase in RMS error is observed using 12 hour forecasted data rather than analysis time data, increasing from 1.37 ºC RMS to 1.53 ºC RMS. This has implications for researchers using forecasted GEM products to perform RO retrievals in near real time as compared to post mission retrievals.

Humidity results obtained using GEM temperature profiles suggest that the GEM product is suitable for this application, but are limited by the refractivity error arising from the processing in this work. In some cases under sampling of the tropopause in the GEM product may result in errors in the humidity retrieval around the tropopause. At lower altitudes where the vertical gradient is smoother, the sampling interval of the GEM product is sufficient. Retrievals using real GEM data also highlight the issues surrounding dry events which were identified when defining the required accuracy for the NWP product. Dry events show high relative errors, especially at higher altitudes, which

translates into practical problems in expressing the humidity in terms of relative humidity or dew point depression rather than partial water vapour pressure.

6.2. Recommendations and future work

Enhanced and robust error detection will be an important component for any operational application of RO work similar to the work done here. Gross errors in retrievals occur at numerous stages in the processing, in some cases caused by L2 data quality, some caused by extreme outlying boundary conditions, and some for which the causes are not known. In this work, detection and removal or repair of grossly erroneous events has been done manually, but that approach is not practical for larger data volumes. Error detection routines are recommended to identify gross errors at each stage of the processing, and repair them whenever possible.

Errors caused by cycle slips on L2 occur in 16% of the events used in this work. It is possible that L2 data quality will be of particular concern for Canadian retrievals as compared to tropical and mid latitude occultations, because of scintillation effects present in the ionosphere in the auroral zone. An examination of L2 data quality as a function of latitude would be an interesting direction for further research.

Cycle slips on L2 can be directly repaired or rejected in the Doppler data, or the effect can be avoided by adjusting the height below which L2 data is no longer used to construct the IF bending angle. Raising the L2 rejection height has a corresponding

effect on the accuracy of the retrievals below that height, and so care should be taken to raise it no further than necessary. A full examination of the effects of L2 rejection height on profile accuracy would be a valuable extension to this work, if threshold adjustment was to be used. The recently implement L2C signal, included as part of the modernization of GPS, could also be expected to reduce the frequency of mid altitude cycle slips by improving signal strength and tracking on L2. Additional options for improved signal tracking will also be available with the new L5 signal, and the upcoming Galileo system.

In cases where gross errors result from biased boundary conditions, the 10 mb GEM temperature being used is clearly outlying from both the radiosonde and the trend of the remainder of the GEM profile. As radiosonde data is not likely to be available for near-real time processing, the profile trend is a better choice to indicate when the 10 mb temperature is in error. Identification of these outlying temperatures would be a necessary component of any operational processing relying on 10 mb GEM temperatures for boundary conditions. The next temperature value below 10 mb could be used as a boundary condition instead in these cases.

Use of the current public GEM product for temperature boundary conditions is greatly limited by the vertical extent of the product, extending to only 50 mb (~21 km). This places a corresponding limit on the range of dry temperatures which can be derived. It is

recommended that researchers using the current product seek to obtain temperatures at higher pressure levels, which may be available.

Humidity retrievals could be improved by application of the canonical transform technique and the use of open-loop tracking data. This would greatly increase the refractivity accuracy which could be obtained from the occultation, which would translate into a corresponding increase in the humidity accuracy. Humidity retrievals in the direct vicinity of the tropopause are likely to be affected to some degree by under sampling in the GEM temperature profile. This is unavoidable, as RO invariably has higher vertical resolution than NWP. The effect of undersampling will not be as severe with the current GEM product as it is in this work however, as the current product has data at more pressure levels around the tropopause. The data used in this work has 4 levels between 150 and 300 mb (~13 – 9 km), while the current product has 8 levels in this range.

In conclusion, the GEM model appears to be a suitable NWP data source for operational retrievals from radio occultation.

References

Aparicio, J.M., G. Deblonde (2004) "*Assessment of Impact of the Assimilation of GPS Radio Occultation Observations*", Proc. ION GNSS 17th International Technical Meeting of the Satellite Division, Long Beach, USA, 21-24 September

Barenbrug, A.W.T. (1974) "*Psychrometry and Psychrometric Charts, 3rd Edition*", Cape and Transvaal Printers Ltd., Cape Town, South Africa

Bevis, M., S. Businger, T.A. Herring, C. Rocken, R.A. Anthes, R.H. Ware (1992) "*GPS Meteorology: Remote Sensing of Atmospheric Water Vapor Using the Global Positioning System*", Journal of Geophysical Research, v 97, issue D14, pp 15787-15801

Canadian Meteorological Centre website, http://www.msc-smc.ec.gc.ca/cmc/index_e.html, accessed Semptember 2007

Côté, J., S. Gravel, A. Méthot, A. Patoine, M. Roch, A. Staniforth (1998) "*The Operational CMC-MRB Global Environmental Multiscale (GEM) Model. Part I: Design Considerations and Formulation*" Monthly Weather Review, v 126, pp 1373-1395

Fjeldbo, G.F., A.J. Kliore, V.R. Eshleman (1971) "*The Neutral Atmosphere of Venus as Studied with the Mariner V Radio Occultation Experiments*", The Astronomical Journal, v 76, no 2, pp 123-140

Gerding, M., A. Weisheimer (2003)."*Validation of water vapour profiles from GPS radio occultations in the Arctic*" First Champ Mission Results for Gravity, Magentic and

Atmospheric Studies: Proceedings of the First Champ Science Meeting, Springer-Verlag, New York, USA

Goff, J. A. & S. Gratch (1946) "*Low-pressure properties of water from -160 to 212 °F*", Transactions of the American Society of Heating and Ventilating Engineers, v 52, pp 95-121

Gorbunov, M.E., A.S. Gurvich (1998) "*Algorithms of inversion of Microlab-1 satellite data including effects of multipath propagation*", Intl. Journal of Remote Sensing, v 19, pp 2283-2300

Gorbunov, M.E. (2001) "*Radioholographic methods for processing radio occultation data in multipath regions*" Tech. Report 01-02, Danish Meteorological Institute, Copenhagen, Denmark

Gorbunov, M.E. (2002a) "*Canonical transform method for processing GPS radio occultation data in the lower troposphere*" Radio Science, v 37, p 1076

Gorbunov, M.E. (2002b) "*Radio-holographic analysis of Microlab-1 radio occultation data in the lower troposphere*", Journal of Geophysical Research, v 107, p 4156

Hajj, G.A., E.R. Kursinski, L.J. Romans, W.I. Bertiger, S.S. Leroy (2002) "*A technical description of atmospheric sounding by GPS occultation*", Journal of Atmospheric and Solar-Terrestrial Physics, v 64, pp 451-469

Hajj, G.A., C.O. Ao, B.A. Iijima, D. Kuang, E.R. Kursinski, A.J. Mannucci, T.K. Meehan, L.J. Romans, M. de la Torre Juarez, T.P. Yunck (2004) "*CHAMP and SAC-C Atmospheric Occultation Results and Intercomparisons*", Journal of Geophysical Research, v 109, D06109

Hedin, A. E. (1991) "*Extension of the MSIS Thermosphere Model into the Middle and Lower Atmosphere*", Journal of Geophysical Research, v 96, pp 1159-1172

Hocke, K. (1997) "*Inversion of GPS Meteorology Data*", Annales Geophysicae, v 15, pp 443-450

IGS website, http://igscb.jpl.nasa.gov, accessed July 2007

Kaplan, E.D., C.J. Hegarty, eds. (2006) "*Understanding GPS Principles and Applications – 2nd edition*", Artech House, Norwood, USA

König, R., S. Zhu, Ch. Reigber, K.-H. Neumayer, H. Meixner, R. Galas, G. Baustert, P. Schwintzer (2002) "*CHAMP Rapid Orbit Determination for GPS Atmospheric Limb Sounding*", Advances in Space Research, v. 30, pp 289-293

Konig, R., G. Michalak, K.H. Neumayer, R. Schmidt, S.Y. Zhu, H, Meixner, C. Reigber (2005) *"Recent Developments in CHAMP Orbit Determination at GFZ*", in *Earth Observation with CHAMP: Results from Three Years in Orbit*, pp 65-70, Springer Berlin Heidelberg

Kursinski, E.R, G.A. Hajj, J.T Schofield, R.P. Linfield, K.R. Hardy (1997) "*Observing Earth's atmosphere with radio occultation measurements using the Global Positioning System*", Journal of Geophysical Research, v 102, pp 23,429-23,465

Kursinksi, E.R. (2004) "*GPS Occultation Introduction and Overview*", presented at the NCAR Summer Colloqium on Atmospheric Remote Sensing using GPS, Boulder, Colorado, 20 June – 2 July

Lachapelle, G. (2004) "*Advanced GPS Theory and Applications: Lecture Notes*", Dept. of Geomatics Engineering, University of Calgary, Canada

Marquardt, C. K. Labitzke, Ch. Reigber, T. Schmidt and J. Wickert (2000) *"An Assessment of the Quality of GPS/MET Radio Limb Soundings During February 1997"* Phys. Chem. Earth, vol 26, no 3, pp 125-130

Marquardt, C., K. Schöllhammer, G. Beyerle, T. Schmidt, J. Wickert, C. Reigber (2002) "*Validation and Data Quality of CHAMP Radio Occultation Data*", Proc. First CHAMP Science User Meeting, Potsdam, Germany, 22-25 January

Niell, A.E., A.J. Coster, F.S. Solheim, V.B. Mendes, P.C. Toor, R.B. Langley, C.A. Upham (2001) "*Comparison of Measurements of Atmospheric Wet Delay by Radiosonde, Water Vapor Radiometer, GPS, and VLBI*", Journal of Atmospheric and Oceanic Technology, v. 18, pp 830-850

Olynik, M.C. (2002) "*Temporal Characteristics of GPS Error Sources and Their Impact on Relative Positioning*" (M.Sc. Thesis), Department of Geomatics Engineering, University of Calgary, Canada

Parkinson, B.W., J.J. Spilker, eds. (1996) "*Global Positioning Sytem: Theory and Applications*", American Institue of Aeronautics and Astronautics, Washington, D.C., USA

Paroscientific website, http://www.paroscientific.com, accessed August, 2007

Rocken, C., R. Anthes, M. Exner, D. Hunt, S. Sokolovskiy, R. Ware, M. Gorbunov, W. Schreiner, D. Feng, B. Herman, Y-H. Kuo, X. Zou (1997) "*Analysis and validation of GPS/MET data in the neutral atmosphere*" Journal of Geophysical Research, v. 102, no. D25, pp 29,849-29,866

Rocken, C., Y.-H. Kuo, W. Schreiner, D. Hunt, S. Sokolovskiy, C. McCormick (2000) "*COSMIC System Description*", Special Issue of Terrestrial, Atmospheric, and Oceanic Science, v 11, pp 21-52

Smith, E.K., S. Weintraub (1953) "*The Constants in the Equation for Atmospheric Refractive Index at Radio Frequencies*", Proceedings of the IRE, v 41, pp 1035-1037

Sokolovskiy, S.V. (2001) *"Tracking tropospheric radio occultation signals from low Earth orbit*", Radio Science, v. 36, pp 483-498

Sokolovskiy S, Y.-H. Kuo, C. Rocken, W.S. Schreiner, D. Hunt, R.A. Anthes (2006) *"Monitoring the atmospheric boundary layer by GPS radio occultation signals recorded in the open-loop mode"* Geophysical Research Letters, v. 33, L12813

Steiner, A.K., G. Kirchengast, H.P. Ladreiter (1999) "*Inversion, error analysis, and validation of GPS/MET occultation data*", Annales Geophysicae, v 17, pp 122-138

Svehla, D., & M. Rothacher (2005) "*Kinematic Positioning of LEO and GPS satellites and IGS stations on the ground*", Advances in Space Research, v36, pp 376-381

Syndergaard, S. (1998) "*Modeling the impact of the Earth's oblateness on the retrieval of temperature and pressure profiles from limb sounding*", Journal of Atmospheric and Solar-Terrestrial Physics, v 60, pp 171-180

Vorob'ev, V.V., T.G. Krasil'nikova (1993) "*Estimation of the Accuracy of the Atmospheric Refractive Index Recovery From Doppler Shift Measurements at Frequencies Used in the NAVSTAR System*", Izvestiya Atmospheric and Oceanic Physics, v 29, pp 602-609

Ware, R., M. Exner, D. Feng, M. Gorbunov, K. Hardy, B. Herman, Y. Kuo, T. Meehan, W. Melbourne, C. Rocken, W. Schreiner, S. Sokolovskiy, F. Solheim, X. Zou, R. Anthes, S. Businger, K. Trenberth (1996) "*GPS sounding of the atmosphere from low earth orbit: preliminary results*", Bulletin of the American Meteorological Society, v 77, pp 19-40

Wickert, J., C. Reigber, G. Beyerle, R. König, C, Marquardt, T. Schmidt, L. Grunwaldt, R. Galas, T.K. Meehan, W.G. Melbourne, K. Hocke (2001a) "*Atmospheric Sounding by GPS radio occultation: First results from CHAMP*", Geophysical Research Letters, v 28, pp 3263-3266

Wickert, J., R. Galas, G. Beyerle, R. König, C. Reigber (2001b) "*GPS Ground Station Data for CHAMP Radio Occultation Measurements*", Phys. Chem. Earth, v 26, pp 503-511

Wickert, J., T. Schmidt, C. Marquardt, Ch. Reigber, K.-H. Neumayer, G. Beyerle, R. Galas, L. Grunwaldt (2001c) "*GPS radio occultation with CHAMP: First results and status of the experiment*" Proceedings of the IAG Scientific Assembly, Budapest, Hungary, 2 – 8 September

Wickert, J., G. Beyerle, G.A. Hajj, V. Schweiger, C. Reigber (2002) "*GPS radio occultation with CHAMP: Atmospheric profiling utilizing the space-based single difference technique*", Geophysical Research Letters, v 29, p 1187

Wickert, J., R. König, T Schmidt, C. Reigber, N. Jakowski, G. Beyerle, R. Galas, L. Grunwaldt, T.K. Meehan, T.P. Yunck (2003) "*The radio occultation experiment aboard CHAMP (Part I): Operational data processing, technical aspects, atmospheric excess phase calibration and ionospheric profiling*", Proc. International Workshop on GPS Meteorology, Tsukuba, Japan, 13-17 January

Wu, S.C., T.P. Yunck, C.L. Thornton (1991) "*Reduced dynamic technique for precise orbit determination of low earth satellites*" Journal of Guidance, Control, and Dynamics, v 14, pp 24-30